

University of Naples Federico II

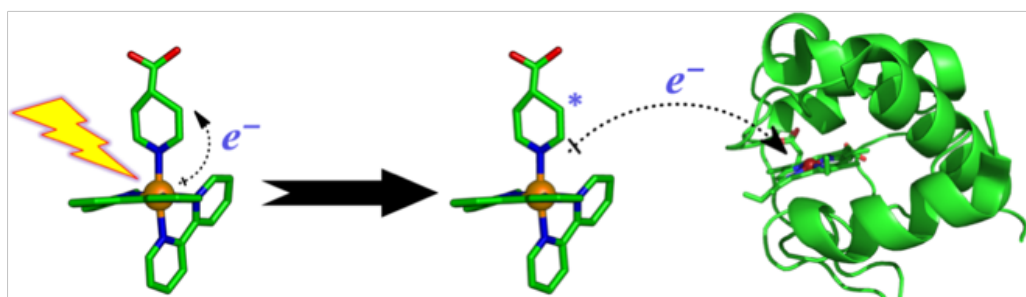
Polytechnic and Basic Science School

Department of Chemical Sciences



Ph.D. in Chemical Sciences

Developing Artificial Multi-Metal Peptide-Based Photocatalysts



Diaa Aref

Advisor:

prof. Angela Lombardi
prof. Michele Pavone

Examiner:

prof. Antonello Merlino

XXXII Cycle 2017 – 2020

Coordinator: *prof. Angela Lombardi*

Dissertation

Developing Artificial Multi-Metal Peptide-Based Photocatalysts

by

Diaa Aref

Advisor:

prof. Angela Lombardi
prof. Michele Pavone

Examiner:

prof. Antonello Merlino

XXXII Cycle 2017 – 2020

Coordinator: prof. Angela Lombardi

Dedicated to

My home...

Palestine

Acknowledgment

Foremost, I want to offer this endeavor to our **God Almighty** for the strength, patency, mental peace and good health that is bestowed upon me in order to finish this work. **Asking him satisfaction and acceptance** .

I wish to express my sincere gratitude to my family, for my Mom and Dad, the most important persons in my life, for all the warm-heartedness, sympathy, love and real support that is granted by them in the entire of my life. To my brothers and sisters for their encouragement and support. **Thank you all** .

To my beloved and supportive wife, Manar, who is always by my side, when time is needed. For her patency during my dissertation works, when I spend a long time and energy perusing goals that took me away from her, and never forget her encouragement and support. **"Behind every great man stands a woman"** .

I would like to express my deepest gratitude and profound respect to my advisers; prof. Angela Lombardi, for her guidance and supervision, for providing necessary information regarding this research, and the all support that is given to me to completing this endeavor. Also, my sincere gratitude is given to Prof. Michele Pavone for his patience, motivation and immense knowledge in the computational measurements, How I wished if I had the time to learn more from him. **The author thankful for having such good advisors like you** .

Immeasurable appreciation and sincere gratitude are given to Dr. Marco Chino for his support, guidance, valuable comments and suggestions throughout this research, and last by giving endless help to finish this thesis. **The author is thankful for you and your support** .

Infinite gratitude and appreciation to prof. Vincenzo Pavone for his encouragement, helpful guidance, valuable comments and being available during my research. **Thank you .**

Sincere gratitude is also given to Dr. Ornella Maglio for the valuable knowledge in NMR analysis, and for her support and helps that is given to me that I will never forget. Also, sincere gratitude is given to prof. Flavia Nastri for her support, help and precious knowledge. And never forget to send my sincere gratitude to Dr. Daniele D'Alonzo for the support and precious knowledge in NMR. **Many thanks for all of you .**

I would like to express my warmest individual sincere and thanks to all my colloquies in the artificial metalloenzyme group (AME) group, for rendered help that was given when needed, and for all memorable moments and events that we have spent together, which I will never forget, **Thank you all .**

Besides, sincerely thanks for prof. Kara Bren and her kindly group, with special thanks to Dr. Jennifer Le and Dr. Emily Edwards for the collaboration and photocatalytic hydrogen experiments. **Thank you all .**

Last and not least, I would like to express my deep sense of gratitude for both Universities; An-Najah National University and University of Napoli Federico (II), and also for the Chemistry Department at An-Najah University represented by Dr. Nedal Zatar and Chemical Sciences at Napoli Federico (II) University represented by Prof. Angela Lombardi for facilitating the collaboration and for giving me this opportunity for doing my Ph.D. .

With my all warmest Thankful and deepest sincere gratitude.

The Author

DIAA AREF

13/03/2020

Table of content

No.	Title	Page
Abstract		ix
Chapter (1)		
Synthesis and characterization of a new ruthenium(II) photosensitizer		
1.1.	Introduction	3
1.1.1.	Photosensitizer classes and their action mechanism	5
1.1.1.1.	Photo-induced charge transfer processes	7
1.1.1.2.	Photo-induced excitation of metal complexes	9
1.1.1.3.	Excited state theoretical concepts	12
1.1.1.4.	Photo-induced electron and energy transfer processes	16
1.1.2.	Triplet-state [Ru ^{II} -polypyridine] photosensitizers	20
1.1.3.	Structural and functional aspects of [Ru ^{II} tris-bidentate] and [Ru ^{II} bis-tridentate] complexes	23
1.1.4.	Photosensitization of native proteins	27
1.2.	Aims (chapter 1)	32
1.3.	Result and Discussion	34
1.3.1.	Synthesis and characterization of a new ruthenium(II) polypyridine complex	34
1.3.1.1.	Reaction monitoring and product formation	36
1.3.1.2.	Product purification and characterization	41
1.3.2.	NMR-based structural characterization	44
1.3.2.1.	NMR characterization of the complex 2	44
1.3.2.2.	NMR characterization of the complex 3	45
1.3.3.	Photophysical characterization of the complex 3	48

No.	Title	Page
1.3.4.	Theoretical calculations	54
1.3.4.1.	Structural optimization	54
1.3.4.2.	Binding energy calculation	55
1.3.4.3.	Electronic transition calculation	57
1.3.5.	Photochemical characterization of the complex 3	60
1.4.	Concluding Remarks	65
1.5.	Materials and Methods	66
1.5.1.	Materials, reagents, and solvents	66
1.5.2.	Instrumentations and techniques	66
1.5.3.	General procedure for preparation of the complex 3	68
	References	69

Chapter (2)

Building a photosensitizing framework for a class of artificial porphyrin-based hydrogenases

2.1.	Introduction	87
2.1.1.	Hydrogenases: natural enzymes for hydrogen reduction	90
2.1.1.1.	[FeFe] Hydrogenases	92
2.1.1.2.	[NiFe] Hydrogenases	95
2.1.1.3.	[Fe] Hydrogenases	98
2.1.2.	Artificial peptides and model systems for HERs:	100
2.1.3.	Insight on mimochromes as artificial enzymes	108
2.2.	Aims (chapter 2)	114
2.3.	Result and Discussion	115
2.3.1.	Synthesis and characterization of the bi-metallic nuclear assemblies of 3 and Co ^{III} MC6*a	115

No.	Title	Page
2.3.1.1.	Synthesis and characterization the 1 st prototype conjugate (3-[DBCO-PEG ₄]Co ^{III} MC6*a)	116
2.3.1.2.	Photo-induced hydrogen evolution by Co ^{III} MC6*a using 3 and [Ru ^{II} (bpy) ₃] as photocatalysts	127
2.3.1.3.	Synthesis and characterization the 2 nd prototype conjugate (3-Co ^{III} MC6*a)	132
2.4.	Concluding Remarks	138
2.5.	Materials and Methods	140
2.5.1.	Materials, reagents, and solvents	140
2.5.2.	Instrumentations and techniques	140
2.5.3.	General Procedure	142
2.5.3.1.	Synthesis the 1 st prototype conjugate (3-[DBCO-PEG ₄]Co ^{III} MC6*a)	142
2.5.3.2.	Synthesis the 2 nd prototype conjugate (3-Co ^{III} MC6*a)	144
	References	145
	Supporting information	159

Abstract

The development of photosynthetic systems is a growing field in chemistry with significant environmental applications. Ruthenium(II)-based polypyridine complexes are thoroughly studied for their capability to perform light-driven catalysis and to photo-induce charge-transfer to diverse organic, inorganic, and biological molecules. However, the development of a powerful and durable photosensitizer, which can be easily conjugated to different biocatalysts, has not been achieved yet.

In the field of artificial metalloenzymes, the design of a suitable photosensitizing unit that can be tethered to such compounds is of particular interest, considering that only few multi-cofactor artificial metalloproteins have been reported so far. Among them, $[\text{Ru}^{\text{II}}(\text{bpy})_3]$ and $[\text{Ru}^{\text{II}}(\text{tpy})_2]$ have been generally adopted. $[\text{Ru}^{\text{II}}(\text{bpy})_3]$ possesses well-known photophysical and photochemical properties, such as high chemical stability, high molar absorptivity ($\sim 14,600 \text{ M}^{-1}\text{cm}^{-1}$), and fluorescence quantum yield. Moreover, an excited-state lifetime in the order of microseconds ($\sim 1,100 \text{ ns}$) is crucial for its photochemical application. However, because of its stereogenic metal center, the functionalization of one or more of the coordinated bpy-ligands produces at least two stereoisomers (Λ and Δ) with distinct photophysical properties, increasing the synthetic complexity. In contrast, $[\text{Ru}^{\text{II}}(\text{bpy})_3]$ has an isomeric defined structure. Nevertheless, poor photophysical properties, such as lower molar absorptivity ($< 10,000 \text{ M}^{-1}\text{cm}^{-1}$) and picosecond excited state-lifetime, hamper its applicability. Several reports have been published that describe tris-heteroleptic complexes as a feasible alternative in order to overcome such limitations.

In chapter one, we report our contribution in the field of photosensitization. The synthesis and characterization of a new tris-heteroleptic ruthenium(II) complex, $[\text{Ru}^{\text{II}}(\text{bpy})(\text{tpy})(\text{pyCOOH})]$ (bpy = 2,2'-bipyridine, tpy = 2,2':2'',6'-terpyridine and pyCOOH = 4-carboxylpyridine), will be presented. Such complex has an isomerically-defined structure; it holds a carboxyl moiety that provides a versatile coupling moiety for bioconjugation, and that enhances its photophysical properties thanks to the electron withdrawing effect. The photophysical performance of the ruthenium(II) complex has been characterized by steady-state spectroscopic experiments, and supported by DFT and TD-DFT calculations for further understanding of the observed properties at a molecular scale. The synthesized ruthenium(II) complex has shown an enhanced light absorptivity of approximately $12,000 \text{ M}^{-1}\text{cm}^{-1}$ (at $\lambda_{\text{max}} = 460 \text{ nm}$) and $13,000 \text{ M}^{-1}\text{cm}^{-1}$ (at $\lambda_{\text{max}} = 427 \text{ nm}$) in acetonitrile, and a wider range of visible light absorption in comparison to $[\text{Ru}^{\text{II}}(\text{bpy})_3]$ ($14,600 \text{ M}^{-1}\text{cm}^{-1}$; $\lambda_{\text{max}} = 460 \text{ nm}$). As expected for this class of terpyridine-based ruthenium(II) complexes, $[\text{Ru}^{\text{II}}(\text{bpy})(\text{tpy})(\text{pyCOOH})]$ has only limited fluorescence quantum yield, approximately tenfold less than $[\text{Ru}^{\text{II}}(\text{bpy})_3]$ ($\Phi([\text{Ru}^{\text{II}}(\text{bpy})(\text{tpy})(\text{pyCOOH})])=0.009$; $\Phi([\text{Ru}^{\text{II}}(\text{bpy})_3])=0.095$). The TD-DFT shows that the electronic density of the LUMO, involved in the charge transfer transition, mainly occupies the carboxyl moiety. Such key feature could be extremely positive if we consider that such moiety is involved into the conjugation between the ruthenium(II) complex and other molecular assemblies.

The photochemical performance has been studied using a multicomponent system, composed of the ruthenium(II) complex, cytochrome c and aniline as the photosensitizer, electron acceptor and sacrificial electron donor, respectively. The photo-induced electron transfer process was found to be pseudo first-order against ruthenium(II) complex concentration, being 76% as active as $[\text{Ru}^{\text{II}}(\text{bpy})_3]$. Such lower activity may be accounted to the higher activation energy barrier (ca. $3.7 \text{ kJ}\cdot\text{mol}^{-1}$) between the two complexes.

In chapter two, the tethering between the ruthenium(II) complex and artificial peptide has been tested by preparing two prototype systems based on cobalt(III) *Mimochrome VI*a* ($\text{Co}^{\text{III}}\text{MC6*a}$), which is a rationally designed heme-peptide conjugate. The latter has been reported for its remarkable electrochemical activity, longevity, and stability in electrochemical hydrogen evolution in water under mild conditions. Therefore, $\text{Co}^{\text{III}}\text{MC6*a}$ has been used as a model system to test the here-presented complex conjugation. Two conjugation protocols have been characterized using both spectroscopic and chromatographic techniques. The synthetic results show that the ruthenium(II) complex can be easily tethered to the lysine-residue of $\text{Co}^{\text{III}}\text{MC6*a}$ either through click-chemistry crosslinking (using DBCO-PEG₄-NHS as the spacer) or through direct conjugation (using a one-pot protocol for NHS coupling). Preliminary results of photoinduced hydrogen evolution have shown that it occurred only when $[\text{Ru}^{\text{II}}(\text{bpy})_3]$ was used as freely diffusing photosensitizer. Nonetheless, spectroscopic evidence has excluded any inactivation of $\text{Co}^{\text{III}}\text{MC6*a}$ by the $[\text{Ru}^{\text{II}}(\text{bpy})(\text{tpy})(\text{pyCOOH})]$ complex, thus confirming the general covalent approach of photosensitization.

Chapter 1

Synthesis and characterization of a new ruthenium(II) photosensitizer

1.1. Introduction

Sun is a freely available, abundant, and sustainable energy source. The earth receives solar energy, as heat and light, at the rate of approximately $1.2 \cdot 10^{18} \text{ J.s}^{-1}$, which exceeded the annual worldwide energy consumption rate of approximately $1.5 \cdot 10^{14} \text{ J.s}^{-1}$ ³. Today, an effective method for capturing, converting, and storing solar energy is still under development.

The available methods for harvesting solar-energy are fundamentally three:

(i) Solar-cells (known as photovoltaics “PV”), which convert sunlight directly into electricity. Typically, photovoltaics convert near “10 - 20%” of the energy received to electricity^{4,5}. Recently, the most efficient solar cell has been reported by F. Dimroth’s group, being a gallium-based multi-junction concentrator PV with an efficiency of 46%⁶.

(ii) Solar-thermal electricity, in which the solar heat energy is transferred to a working fluid of a Stirling engine. The mechanical power is then converted into electricity by an electric generator or an alternator⁷. The complexity of this system constraints its application to the electric supply in vast areas and facilities⁸.

(iii) Other chemistry-based technologies, in which solar energy is used either as heat (thermochemical reactions) or light (photochemical reactions) to drive chemical transformations, such as fuel production^{9,10}.

Solar energy is already utilized in different applications, e.g., organic synthesis¹¹, photodynamic therapy¹², dye-sensitized solar cell (DSSC)¹³⁻¹⁵, fuel cell technologies¹⁶, and biofuel production¹⁷. Sunlight-dependent fuel production is generally referred to as artificial photosynthesis¹⁸.

In photosynthesis, the sunlight is converted and stored as chemical bonds belonging to the so-called “high-energy substances” (or energy carriers)^{9,10}.

Hydrogen, oxygen, and hydrocarbons are the most common examples of such energy carriers ^{3,18–21}. Photosynthesis is considered a growing field in chemistry; despite its undoubted advantages in sustainable fuel production, the development of efficient systems for sunlight harvesting and conversion to the carriers is still an open challenge ^{19,20}.

Light harvesting can be accomplished by photon absorption and subsequent charge-separation processes. The photosensitizer is the molecular system that works as antennas; it initiates a chemical reaction by capturing a photon at an appropriate wavelength ^{22,23}. The photosensitization is the process by which the excited photosensitizer performs electron or energy transfer to another molecule, the so-called acceptor, ultimately forming highly reactive species useful for several applications, such as photosynthesis ^{18,24}.

Inspired by the extensive knowledge earned over the past centuries in the fields of photophysics and photochemistry, many authors are involved in the development of efficient, durable, and synthetically accessible photosensitizers. Indeed, photosensitizer features must be opportunely tuned to match the requirements needed for a specific application, such as catalysis.

Next **section (1.1.1)** will briefly describe the basic physical and chemical concepts of photosensitization. Later on, a particular focus will be dedicated to ruthenium(II) complexes as photosensitizers, **section (1.1.2; p. 21)**.

1.1.1. Photosensitizer classes and their action mechanism

The increasing interest in sunlight energy conversion and in particular in photochemical reactions and photosynthesis boosted the research towards the discovery of novel photosensitizers. Such compounds must be at the same time: **(i)** efficient in harvesting visible-light and **(ii)** able to initiate chemical reactions. Several inorganic and few organic molecules have been investigated in the development of new photosensitizers.

Photosensitizers can be classified as organic or inorganic (organometallic) photosensitizers.

Inorganic (organometallic) photosensitizers are characterized by harvesting wide range of the visible light due to their metal to ligand charge transfer, populating the long-lived triplet excited-state and forming unstable species upon excitation. Consequently, providing sufficient time for producing energy or electrons transfer useful for chemical reactions²⁴⁻²⁸.

Inorganic dyes are widely used in photo-redox and photochemical catalysis²⁴⁻²⁸. However, the high price, toxicity profile, and problematic recyclability might limit their more general use especially on larger scales²⁹.

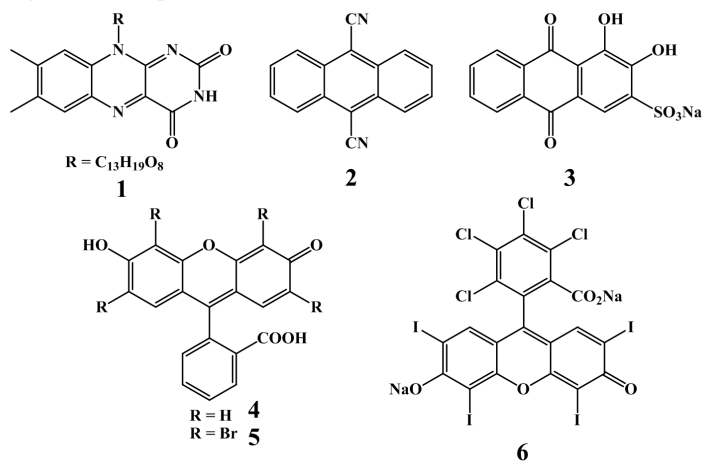
On the other hand, the organic (metal-free) photosensitizers show higher absorption intensity of light ($\sim 10^5$) and fluorescence quantum efficiency. However, organic molecules generally have lower chemical stability and lower excited-state lifetime, thus limiting their applications in photosensitizing solar cells (DSSC) and in bio-imaging applications³⁰⁻³².

In **Figure (1.1)**, a few examples of such molecular systems are summarized:

(i) Organic-class of photosensitizers: flavin (**1**), 9,10-dicyanoanthracene (**2**), alizarin red S (**3**), fluorescein (**4**), eosin Y (**5**) and rose bengal (**6**)

(ii) Inorganic (or Organometallic)-class of photosensitizers: $\text{Ru}(\text{bpy})_3$ (7), $\text{Ru}(\text{tpy})_2$ (8), $\text{Ir}(\text{bpy})\text{ppy})_2$ (9), $\text{Rh}\{4,4'(\text{tBu})_2\text{bpy}\}_3$ (10) and $\text{Re}(\text{bpy})(\text{CO})_3\text{SCN}$ (11).

Organic-based photosensitizers:



Inorganic (organometallic) -based photosensitizers:

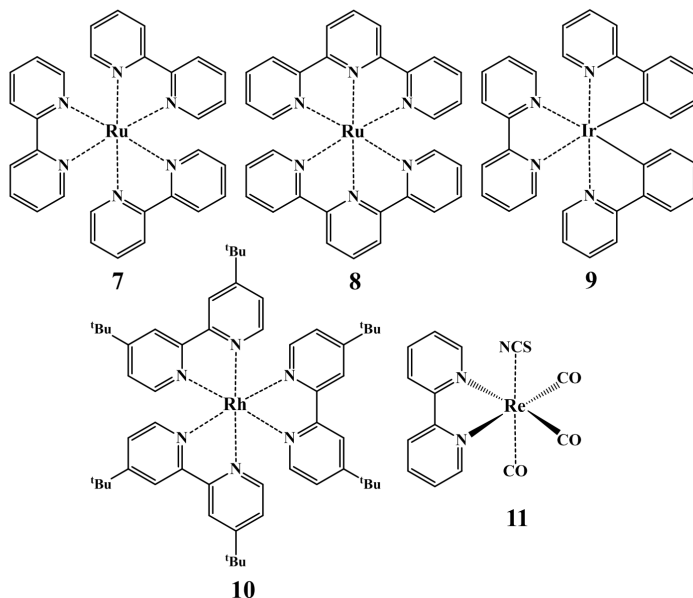


Figure (1.1). Chemical structures for some organic and inorganic (or organometallic) photosensitizers.

1.1.1.1. Photo-induced charge transfer processes

After the absorption of a photon, the promotion of an electron to a higher energy level (electronic excited state) occurs. Consequently, highly energetic unstable species are formed. The excess energy undergoes some types of allowed deactivation pathways, either by radiative or non-radiative processes³³.

The Jablonski diagram, **Figure (1.2)**, is a diagram that illustrates the electronic states of a molecule and the transitions between them. The states are arranged vertically by energy and grouped horizontally. The photo-electron dynamics is ruled by spin factors, spatial symmetry, and the character of the electronic states involved in the electronic transitions^{24,34}.

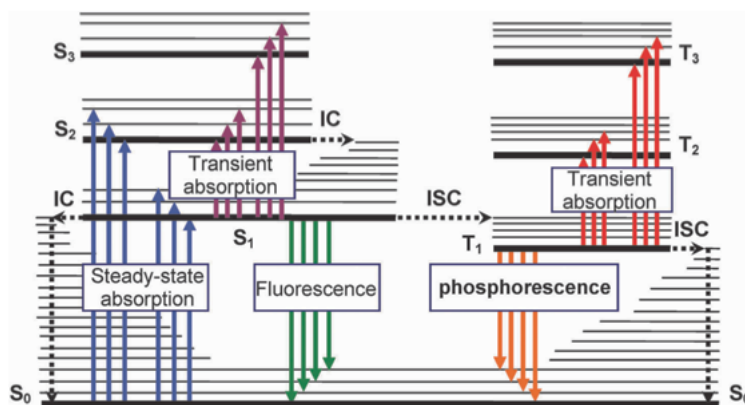


Figure (1.2). The schematic image represents the Jablonski diagram and the photo-electron dynamic pathways. [Reproduced from 'Ref. 34' with permission of the publisher]

Based on the Jablonski diagram, the photophysical processes occurring in photoactive molecules are the following:

- (i) The absorption of the photon allows the electron to populate the vibrational levels of the higher singlet electronic states ($S_1, S_2 \dots$). This absorption process occurs within $\sim 10^{-15}$ sec and can be probed by steady-state absorption spectroscopy, **Figure (1.2; blue arrows)**.
- (ii) The dissipation of the energy occurs through a non-radiative vibrational relaxation to the first lower vibronic excited state (S_1) in a process so-called *internal crossing* (IC), the energy being released to the surrounding (i.e. the solvent). This process occurs within $10^{-14} - 10^{-10}$ sec, and required sophisticated probing techniques, such as transient fluorescence and absorption spectroscopies, **Figure (1.2; dashed black horizontal arrows)**.
- (iii) The IC can be followed by radiative deactivation, the so-called *fluorescence*, in which the excess of the excited state energy (S_1) can be released as radiated emission with higher wavelength (lower in energy). This process occurs within $10^{-9} - 10^{-6}$ sec, and can be probed by steady-state fluorescence spectroscopy, **Figure (1.2; green arrows)**.
- (iv) The deactivation of the excited state (S_1) occurs through *intersystem crossing* (ISC) followed by another form of radiative decay, the so-called *phosphorescence*. The ISC occurs within $10^{-10} - 10^{-8}$ sec, by populating the excited triplet vibronic states through spin inversion. The energy minimum is then reached by vibrational relaxation to T_1 . This mechanism ends up by another type of radiative deactivation to the ground state (S_0), the *phosphorescence*. The *phosphorescence* is generally characterized by prolonged lifetime of the excited triplet state, which decays within $>10^{-3}$ sec, and can be probed by using steady-state fluorescence spectroscopy, **Figure (1.2; red arrows)**.

- (v) Deactivation from S_1 or T_1 to the ground state (S_0) may occur in a non-radiative process, called *quenching*, within $10^{-7} - 10^{-5}$ sec. In this deactivation process, the energy is transferred to other molecules and/or photoactive species and/or the surrounding (i.e. the solvent). The dynamic of the *quenching* mechanism of the excited state is ruled by diffusional and collision processes, **Figure (1.2; dashed black vertical arrows)**.
- (vi) By performing a photochemical reaction, in which the excited state is deactivated through molecular reorganization, dissociation, through energy or electron transfer processes leading to chemical reactions.

1.1.1.2 Photo-induced excitation of metal complexes

The charge transfer (CT) is a fundamental process in photophysics and photochemistry. In the CT, an electron transfer is induced by radiative or non-radiative processes, between weakly coupled Donor (D) and Acceptor (A) electronic states³⁵.

In metal complexes, the electronic CT (i.e. an electronic transition) occurs between the central metal atom and the surrounding ligands. A CT complex may be defined as the inner-sphere ligands and the metal nuclei. Two major classes of CT may be identified, based on the nuclear coordinates of transition:

- (i) ligand-to-metal charge transfer (LMCT).
- (ii) metal-to-ligand charge transfer (MLCT).

These CT transitions can be probed by UV-Vis or Raman spectroscopies³⁶⁻⁴⁰.

The LMCT results from the electronic transition between the highest occupied molecular orbital (HOMO), which is predominantly localized on the ligand, to the lowest unoccupied molecular orbital (LUMO), which is predominantly localized on the metal. This type of CT is commonly observed when complexes have

ligands with relatively high-energy polarizable lone pairs, as in the case of Br, S or Se, or when the metal in high oxidation states has low-lying empty orbitals with, as in the case of Mn(VII), Ir(IV), Cr(VI), Cd(II)^{37,39,41}. In contrast, the MLCT results when the electron transfers from a metal-centered HOMO to a ligand-centered LUMO. This kind of CT is commonly observed in complexes owing ligands with low-lying π^* orbitals, as in the case of aromatic ligands (e.g. bipyridine), or CO, CN^- and SCN^- ligands. The MLCT transition occurs at low energy (in the visible spectrum) if the metal ion has a low oxidation number, and therefore the d-orbitals will be relatively high in energy, e.g., Fe(II), Re(I), Ru(II), Ir(III) and Os(II), as shown in the schematic image^{36,38,42,43}, **Figure (1.3)**.

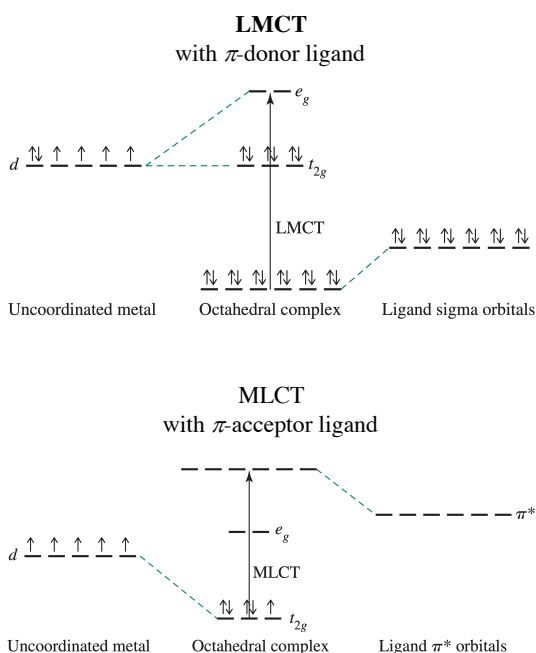


Figure (1.3). Diagram represents the MOs of the O_h -symmetrical complexes. The LMCT with π -donor ligand (**Top**) and MLCT with π -acceptor ligands (**Bottom**). [Reproduced from 'Ref. 43' with permission of the publisher]

The absorption band corresponding to the intramolecular electronic CT (ΔE) can be defined based on the ionization potential “ E_I ” (the required energy to remove the electron from HOMO orbital) of the D species and the electron affinity “ E_A ” (the energy release in filling the LUMO) of the A species, additional to the electrostatic attraction “ J ” between D and A, as shown in the **equation (1.1)** ^{44,45}.

$$E = E_I + E_A + J \quad (1.1)$$

The d^6 transition-metal complexes of Fe(II), Ru(II), Os(II) have grant much attention due to their electrochemical and photophysical properties. According to the ligand field theory, the complexes of these metals possess an O_h -symmetrical structure, which may be distorted depending on the ligands around the central metal.

The ligand field affects the d-d splitting of the metal center, and can be modulated by the ligand type or by its substituents ⁴⁶. Typically, the photophysical, photochemical, and electrochemical properties of the complex rely both on the ligand field around the central metal and on the metal itself and its oxidation state.

When we compare the transition metals of the 8th group in their M^{2+} oxidation state, we find that iron(II) complexes are kinetically labile, and that the low-lying metal-centered MOs shift MLCT transitions to very high energy ⁴⁷, **Figure (1.4-a)**. Contrarily to iron, ruthenium complexes are characterized by higher energy metal-centered orbitals, being therefore able to perform MLCT transitions at lower energy ⁴⁷, **Figure (1.4-b)**. Moreover, the singlet and triplet MLCT electronic states are close in energy, which grant Ru the ability to populate the relative long-lifetime excited state. However, 3MLCT and 3MC may be highly superimposed in such Ru-complexes, making the 3MC populated from the 3MLCT , and consequently, competition between radiative and non-radiative pathways occurs.

On the other hand, osmium complexes are kinetically inert but possess highly energetic d orbitals, the low-lying ligand-centered (π - π^*) MOs may be thus involved in MLCT⁴⁷, **Figure (1.4-c)**.

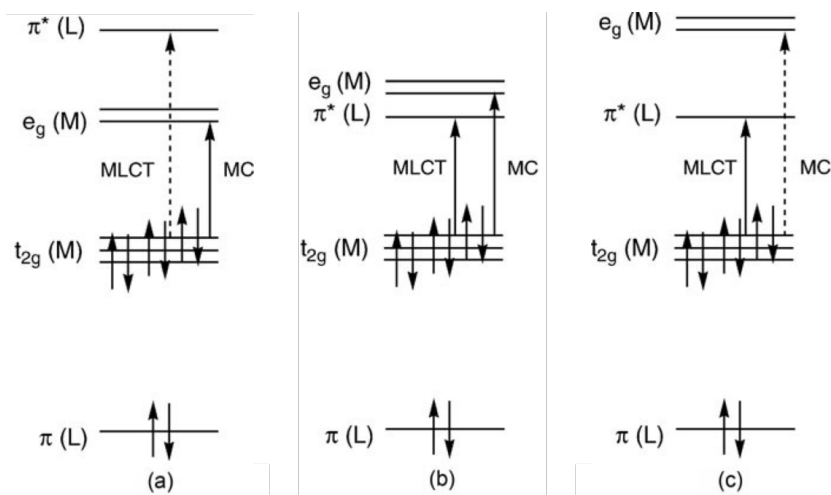


Figure (1.4). Schematic orbital diagram for a d^6 complex in an O_h -symmetrical environment, underlying most probable (solid arrows) and less probable (dashed arrows) transitions according to the relative energy of the $e_g(M)$ and $\pi^*(L)$. **(a)** Low-energy laying $\pi^*(L)$ and high-energy laying $e_g(M)$ “large destabilized $e_g(M)$ and large dd-splitting”; therefore more probability for MLCT and less accessible for populating the MC **(b)** Low-energy laying $\pi^*(L)$ and high-energy laying $e_g(M)$ “small destabilized $e_g(M)$ and small dd-splitting”; therefore accessible for populating both MLCT and MC. **(c)** High-energy laying $\pi^*(L)$ and low-energy laying $e_g(M)$ “large stabilized $e_g(M)$ and small dd-splitting”; therefore, less accessible for MLCT and high probability to populate the MC. [Reproduced from ‘Ref. 47’ with permission of the publisher]

1.1.1.3. Excited state theoretical concepts

Three main concepts rule these competing deactivation pathways, which are also vital for the understanding of the photophysical and photochemical properties for the photoactive molecules: the *molar extinction coefficient*, the *excited-state lifetime* and the *quantum yield*.

The *molar extinction coefficient* (ϵ) is an intrinsic property of the photoactive species and it is related to the light absorption by the Lambert-Beer law, **equation (1.2)**:

$$A = \log_{10} \left(\frac{I_0}{I} \right) = \epsilon l C; \text{ Therefore } \epsilon = A / l C \quad (1.2)$$

Where A represents the absorbance intensity, which is defined as the logarithmic ratio between incident (I_0) over transmitted (I) light radiation, thus being adimensional; ϵ represents the molar absorptivity in $M^{-1} \text{ cm}^{-1}$ unit; l represents the light path length or the thickness of the sample in the unit of cm; C represents molar concentration mol L^{-1} ⁴⁸.

The ϵ is related to the light-harvesting efficiency at a certain wavelength. The higher the molar extinction coefficient is, the more the molecule is able to absorb light, and therefore, the higher is the probability of populating its electronic excited states.

The *excited-state lifetime* (τ) is the time that a molecule stays in the excited state before returning in the ground state, and can be measured by observing the decay of fluorescence intensity after a short pulse-laser excitation or through monitoring the transient absorption spectroscopy ^{49,50}.

The lifetime is the reciprocal of the rate constant of the radiative and nonradiative decays **equation (1.3)**. The radiative decay lifetime of the photoactive species (the fluorophore) can range from picoseconds to hundreds of nanoseconds.

$$\tau(S_1) = 1 / (k_F + k_{IC} + k_{ISC} + k_Q[Q] + k_R). \quad (1.3)$$

In which, the efficiencies of the individual steps are:

$$\text{(Fluorescence):} \quad \eta_F = k_F \cdot \tau(S_1)$$

$$\text{(Internal crossing):} \quad \eta_{IC} = k_{IC} \cdot \tau(S_1)$$

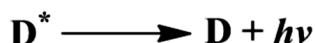
$$\text{(Intersystem crossing):} \quad \eta_{ISC} = k_{ISC} \cdot \tau(S_1)$$

$$\text{(Quenching):} \quad \eta_Q = k_Q[Q] \cdot \tau(S_1)$$

$$\text{(Other Radiative processes):} \quad \eta_R = k_R \cdot \tau(S_1)$$

As long as the molecule stays in the excited state, the fluorophore (D) is able to undergo diverse events (e.g., conformational changes, interacting with other molecular species, and rotate and diffuse through the local environment)⁴⁸.

For instance, if a molecule has fluorescence as the sole pathway for decay, such decay is given by the following equation:



Then, this I^{st} -order process can be expressed as: $d[D^*]/dt = -k_f[D^*]$

Therefore, the lifetime is given by the following mathematical expression:

$$\tau_f = 1/k_f$$

Where, τ_f represents the fluorescence excited state lifetime.

The integrated equation of the excited state can be expressed as:

$$[D^*] = [D^*]_0 e^{(-t/\tau_f)}$$

The *quantum yield* (Φ) is a feature related to the lifetimes and describes how efficiently a fluorophore converts the excitation light into fluorescence^{50,51}. Φ is defined as the ratio of the number of photons emitted to the number of photons absorbed, and therefore the maximum value of Φ is unity⁵²⁻⁵⁴. However, virtually any luminescent materials may reach unity, mainly due to competition with non-radiative processes that lead to partial depletion of the number of emitted photons.

$$\Phi = \frac{\text{Number of photons emitted}}{\text{Number of photons absorbed}} = \frac{I_{em}}{I_{abs}}$$

On the other hand, the quantum yield can be expressed by the ratio of the rate constants of the radiative (k_r) over the non-radiative (k_{nr}) processes, as shown in the following mathematical expression, **equation (1.4)**:

$$\Phi = \frac{\sum_i k_r}{(\sum_i k_r + \sum_i k_{nr})} \quad (1.4)$$

Where, k_r represents the rate-constant of the radiative deactivation processes (the fluorescence and phosphorescence). k_{nr} represents the rate constant of all non-radiative events that have been previously illustrated by Jablonski diagram.

Finally, the quantum yield can be also expressed in terms of the luminescence lifetime as the following mathematical expression, **equation (1.5)**:

$$\Phi = \frac{\sum_i k_r}{(\sum_i k_r + \sum_i k_{nr})} = \tau / \tau_F \quad (1.5)$$

1.1.1.4. Photo-induced electron and energy transfer processes

In binuclear (or multi-component) photosensitized assemblies, the excess energy of the absorbed light is dissipated either through charge (electron) transfer (CT) or energy transfer (ET) processes, **Figure (1.5)**. These processes may be exploited in photo-inducing or photo-catalyzing chemical reactions⁵⁵⁻⁵⁷.

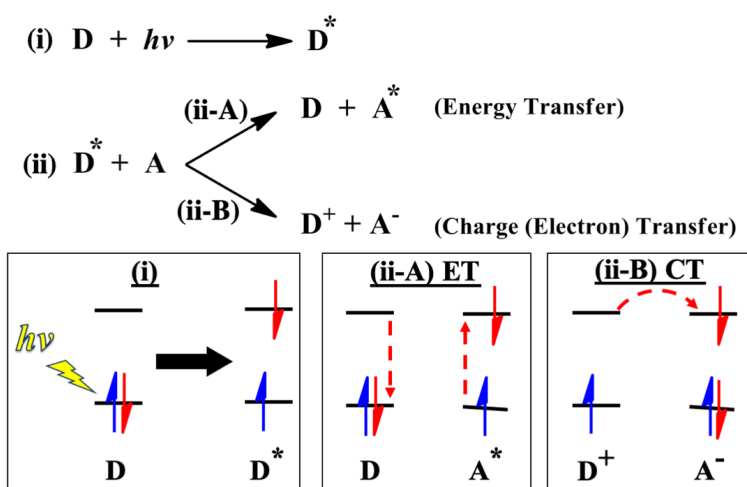


Figure (1.5). Schematic image representing the energy transfer (ET) and electron (charge) transfer (CT); photoabsorption by D forming a highly energetic (excited) state (D^*) (i). ET occurs, and producing excitation of A (A^*) (ii-A). CT occurs, and A accepts an electron, forming D^+ and A^- , the oxidized and reduced states, respectively (ii-B).

The understanding of the thermodynamic and kinetic aspects of the photo-induced energy and electron transfer processes between molecules and within supermolecular systems is vital to developing and design of robust photoactive systems. From the thermodynamics perspective, the photosensitizer must be able to induce the transfer of an electron or a hole, thus stabilizing charge separation between the two components, the donor/acceptor dyad⁵⁸. This charge separation relies on the redox potential (energy difference) of both species, as shown in the diagram, **Figure (1.6)**.

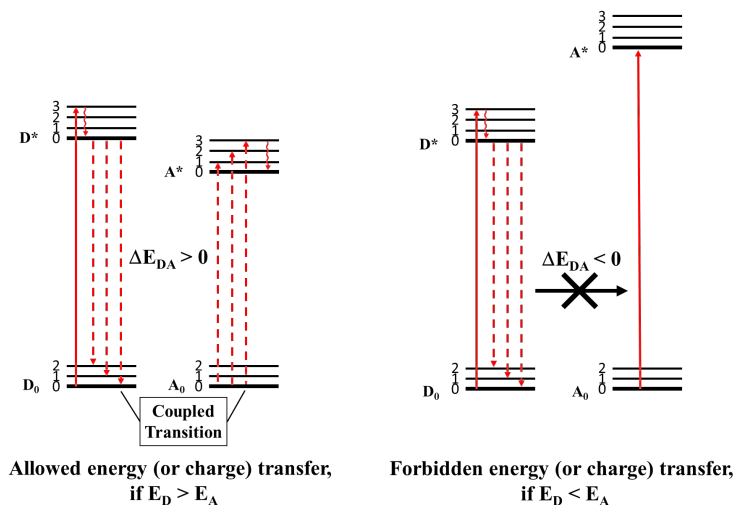


Figure (1.6). Left and right diagrams represent how the difference of the energy levels (or redox-potentials) between D and A governs the CT or the ET.

On the other hand, based on the kinetic point of view, the rate of CT or the ET relies on the excited state lifetime. If the lifetime of the excited state is sufficiently long (longer than $\sim 10^{-9}$ sec), the excited state (D^*) has higher chances to encounter the acceptor (A). Some specific weak interactions occur, which lead to the deactivation of the excited state by second-order kinetic processes^{57,59}, **Figure (1.7).**

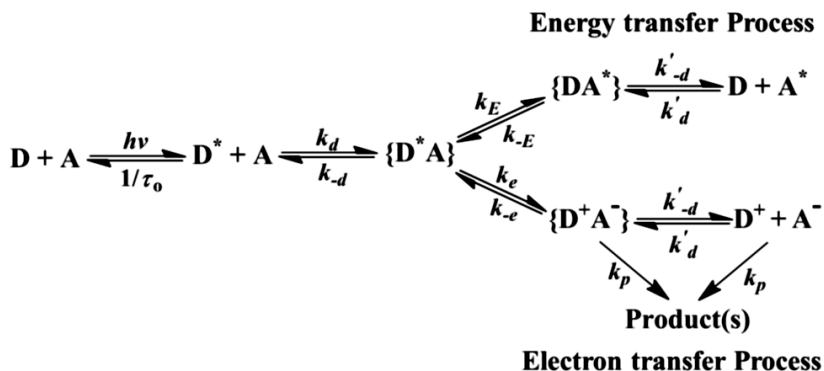


Figure (1.7). Representative kinetic mechanisms of the ET and CT processes. k_a is the diffusion rate constant of the D and A to form the adduct $\{D^*A\}$ in complex state, and then

through CT the successor complex $\{D^+A^-\}$ is transformed (k_e is the constant of activation reaction), and finally the dyad gets separated by diffusion constant k'_{-d} . The diffusion of the D and A is the slowest step in this mechanism; therefore, the total reaction is diffusion controlled.

The rate of electron transfer processes involving excited state molecules can be described based on Marcus theory^{55,60}. This electron transfer is thermally induced through geometrical reorganization of the surrounding molecules (e.g., the solvent), known as outer-sphere, and the ligands (inner-sphere), which create favorable geometric structures prior to the electron jump, **Figure (1.8)**.

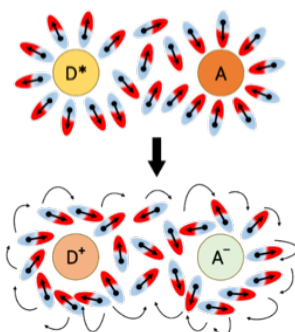


Figure (1.8). The schematic image represents the solvent reorganization dynamics that favors the electron-transfer of a dyad based on the Marcus model system. [Reproduced from 'Ref. 55' with permission of the publisher]

In the Marcus model⁵⁵, the solvent polarization plays a significant role to determine the free-energy of activation of the CT and therefore its rate. The initial and final states of the electron transfer in the excited molecules are formalized as potential energy curves, and the calculated free-energy change (ΔG) involves the redox potential of the formed excited state couple ($\{D^*A\}$), **Figure (1.9)**.

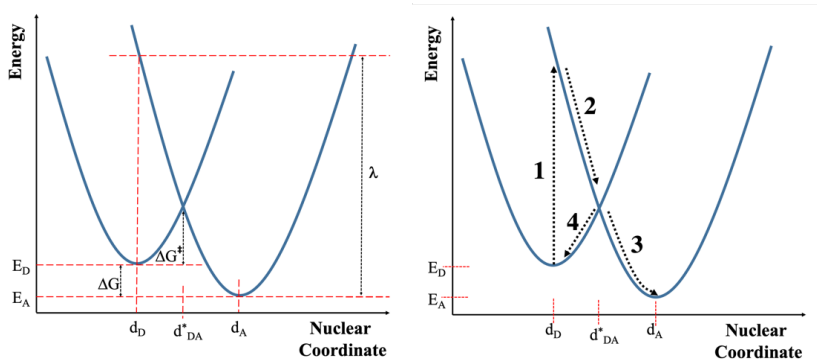


Figure (1.9). Diagram represents the potential energy curves that are formalized by the Marcus model and summarizes some thermodynamic parameters (**Left**) and electron transfer dynamics (**Right**), which shows the relationship between optical (1), photo-induced (2 and 3), and thermal back (4) electron transfer processes in supramolecular species. [Reproduced from 'Ref. 55' with permission of the publisher]

Another important class of the excited state energy dissipation is through energy transfer. Both states involved are locally excited, but the excitation is localized in different parts of the molecule or on different molecules. In ET, there are three suggested mechanisms; one radiative and two non-radiative mechanisms:

- (i) The radiative ET, known as trivial ET.
- (ii) The non-radiative Förster ET (FRET) mechanism, in which the ET is ruled by the electrostatic coupling of the transition dipole moments of the dyad that stimulates the deactivation of the excited state of D and the excitation of A ⁶¹. This type is effective at distances in several nm, and its rate is orientation and distance-dependent (inversely related to the sixth power of the distance).

- (iii) The non-radiative Dexter (also known as exchange) mechanism, which is a short-range mechanism and requires the overlapping between both the excited and the ground electronic states ⁶¹. In this mechanism, a simultaneous opposite electron-transfer occurs between the excited and ground states of both dyads

The Dexter ET mechanism is predominant as long as both dyads are effectively touched, and it is competitive with the Förster mechanism for the singlet excitation energy transfer but vastly faster than the Förster mechanism for triplet excitation energy transfer, **Figure (1.10)**.

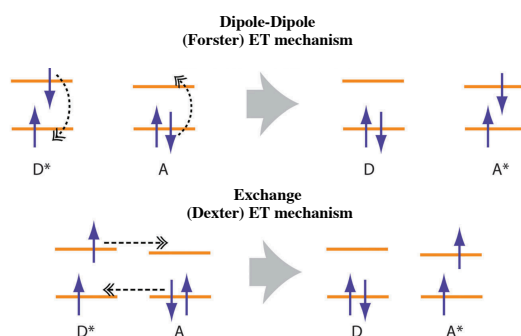


Figure (1.10). Diagram represents the energy-transfer dynamics based on (dipole-dipole) Förster mechanism (**Top**), and (exchange) Dexter mechanism (**Bottom**). [*Reproduced from 'Ref. 61' with permission of the publisher*]

1.1.2. Triplet-state [Ru^{II}-polypyridine] photosensitizers

The triplet-state photosensitizers (triplet-PSs) are gaining increasing interest in several fields, such as in electroluminescence ⁶², phosphorescent bioimaging ⁴⁶, molecular sensing ⁶³, photodynamic therapy (PDT, via sensitization of singlet oxygen, ¹O₂) ^{12,64}, photoinitiated polymerization ⁶⁵, and more recently, photocatalysis ⁶⁶. An ideal triplet-PS should show strong absorption features in the visible light, high triplet state quantum yields (effective ISC), and a long-lived triplet excited state. However, it is still hard to design a triplet PS with

predetermined ISC property, due to the lack of recognized relationship between the ISC and molecular structures.

The ruthenium-based polypyridine complexes are characterized by absorbing the light at the visible region of the spectrum, populating the singlet state of the MLCT ($^1\text{MLCT}$), and the strong phosphorescence generated from the relaxation of the triplet-MLCT state ($^3\text{MLCT}$) after ISC. Such electronic transition is due to the low energy difference between the singlet and triplet states of the MLCT states in ruthenium complexes ⁶⁷. Nevertheless, the probability of non-radiative deactivation due to the population of the metal-centered triplet state (^3MC) represents a possible drawback, which may cause the ligand loss, **Figure (1.11)**.

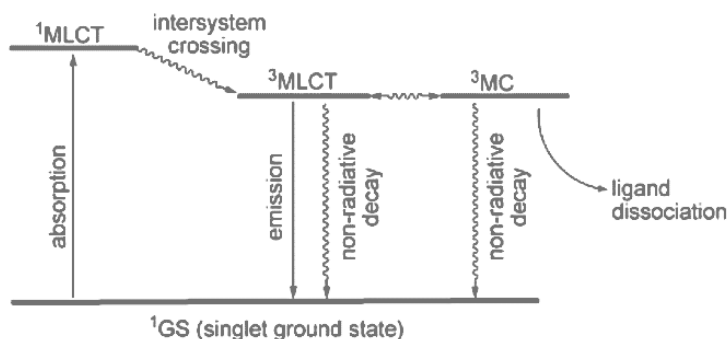


Figure (1.11). Simplified Jablonski diagram for Ru^{II}-based polypyridine complexes. [Reproduced from 'Ref. 47' with permission of the publisher]

Ruthenium(II) tris(bipyridine) ($[\text{Ru}^{\text{II}}(\text{bpy})_3]$) and ruthenium(II) bis(terpyridine) ($[\text{Ru}^{\text{II}}(\text{tpy})_2]$) and their derivatives are considered as the prototypical triplet-PS compounds. These triplet chromophores are able to perform either reductive, **4** in **Figure (1.12)** or oxidative, **4'** in **Figure (1.12)** single electron transfer (SET) ⁶⁸.

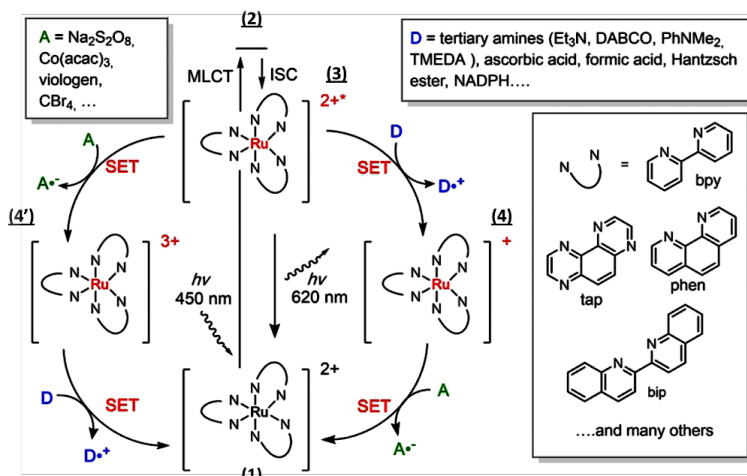


Figure (1.12). The schematic image represents the oxidative and reductive pathways of Ru^{II} -based polypyridine complexes photochemistry. [Reproduced from 'Ref. 68' with permission of the publisher]

The Ru^{II} -complex, **1 in Figure (1.12)**, after absorbing the visible-light radiation, promotes one electron from the metal-centered t_{2g} orbital to the ligand-centered π^* orbital, generating the $^1\text{MLCT}$ electronic state, **2 in Figure (1.12)**. The ruthenium metal is formally photo-oxidized to $[\text{Ru}^{\text{III}}]$, while the ligand undergoes a single-electron reduction. The initially photo-generated singlet state is short-lived ($\sim 10^{-15}$ s), and rapidly undergoes intersystem crossing (ISC) to yield a long-lived $^3\text{MLCT}$, **3 in Figure (1.12)**. In this state, the electron-spin inversion occurs, and the electronic configuration of this state can be described as $^3[(d(\pi)^5 (\pi_{\text{ligand}})^1)]$. This triplet state has a long lifetime because the conversion to the singlet state is spin-forbidden. The highly energetic $^3[\text{Ru}^{\text{II}}(\text{bpy})_3]^{2+*}$ has stronger oxidation and reduction potentials (-0.86 and +0.84 V), if compared to the ground state (+1.26 and -1.23 V, respectively) ^{69,70}. Therefore, this dual nature of the excited state enables it to engage either reductive SET in the presence of a donor (D) to produce $[\text{Ru}^{\text{I}}]$, **4 in Figure (1.12)** or oxidative SET in the presence of an acceptor (A) to produce $[\text{Ru}^{\text{III}}]$, **4' in Figure (1.12)**.

1.1.3. Structural and functional aspects of [Ru^{II} tris-bidentate] and [Ru^{II} bis-tridentate] complexes

[Ru^{II}(bpy)₃] is the first reported analogue of Ru^{II}-based tris-bidentate complexes, in 1959 by Paris and Brandt ⁷¹. It is characterized by a relatively strong absorption band located in the visible ($\lambda_{\text{max}} = 460 \text{ nm}$) with high extinction coefficient ($\sim 14,400 \text{ M}^{-1}\cdot\text{cm}^{-1}$), notable fluorescence emission ($\lambda_{\text{max}} = 610 \text{ nm}$), and long excited-state lifetime ($\sim 1,100 \text{ ns}$) ^{67,72}. However, octahedral tris-bidentate metal complexes (e.g., [Ru^{II}(bpy)₃]), owing to a stereogenic metal-center, exist in two isomeric forms (Λ and Δ), **Figure (1.13, A)** ⁷³. This leads to some implications when preparing multinuclear assemblies, where the isolated samples usually reflect statistical mixtures of the two possible isomers. Additional stereoisomerism has to be considered when two (or three) of the bipyridyl ligands are unsymmetrically substituted. For instance, complexes of the type [Ru^{II}(bpyR)₃], bpyR is an unsymmetrical ligand, show *fac* and *mer* geometrical isomers, **Figure (1.13, B)** ⁷³.

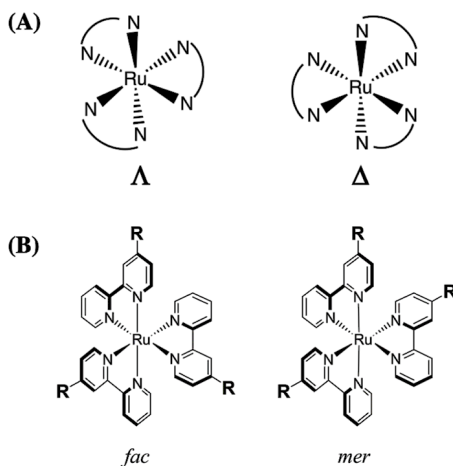


Figure (1.13). Geometrical isomers of, [Ru^{II}(bpy)₃] the Λ (Left) and Δ (Right) isomers (A). The substituted [Ru^{II}(bpyR)₃] with unsymmetrical ligands (B). [Reproduced from 'Ref. 73']

If different substituents are considered, four geometric isomers will exist, **Figure (1.14)**, which become eight when the third bpy is also substituted with a different ligand. Each of them may show distinct photophysical properties and synthetic complexity ^{74,75}.

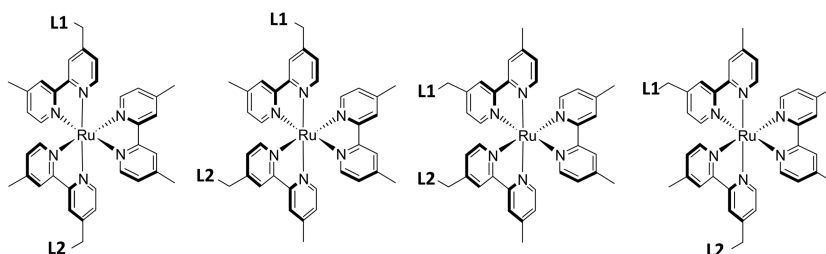


Figure (1.14). Geometrical isomers of a general $[\text{Ru}^{\text{II}}(\text{bpyL}^1)(\text{bpyL}^2)(\text{bpy})]$ with two unsymmetrical ligands. [Reproduced from 'Ref. 73']

In contrast, the $[\text{Ru}^{\text{II}}(\text{tpy})_2]$ has only a trans configuration, **Figure (1.15)**. The structural linearity and isomeric purity obtained in multiunit assemblies with substitution along the **C2** axis of the tpy-ligand, makes it attractive ⁷⁶. Unfortunately, it owns a weak absorption band in the visible region ($\lambda_{\text{max}} \sim 475$ nm) with extinction coefficient $< 10,000 \text{ M}^{-1} \cdot \text{cm}^{-1}$, and weak fluorescence emission, and short excited-state lifetime in the order of picoseconds (~ 250 ps) ^{67,77,78}. The two bulky and strained tridentate terpyridine ligands, in order to surround the metal, cause a bit distortion of the O_h -symmetry, meanwhile disturbing the tpy-ligands aromaticity. This distortion produces a weak ligand field, low d-d splitting. The $^3\text{MLCT}$ becomes closer to the ^3MC state, harvesting the $^3\text{MLCT}$ population by thermally non-radiative deactivation.

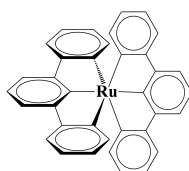


Figure (1.15). Chemical structure of $[\text{Ru}^{\text{II}}(\text{tpy})_2]$ with trans-configuration.

Many efforts have been reported in manipulating the energy difference between the $^3\text{MLCT}$ and ^3MC states, either by stabilizing the $^3\text{MLCT}$ or destabilizing the ^3MC ⁷⁹. In order to achieve such stabilization of the $^3\text{MLCT}$ or destabilization of ^3MC states, substituted ligands have been synthesized with electron-withdrawal or donation tendencies, respectively. For instance, the use of acetylene substituents in the 4'-position promoted long excited-state lifetimes ^{27,80–83}, **Figure (1.16)**.

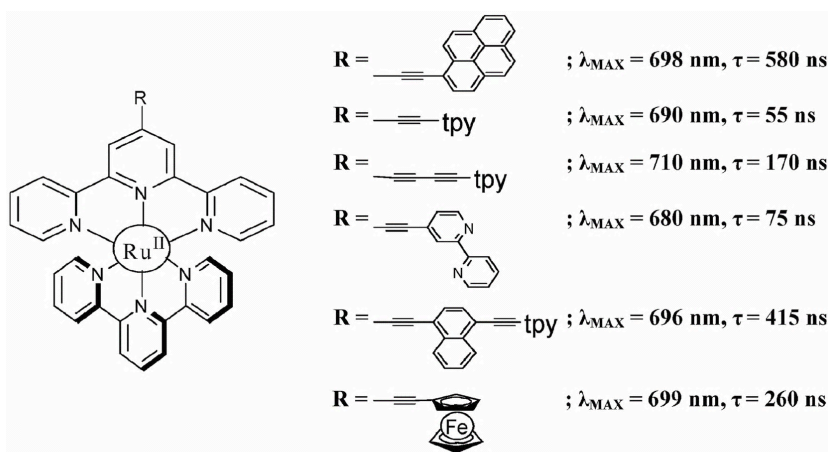


Figure (1.16). Some acetylene-substituted $[\text{Ru}^{\text{II}}(\text{tpy})_2]$ and related photophysical data. [Reproduced from 'Ref. 27' with permission of the publisher]

Other efforts were focused on enhancing the photophysical properties of the ruthenium(II) bis-tridentate ligands (e.g. $[\text{Ru}^{\text{II}}(\text{tpy})_2]$) by using aromatic substituents (i.e., phenyl-groups) on the 4'-position, **Figure (1.17)**. The complex $[\text{Ru}^{\text{II}}(\text{tpy-Ph})_2]$ and its analogues have luminescence lifetimes of approximately 4 ns. Although other strategies have been reported in the literature ^{27,84}, most of its congeners lose some or all of the essential properties of a sensitizer such as proper redox potential or excited-state energy.

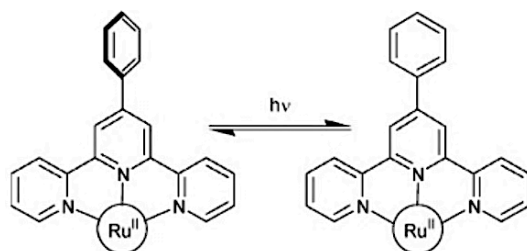


Figure (1.17). The schematic image represents the twisting on the phenyl-substituent on the coordinated tpy-ligand for co-planarity phenomenon; Non-planar (**Left**), and co-planar (**Right**). [Reproduced from 'Ref. 27' with permission of the publisher]

Further studies were focused on studying different tris-heteroleptic polypyridine complexes in the form of $[\text{Ru}(\text{tpy})(\text{bpy})\text{L}]$ where L represents a mono-dentate ligand, with the aim to minimize the strain of the tridentate-ligand ²⁷. Such complexes have gained attention as photosensitizers in different fields, such as dye-sensitized solar cells (DSSCs) ⁸⁵, unimolecular water oxidation ⁸⁶, hydrogen photosynthesis ⁸⁷, and labeling of biological systems ⁸⁸. Tris-heteroleptic Ru^{II} -complexes have reported enhanced photophysical and chemical features, without the drawbacks of a stereogenic metal center ⁸⁸, **Figures (1.18)**.

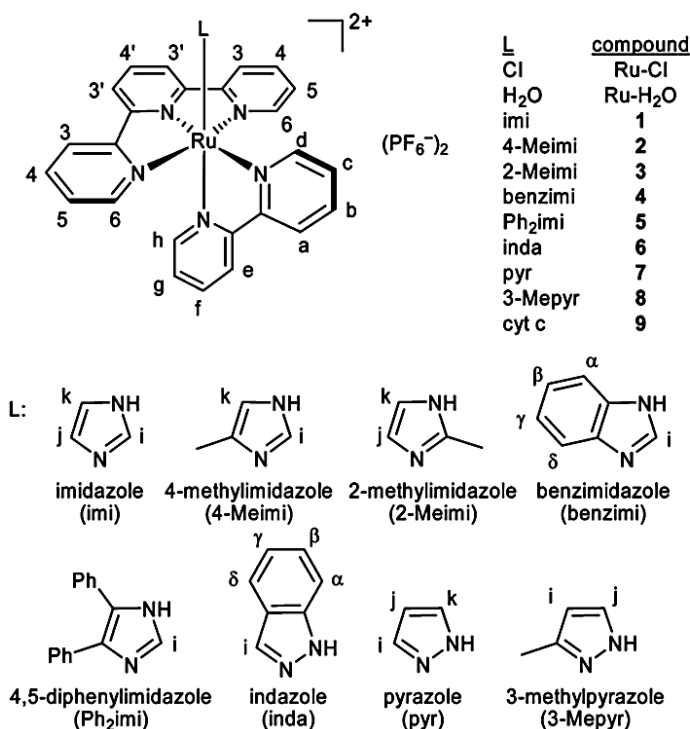


Figure (1.18). Heteroleptic ruthenium(II) polypyridine complexes as photosensitizers with imidazole-based monodentate ligands. [Reproduced from 'Ref. 88' with permission of the publisher]

1.1.4. Photosensitization of native proteins

Electron transfer is a fundamental process in biological systems, such as photosynthesis, respiration and redox-mediated enzyme catalysis. Therefore, the understanding of the peptide and the protein roles in mediating long-range electron transfer has been and it is still the aim of several studies, in which ruthenium(II) complexes have been frequently used as photosensitizers^{33,39,88-92}.

The unique photochemical properties of the [Ru^{II}(bpy)₃] prototype and its derivatives have rendered these complexes valuable in triggering electron transfer processes^{93,94}. Then, Ru^{II}-polypyridine modified proteins have found wide

application in the field of light-driven biocatalysis, which has been studied in several catalytically-competent metalloproteins, such as hydrogenases, carbon monoxide dehydrogenase, nitrogenase, laccase and cytochrome P450 BM3⁹⁵. Early successes in the photo-activation of small molecules helped in moving the field towards harnessing the catalytic potential of enzymes. Indeed, metalloenzymes present unique structural features and catalytic efficiency rarely matched by small molecule models⁹⁶⁻¹⁰¹.

Early attempts at electron transfer studies or light-driven biocatalysis have used $[\text{Ru}^{\text{II}}(\text{bpy})_3]$ complex in solution with the metalloprotein of interest. This bimolecular process often resulted in marginal CT/catalysis. Hence, strong efforts have been devoted to covalently attach the photosensitizer to metalloproteins in order to promote unimolecular electron transfer reactions, which promoted the development of various strategies for the selective attachment of the ruthenium(II) complexes by taking advantage of the tunable reactivity of the amino acid side chains.

Cytochrome *c* (Cc), a small heme protein, has been widely adopted in many seminal studies as the prototypical one-electron carrier of the electron transport chain in mitochondria⁶⁸. It undergoes oxidation and reduction processes upon conversion of the iron cofactor between $[\text{Fe}^{\text{II}}]$ and $[\text{Fe}^{\text{III}}]$ states. Cc is a well-studied system for photo-induced electron transfer through conjugated and diffused forms of ruthenium-based photosensitizers, with a moderately slow process that can be followed by steady-state spectroscopy experiments¹⁰².

Initial reports, published by Gray and coworkers, involved the direct attachment to histidine residues of either horse heart cytochrome *c* or azurin, of aquo complexes, such as $[\text{Ru}^{\text{II}}(\text{NH}_3)_5(\text{H}_2\text{O})]$ ^{103,104}, $[\text{Ru}^{\text{II}}(\text{bpy})_2(\text{Im})(\text{H}_2\text{O})]$ or $[\text{Ru}^{\text{II}}(\text{tpy})(\text{bpy})(\text{H}_2\text{O})]$. Few years later, peptide coupling strategies have resulted

in the attachment of ruthenium(II) complexes bearing amino or carboxylic acid moieties to site-specific Cys and Lys residues ¹⁰⁵.

Other efforts were also reported by C. Janiak and coworkers, where compounds of the form $[\text{Ru}^{\text{II}}(\text{bpy})(\text{tpy})\text{L}]$ ($\text{L} = \text{H}_2\text{O}$, imidazole (imi), 4-methylimidazole, 2-methylimidazole, benzimidazole, 4,5-diphenylimidazole, indazole, pyrazole, 3-methylpyrazole) have been synthesized, and the coupling between the $[\text{Ru}^{\text{II}}(\text{bpy})(\text{tpy})]$ fragment from the Ru-aqua complex to His44 of the cytochrome c (Yeast iso-1) was performed. This study aimed to use the $[\text{Ru}^{\text{II}}(\text{bipy})(\text{terpy})\text{L}]$ instead of $[\text{Ru}^{\text{II}}(\text{bipy})_2(\text{H}_2\text{O})\text{L}]$ ($\text{L} = \text{H}_2\text{O}$ or imidazole) in order to simplify the synthetic difficulties by using the former complex, which was providing only one open coordination site for protein conjugation ⁸⁸, **Figure (1.19)**.

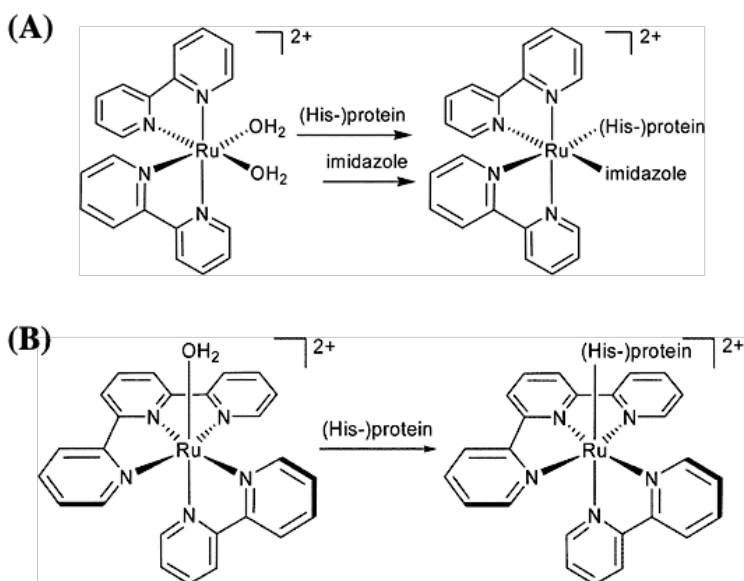


Figure (1.19). Reaction scheme shows (A) the two free sites in the $[\text{Ru}^{\text{II}}(\text{bpy})_2(\text{H}_2\text{O})_2]$ can be bonded by imidazole. (B) the tpy-analogues, the $[\text{Ru}^{\text{II}}(\text{bpy})(\text{tpy})(\text{H}_2\text{O})]$, as precursors for protein coupling, which provides only one coordination site remaining to be occupied by the protein, hence the protein coupling can be simplified to a one-step reaction.

[Reproduced from 'Ref. 88' with permission of the publisher]

Peters and coworkers attached ruthenium(II) complexes to [NiFe]-hydrogenases, by conjugating the amino group of a $[\text{Ru}^{\text{II}}(\text{bpy})_2\text{PhenA}]$ complex (PhenA = 5-amino-1,10-phenanthroline) to the carboxylic acid side chains of aspartic or glutamic acids in the presence of crosslinking carboxydiimide reagents. Enhancement of the photocatalytic hydrogen production occurred by the conjugated adduct if compared with the freely diffusing system. Furthermore, sustained hydrogen production occurs even in the presence of oxygen, by presumably creating a local anoxic environment through the reduction of oxygen (effected by ruthenium), similarly to what has been proposed for oxygen tolerant hydrogenases ¹⁰⁶.

On the other hand, Lakowicz has reported the conjugation of an asymmetrical ruthenium(II) complex, the $[\text{Ru}^{\text{II}}(\text{bpy})_2(\text{dcbpy})]$ (where dcbpy = 4,4'-dicarboxy-2,2'-bipyridine) to the amino side chain of lysine residues. The latter complex may be used as luminescent probe for measuring the rotational motions of proteins, such as human serum albumin, concanavalin A (ConA), human immunoglobulin G (IgG), and ferritin. Reported data demonstrate that the probe can be used to measure rotational motions on the 10ns to 1.5ps time scale, previously inaccessible using common luminescence methods. The author suggested that the $[\text{Ru}^{\text{II}}(\text{bpy})_2(\text{dcbpy})]$ probe could be regarded as the first of a class of metal-ligand complexes, each with different chemical reactivity and spectral properties, for studies of macromolecular dynamics ¹⁰⁷. Indeed, the isocyanate moiety on a phenanthroline ligand has been introduced to facilitate the lysine conjugation, in luminescence applications ^{107,108}.

Ultimately, the cysteine residue, with its high nucleophilicity and lower natural abundance, is very attractive as a selective target for covalent attachment to various photosensitizers ¹⁰⁹. Sulfhydryl-specific labeling has been achieved via the introduction of reactive maleimide ^{110,111}, bromoalkyl ¹¹², and iodoacetamide

substituents onto various luminescent complexes ¹¹³. Only recently, Dwaraknath reported the selective sulfhydryl ring opening of an epoxide moiety from a 5,6-epoxy-5,6-dihydro-1,10-phenanthroline ligand. Moreover, a totally alternative coupling strategy involved direct functionalization of protein metal cofactors, such as the prosthetic heme group in reconstituted heme proteins ^{114,115}, or the pterin cofactor of the inducible nitric oxide synthase, with ruthenium(II) complexes ¹¹⁶, **Figure (1.20)**. This strategy in principle allows for better and faster electron-tunneling effect, thus increasing the efficiency of the CT process.

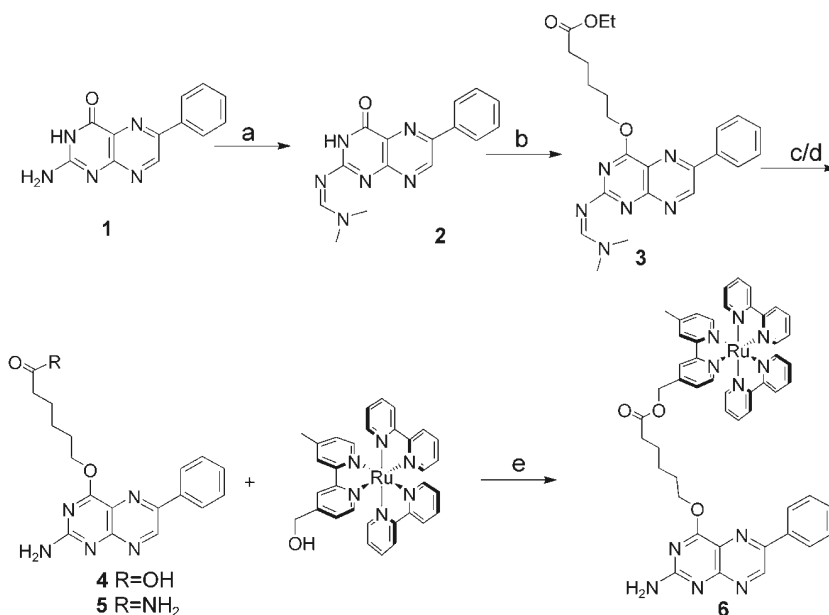


Figure (1.20). Synthetic approach for Ruthenium(II) pterin probes. [Reproduced from 'Ref. 116' with permission of the publisher]

1.2. Aims (chapter 1)

Herein, we present the design and synthesis of a tris-heteroleptic ruthenium(II) complex of the form $[\text{Ru}(\text{tpy})(\text{bpy})\text{L}]$, where L is the monodentate isonicotinic acid (pyCOOH). This Ru-complex is not stereogenic and holds one electron-withdrawing carboxyl group at the monodentate ligand. We will show that this substituent shows several advantages in photosensitization as well as in bioconjugation.

Indeed, the carboxyl moiety, thanks to its electron-withdrawing properties, may eventually stabilize the $^3\text{MLCT}$ state, and increase the gap between the $^3\text{MLCT}$ and ^3MC states, as reported in several analogous systems in literature ^{76,79,117}. Consequently, we will show the enhancement of the photophysical and photochemical properties, by (i) a steady-state spectroscopic analysis, (ii) a theoretical treatment of the electronic features, and (iii) a kinetic study of a prototypical photon-induced electron transfer.

Furthermore, the carboxyl functional group can be easily conjugated to other biomolecular systems. For these tasks, biomolecular active residues (N-terminal backbone, Lys and His side chains) must be targeted through several bio-orthogonal or crosslinking conjugation techniques, as illustrated in the Scheme of **Figure (1.21)**. This versatility, simplicity, and the lack of isomeric forms make this complex particularly convenient for developing easy and tunable routes to efficient photosensitized assemblies.

Pre-activation

Bio-orthogonal Cojugates

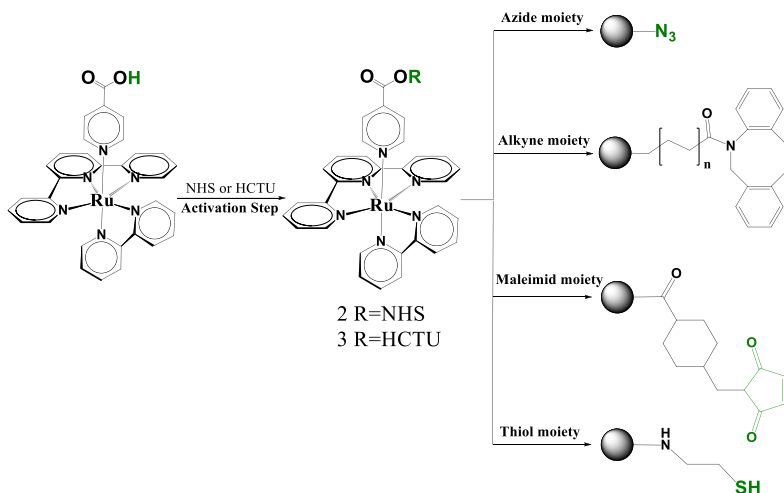


Figure (1.21). Schematic representation of the bio-conjugate and crosslinking approaches with $[\text{Ru}(\text{tpy})(\text{bpy})\text{L}]$, where L is a monodentate ligand holding carboxyl moiety at the position 4-of the bpy ligand. (i) Activating the carboxyl group with a bio-activating agent (e.g., NHS, HCTU, DIC ...), or (ii) through constructing a crosslinking rout to bio-molecular systems (e.g., Azide, DBCO, Melamine, or thiol moieties).

ù

1.3. Result and Discussion

1.3.1. Synthesis and characterization of a new ruthenium(II) polypyridine complex

The primary goal of the present study is the development of a ruthenium complex convenient in photosensitization of biomolecules. Such complexes should have the following features: (i) stable and active in photo-inducing catalysis; (ii) fast and simple coupling protocol with bio-molecular systems; (iii) lack of stereoisomers to prevent additional purification steps.

To match such requirements, tris-heteroleptic complexes represented the trivial choice. In fact, the monodentate ligand could be opportunely chosen/decorated with the desired functional group. Our attention fell on the isonicotinic acid (pyridine-4-carboxylic acid), because carboxyl group may be easily functionalized, the pyridine ligand cannot be easily displaced by proteinogenic ligands (imidazole from histidine, thiol from cysteine, etc.) and it is a low-cost commercially available reagent. Therefore, we synthesized a Ru^{II}-complex in which terpyridine (2,2';6'2''-terpyridine) (**tpy**), bipyridine (2,2'-bipyridine) (**bpy**), and isonicotinic acid (**pyCOOH**) were used as ligands, **Figure (1.22)**.

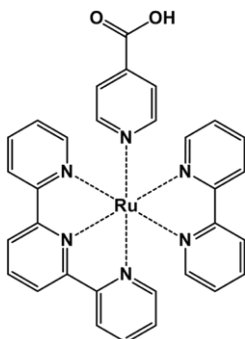
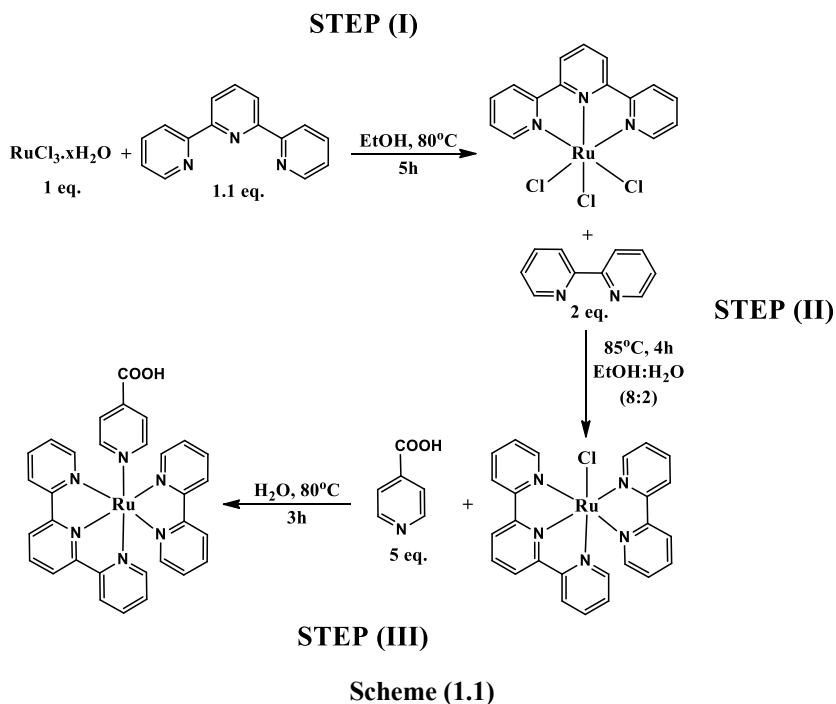


Figure (1.22). Schematic structure of the synthesized tris-heteroleptic Ru^{II}-polypyridine complex [Ru^{II}(bpy)(tpy)(pyCOOH)].

A modified and optimized synthetic protocol has been followed to synthesize the new ruthenium complex, $[\text{Ru}^{\text{II}}(\text{bpy})(\text{ypy})(\text{pyCOOH})]\cdot\text{X}_2$ (where $\text{X} = \text{Cl}^-$, TFA^- or PF_6^-), maximizing purity, yield and reagent consumption. Starting from the commercially available RuCl_3 , the stepwise process for each ligand is reported in **Scheme (1.1)**.



The first, **step I in Scheme (1.1)**, consists in reacting 1eq. of $\text{RuCl}_3\cdot x\text{H}_2\text{O}$ with 1.1eq of the tpy-ligand in ethanol (EtOH) as the solvent under 80°C for 5h. A dark greenish precipitate was produced, corresponding to $[\text{Ru}^{\text{III}}(\text{tpy})(\text{Cl})_3]$ (**1**), which was collected by centrifugation for the next step.

In the second step, **step II in Scheme (1.1)**, complex **1** was reacted with the bpy-ligand. The reaction was carried out by mixing 1eq of **1** with 2eq of the bpy-ligand in 80:20 (v/v) EtOH: H_2O as the solvent under 85°C for 4h. A soluble dark-red colored complex was obtained in the reaction mixture. The $[\text{Ru}^{\text{II}}(\text{bpy})(\text{tpy})(\text{Cl})]$

(2) complex was purified from the crude by reversed-phase flash chromatography (RP-LC), and collected for the last synthetic step.

In the third step, **step III in Scheme (1.1)**, pyCOOH was anchored on complex **2** to get the desired $[\text{Ru}^{\text{II}}(\text{bpy})(\text{tpy})(\text{pyCOOH})]$ (**3**). The reaction was carried out by mixing 1 eq of **2** with 5 eq of the pyCOOH in water under 80°C for 3h. A dark-orange reaction mixture was obtained, which indicates the formation of the desired Ru^{II} -complex (**3**).

1.3.1.1. Reaction monitoring and product formation

UV-Vis absorption spectroscopy and RP-HPLC were used to monitor the reaction progress. UV-Vis spectra were collected at different time at 0, 1 and 4 h, during the reaction progress of **step (II)**, **Figure (1.23)**. A broad band centered at $\lambda_{\text{max}} = 500 \text{ nm}$ corresponding to the $^1\text{MLCT}$ transition appeared, with the concurrent decrease of the bands in the near UV-region, corresponding to the free-bpy precursor. These changes in the UV-Vis spectra are indicating the coordination of the bpy ligand to **1**, and the concomitant formation of complex **2**.

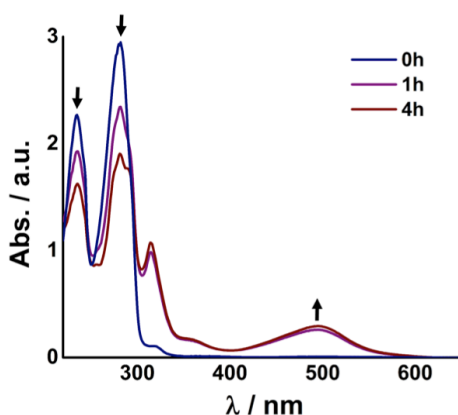


Figure (1.23). UV-Vis spectra showing the reaction progress during the **step II** (0, 1, and 4 h). The arrows indicate the peak shift along with the time course.

HPLC chromatograms have been collected during the **step II** reaction progress, **Figure (1.24, A)**. They show an increasing peak at 17.7 min, corresponding to the formation of **2**, together with the concomitant decreasing of a peak at 3.0 min, corresponding to the depletion of the bpy ligand.

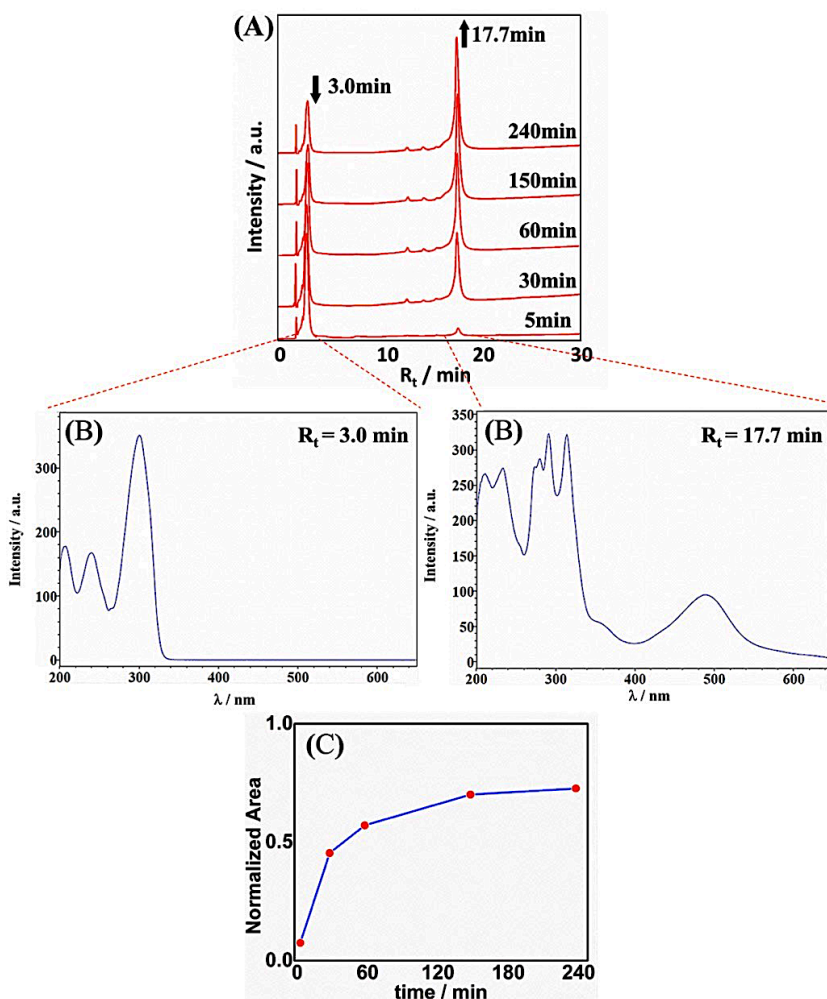


Figure (1.24). RP-HPLC reaction monitoring for the formation of **2** (500 nm). HPLC analysis was conducted by injecting 15 μL of water-diluted reaction aliquots at different time (5, 30, 60, 150, 240 min) (A). UV-vis spectra of the eluted peaks (B). Area of the peak at 17.7 min was plotted against time to follow reaction progress (C).

UV-Vis spectra of the eluted species were collected during the chromatography, **Figure (1.24, B)**, confirming the previous assignment for both the reactant and the product. The reaction progress could be followed by plotting the integration of the peak corresponding to **2** against time **Figure (1.24, C)**. A plateau is reached after approximately 2.5h, suggesting that the reaction reached equilibrium. Longer reaction time induced the conversion of **2** to the aqua-coordinating analogue **2-H₂O**, where water displaces the chloride in the axial position.

The same UV-Vis analysis was conducted for monitoring the formation of complex **3**, during **step III**, **Figure (1.25)**. The following could be noted: **(i)** prior to pyCOOH addition a MLCT band at 480 nm could be observed, corresponding to **2-H₂O**, which is formed under aqueous reaction conditions; **(ii)** after 10 min, absorbance intensity of the MLCT increases, along with a hypsochromic shift and broadening ($\lambda_{\text{max}} = 425$ nm) clearly visible after 1h of reaction; **(iii)** the band at 300 nm (corresponding to free pyCOOH precursor) almost completely disappears, and a new band at λ_{max} ca. 280 nm emerges.

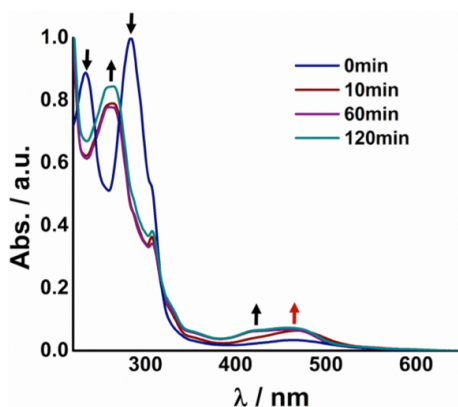


Figure (1.25). UV-Vis spectra showing the reaction progress during the **step III** (after 0, 10, 60, and 120 min). The arrows indicate the peak shift along with the time course.

HPLC chromatograms have been collected during the **step III** reaction progress, **Figure (1.26, A)**. They show an increasing peak at 14.6 min, corresponding to the

formation of **3**, together with the concomitant disappearance of a peak at 13.9 min, corresponding to the consumption of **2-H₂O**. It should be noted that the absence of the peak at 17.7 min has been attributed to the fast exchange of the Cl⁻ ligand with water under the adopted reaction conditions.

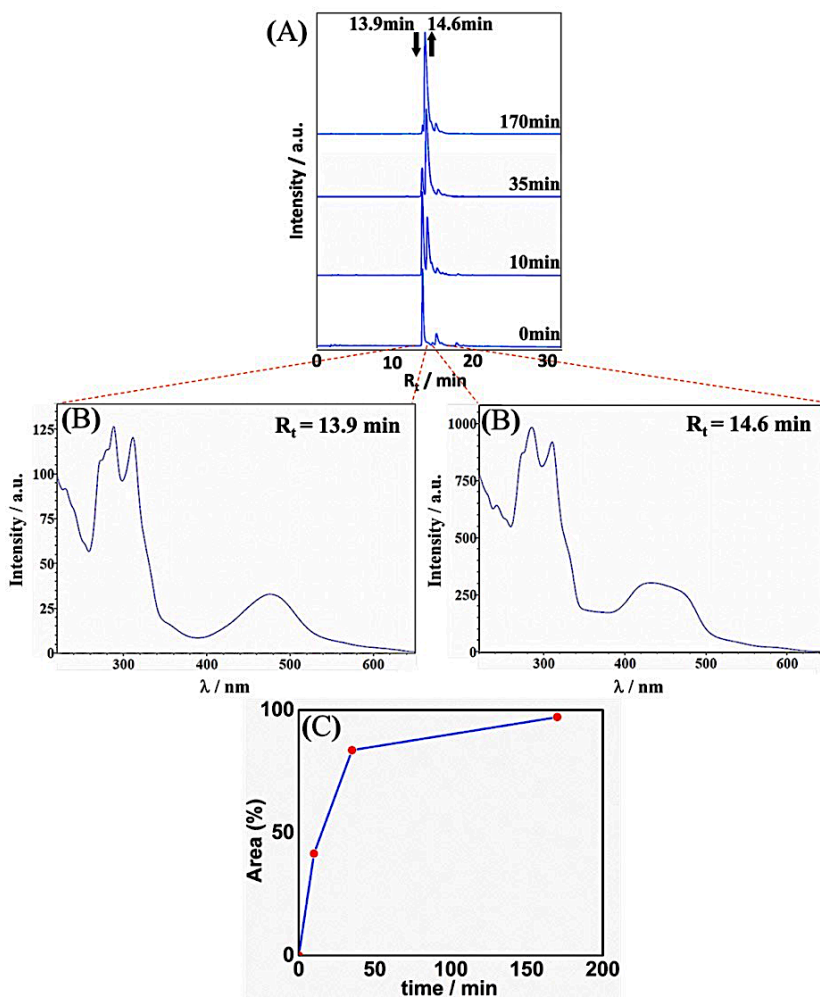


Figure (1.26). RP-HPLC reaction monitoring for the formation of **3** (425 nm). HPLC analysis was conducted by injecting 15 μL of water-diluted reaction aliquots at different time (0, 10, 35, 170 min) (A). UV-vis spectra of the eluted peaks (B). Area of the peak at 14.6 min was plotted against time to follow reaction progress (C).

UV-Vis spectra of the eluted peaks have been collected, **Figure (1.26, B)** and confirmed the interpretation of the previous spectroscopic analysis of the reaction mixture. As in the previous step, reaction progress could be followed by plotting the normalized area of the peak at 17.7 min versus time, **Figure (1.26, C)**. Almost complete conversion could be observed after 3h.

From both spectroscopic and chromatographic techniques, it was found that the complex **2** ($\lambda_{\text{max}} \approx 500$ nm, $R_t \approx 17$ min) was exchanging to the aqua-complex ($\lambda_{\text{max}} \approx 480$ nm, $R_t \approx 13$ min. To confirm that **2-H₂O** was the actual precursor of **3**, a solution consisting of the pure eluted fractions from both complexes was diluted in methanol and investigated by HPLC. The HPLC profile, **Figure (1.27)** showed two well-separated peaks, one at earlier retention-time (R_t 12 min; MLCT band at $\lambda_{\text{max}} \approx 480$ nm) and the second at later retention time (R_t 16.5 min; MLCT band at $\lambda_{\text{max}} \approx 500$ nm), matching those previously observed for complex **2-H₂O** and complex **2**, respectively. The small shift of peaks to earlier R_t was attributed to the use of MeOH as a solvent in place of water (the solvent used for previous reaction monitoring).

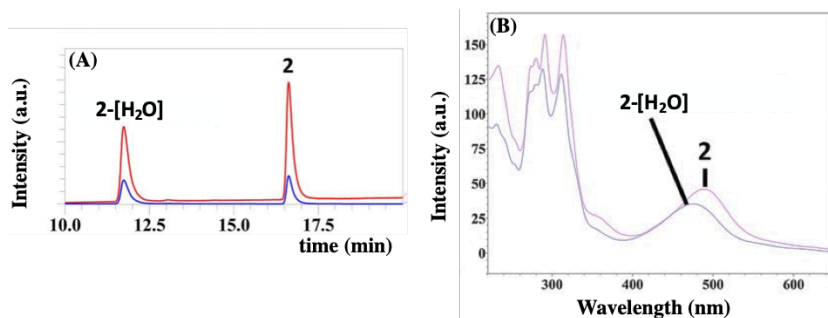


Figure (1.27). RP-HPLC of solution mixture from **2** and the aqua-coordinating Ru^{II}-complex (**2-H₂O**) pre-prepared in methanol solvent (A) (PDA wavelengths; 220 nm “Red,” and 500 nm “Blue”). On-line UV-vis spectra of the observed chromatographic peaks (B).

1.3.1.2. Product purification and characterization

After testing different purification procedures (size-exclusion chromatography, SEC, **see supporting information (S1)**), RP-LC was found to be the most reliable, time-effective and cost-effective technique for the purification of the products from the reaction crude. When complex **2** was used for spectroscopic analyses, the SEC was adopted to prevent water exchange of the labile chloride ligand during purification, **see supporting information (S2)**.

The analytical HPLC profile of the purified **2**, **Figure (1.28, A)**, reveals an intense peak at 17.0 min and few peaks at earlier retention times. The latter have been attributed to the solvent exchange of the Cl^- ligand (water and TFA exchanging ligands). In contrast, the SEC purified complex lacked of such impurities. For complex **2**, we reached 87% purity by RP-LC purification, whereas it exceeded 99% by SEC.

The high-resolution mass spectrum of **2** presents the expected isotopic distribution for ruthenium at m/z values centered around most abundant isotope at 526.038, **Figure (1.28, B)**, which corresponds to the expected theoretical mass of the $[\text{M}^+]$ ion (experimental 526.038 Da, theoretical 526.037 Da).

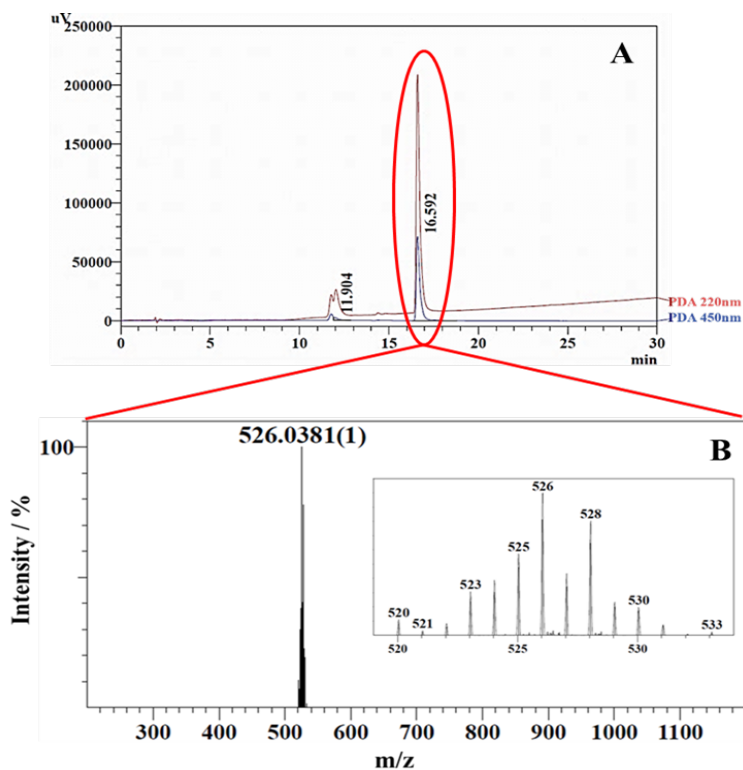


Figure (1.28). RP-HPLC of the RP-LC purified sample **2** (A). IT/TOF-MS spectrum of complex **2**. Insert shows the characteristic ruthenium isotopic pattern (B).

The HPLC profile of the RP-LC purified complex **3**, **Figure (1.29, A)**, shows a well-resolved peak at 12.1 min. High purity was obtained, exceeding the 99.9%, as calculated from area integration of the eluted peaks.

The high-resolution mass spectrum of **3**, **Figure (1.29, B)**, presents the expected isotopic distribution for ruthenium at m/z values centered around most abundant isotope at 307.053 (M^{2+}), (exp. 614.105 Da, theor. 614.100 Da). Ions at 245.535 and 266.050 have been assigned to in-source fragmentation products resulting from either loss of pyCOOH ($[Ru^{II}(bpy)(tpy)]^{2+}$) or acetonitrile replacement ($[Ru^{II}(bpy)(tpy)(ACN)]^{2+}$), respectively.

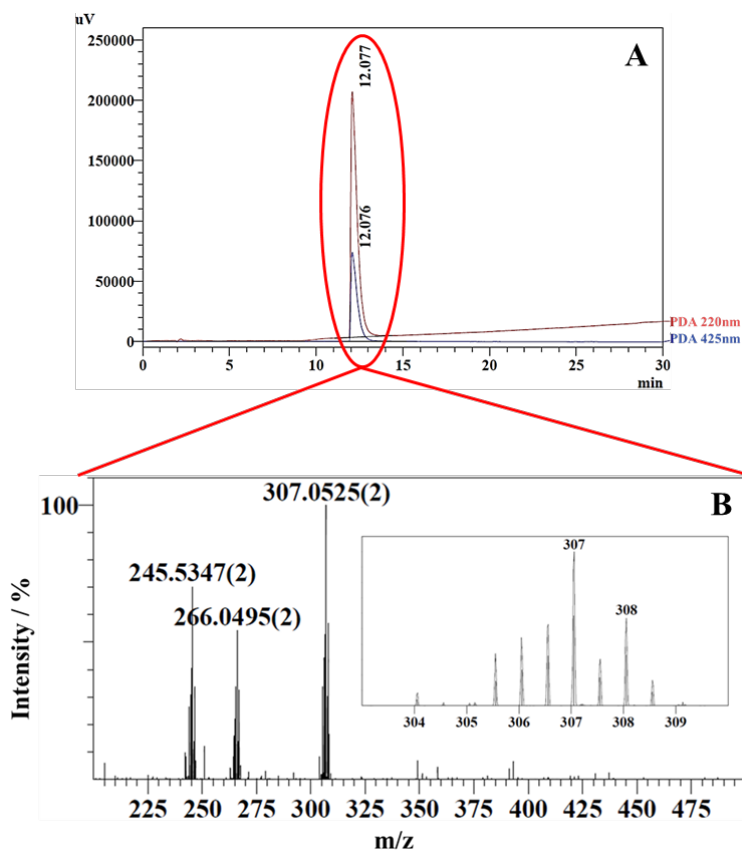


Figure (1.29). RP-HPLC of the RP-LC purified sample **3** (A). IT/TOF-MS spectrum of complex **3**. Insert shows the characteristic ruthenium isotopic pattern (B).

1.3.2. NMR-based structural characterization

1.3.2.1. NMR characterization of the complex **2**

The analysis was carried out in CD₃CN. The ¹H-NMR of the complex (**2**) is reported in **Figure (1.30)**.

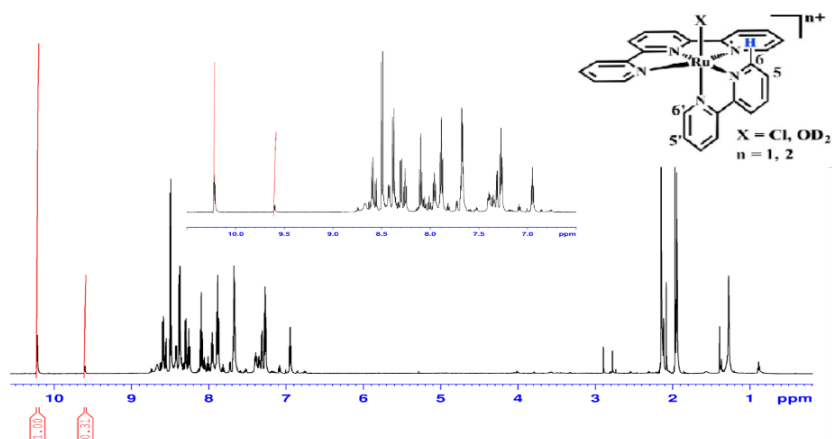


Figure (1.30). The assigned ¹H-NMR spectrum of **2** (10mM) in CD₃CN.

The spectrum shows, as expected, a set of signals located in the low field region ($\delta = 6.8 - 11$ ppm) where resonate the aromatic protons. In this region two peaks are largely downfield shifted ($\delta = 9.6$ and 10.2 ppm), which, as reported in literature¹¹⁸, can be attributed to the H₆ resonance of the tpy-rings in the equatorial position. This proton is strongly influenced by shielding effect of axial hetero-ligands, H₂O and Cl⁻ ligands, respectively.

A careful inspection of the ¹H-NMR spectrum reveals the presence of two different complexes, in the ca. 77/23 ratio: the complex (**2**) and the **2-H₂O**, respectively.

1.3.2.2. NMR characterization of the Complex 3

The complex (**3**) was also analyzed and completely assigned by NMR. The proton resonances were assigned following the standard procedure ¹¹⁹, by using homonuclear TOCSY ¹²⁰, DQCOSY ¹²¹, and ROESY experiments ¹²², see **supporting information (S4 & S5)**. The chemical shifts are exported in the **Table 1.1**.

Table 1.1. Complex 3 assignment

Complex (3)	1H-NMR chemical shift values							
bpy	b2	b1	b3	b2'	b3'	b4	b4'	b1'
	7.06(t)	7.27(d)	7.79(t)	7.82(t)	8.28(t)	8.38(d)	8.64(d)	8.69(d)
tpy	t2, t2'	t1, t1'	t3, t3'	t2''	t4, t4'	t4'', t3''		
	7.39(t)	7.77(d)	8.01(t)	8.17(t)	8.41(d)	8.51(d)		
py	p2, p6	p3, p5						
	7.54(d)	7.61(d)						

The ¹H-NMR spectrum of the complex (**3**) is characterized by sharp and well-resolved resonances, **Figure (1.31)**.

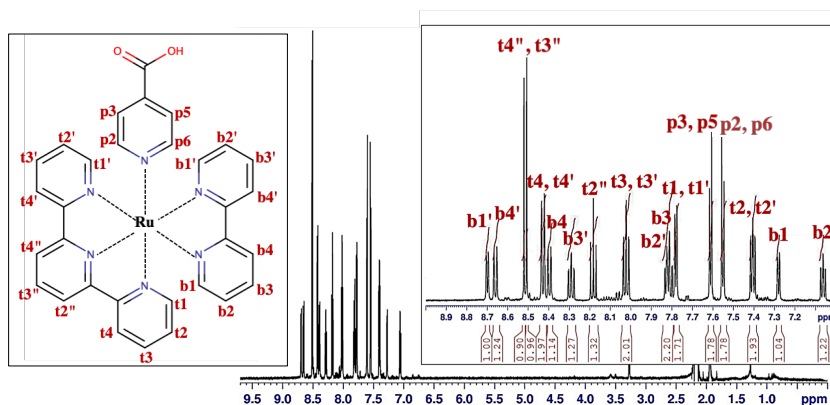


Figure (1.31). The assigned ¹H-NMR spectrum of the **3** (10mM) in CD₃CN (**right**). The assignment protons in the Ru^{II}-complex structure (**Left**).

The spectrum of **3** in CD₃CN, **Figure (1.31)**, is consistent with the symmetry of the complex and shows 16 resonances in the spectral region between 7.0 to 9.0 ppm: six resonances were assigned to the ring-protons of bpy-ligand, eight resonances were assigned to the ring-protons of tpy-ligand, and two resonances were assigned to the ring-protons of the pyCOOH ligand.

The bpy-ligand shows eight resonances (ring 1 and ring 2) that are due to the two non-equivalent pyridine “halves”, as a consequence of different positioning of the two rings: axial and equatorial.

It is worth noting that each peak of the axial bpy-ring is remarkably upfield shifted compared to that of the corresponding proton on the other ring in equatorial position (e.g. $\delta H_{b1} = 7.27$ vs. $\delta H_{b1'} = 8.69$) due to the shielding effect of tpy-equatorial ligand, **Figure (1.32)**.

The analysis of the tpy-rings resonances revealed that the protons, $H_{t1,t1'}$ and $H_{t2,t2'}$, are upfield shifted (7.77, 7.39 ppm) compared to that of the other tpy-protons. It is reasonable assume that this shift is due to the shielding cone of the neighbor bpy-ligand, **Figure (1.32)**.

The two resonances at $\delta = 7.61$ (d) and 7.54 (d) are attributed to the four protons, $H_{p3,p5}$ and $H_{p2,p4}$, of the pyCOOH ligand; the $H_{33,p5}$ proton resonance is downfield shifted compared to the resonance of $H_{2,6}$ due to the deshielding effect of the carboxyl group.

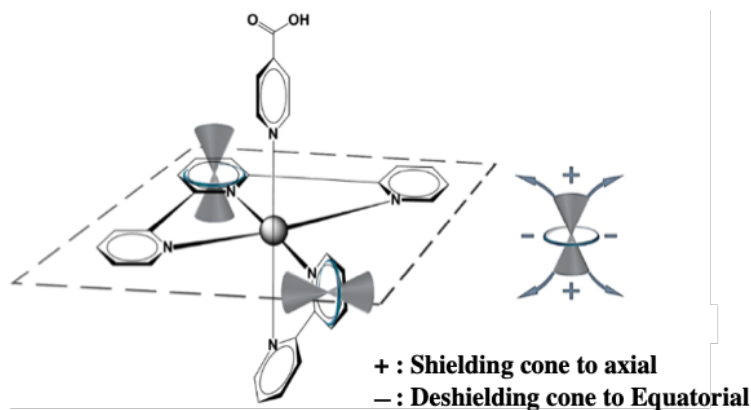


Figure (1.32). Schematic repetitive image for the axial-equatorial cone-effect of the aromatic rings (e.g., pyridine-rings) on the chemical shift of the ^1H -NMR spectrum of **3**.

Based on the NMR analysis we can conclude that, as expected the ruthenium(II) centers display a pseudo-octahedral coordination in these complexes, with three nitrogen donors from each of the tpy-rings occupying the equatorial plane, two nitrogen donors from each of the bpy-ligand are located in axial and equatorial positions, and the pyCOOH ligand, completing the first coordination sphere in axial position, **Figure (1.33)**.

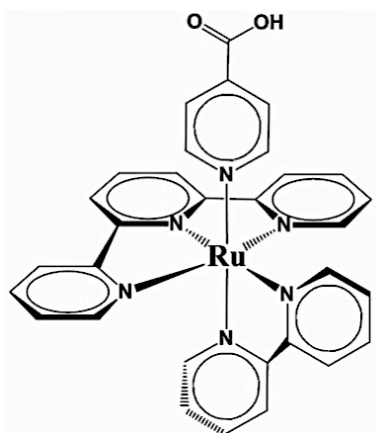


Figure (1.33). NMR-based structure for the ruthenium(II) complex (**3**).

1.3.3. Photophysical characterization of the complex **3**

The photophysical properties of the complex **3** were investigated by conducting steady-state spectroscopic (UV-Vis absorption and fluorescence) experiments. The $[\text{Ru}^{\text{II}}(\text{bpy})_3]$ complex, see **supporting information for synthetic details (S7 & S8)**, was used as a standard^{123,124}. Complex **2**, previously characterized by other authors¹²⁵, was also investigated for further comparison.

The absorption spectra of the ruthenium complexes **2**, **3**, and $[\text{Ru}^{\text{II}}(\text{bpy})_3]$, **Figure (1.34)** present three leading bands, corresponding to the following electron-transitions: (i) the allowed ($\pi \rightarrow \pi^*$) transition of the pyridine-ligand center (LC), which appears as intense and sharp bands in the far-UV region ($\lambda = 200\text{-}350$ nm); (ii) the forbidden ($d \rightarrow d$) transition of the metal center (MC), which appears as a shoulder located in the near-UV region ($\lambda = 350\text{-}400$ nm); (iii) the MLCT band, indicating the transition to the ¹MLCT state, which appears as a broad band in the visible region ($\lambda = 400\text{-}700$ nm).

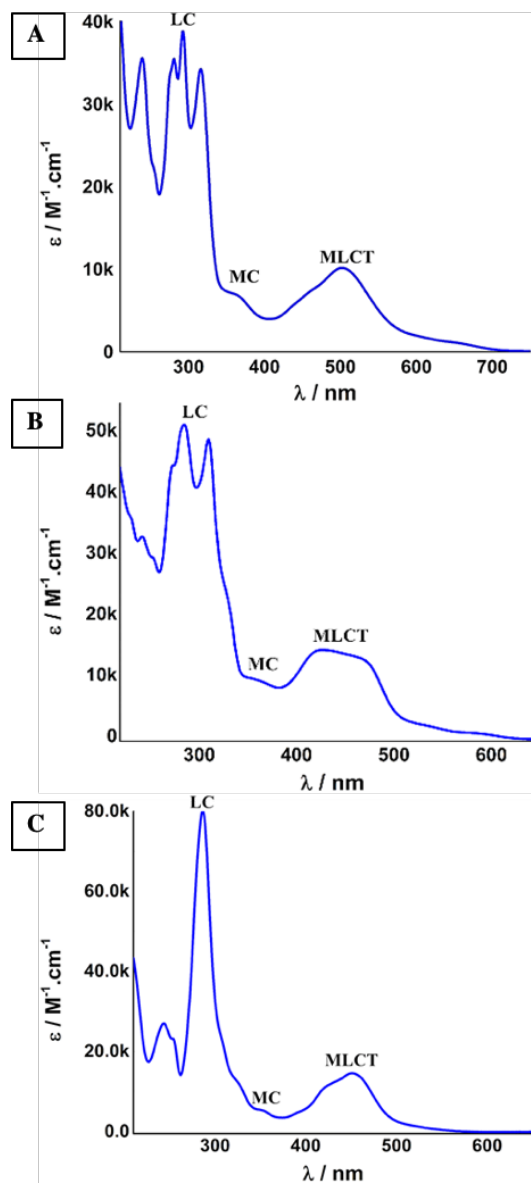


Figure (1.34). UV-Vis spectra of the complexes **2** (A), **3** (B), and $[\text{Ru}^{\text{II}}(\text{bpy})_3]$ (C), using ACN as the solvent.

In the context of photosensitization, the extent of visible light harvesting is one of the more crucial features for such complexes. This can be estimated by evaluating the molar absorptivity at the maximum wavelength ¹²⁶. Molar absorptivity of

¹MLCT electronic transition for the ruthenium complexes **2**, **3**, and [Ru^{II}(bpy)₃] were determined by following the absorption at different concentrations, and evaluating the slope of the linear regression, according to the Beer-Lambert's law, **see supporting information (S9)**, and it was found that the ϵ values for **2** is ca. 10,000 M⁻¹cm⁻¹ (at λ_{max} = 502 nm), for **3** is 12,000 M⁻¹cm⁻¹ (at λ_{max} = 460 nm) and ca. 13,000 M⁻¹cm⁻¹ (at λ_{max} = 427nm), and for the [Ru^{II}(bpy)₃] is 14,600 M⁻¹cm⁻¹ (at λ_{max} = 451nm).

Superimposition of the absorption spectra in the MLCT region, **Figure (1.35)** shows that **3** closely matches [Ru^{II}(bpy)₃] features, whilst **2** shows a bathochromic shift towards 450 nm. The obtained molar absorptivity demonstrate that **3** has enhanced light-harvesting efficiency than its previously reported analogues^{85,127}, and only slightly lower than standard [Ru^{II}(bpy)₃]. Moreover, **3** absorbs light in a broader range of the visible spectrum compared to the [Ru^{II}(bpy)₃] complex, suggesting that **3** could be more easily excited to the singlet state by white-light¹²⁸.

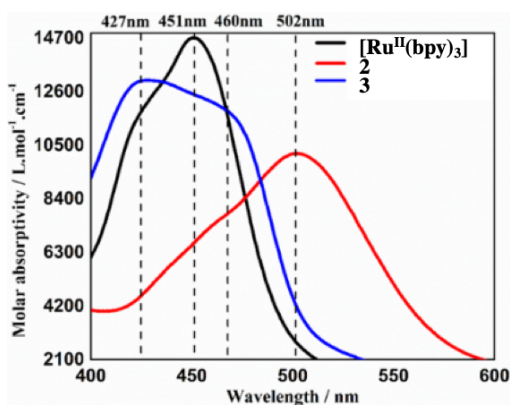


Figure (1.35). Superimposed Absorption spectra of complexes **2** (red), **3** (blue) and [Ru^{II}(bpy)₃] (black) in the MLCT region.

Emission spectra were collected by irradiating nitrogen-purged acetonitrile solutions of **2**, **3**, and $[\text{Ru}^{\text{II}}(\text{bpy})_3]$ at their own MLCT maximum wavelengths, **Figure (1.36)**. As expected for this class of compounds ⁸⁵, an emission band was observed at $\lambda_{\text{max}} = 720 \text{ nm}$ ($\lambda_{\text{ex}} = 502 \text{ nm}$), 607 nm ($\lambda_{\text{ex}} = 460 \text{ nm}$) and 604 nm ($\lambda_{\text{ex}} = 451 \text{ nm}$), for complexes **2**, **3**, and $[\text{Ru}^{\text{II}}(\text{bpy})_3]$ respectively.

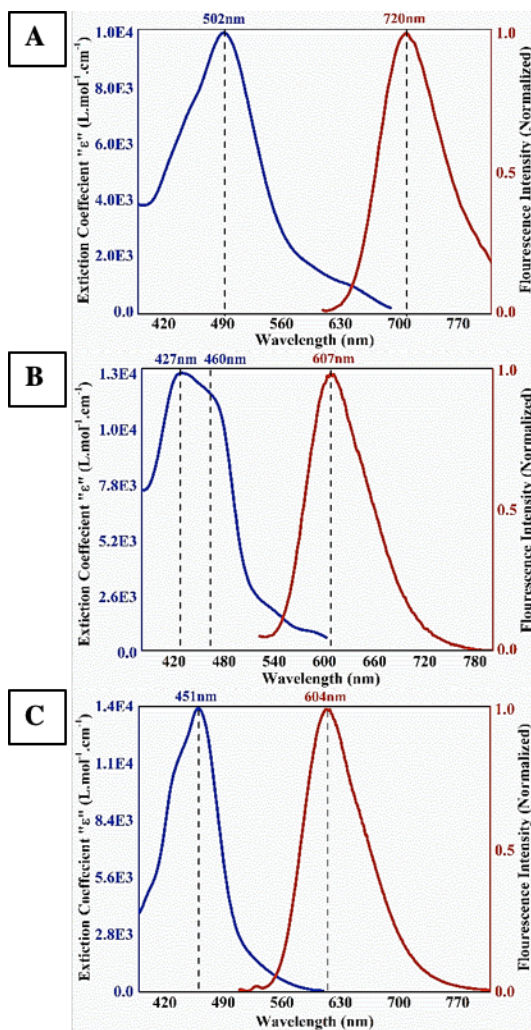


Figure (1.36). Absorption (blue) emission (red) spectra of the **2** (A), **3** (B) and $[\text{Ru}^{\text{II}}(\text{bpy})_3]$ (C) in the MLCT region.

Superimposition of the emission spectra, **Figure (1.37)**, corresponding to the $^3\text{MLCT}$ radiative decay, show that complexes **3** and $[\text{Ru}^{\text{II}}(\text{bpy})_3]$ phosphoresce approximately in the same energy range, whereas **2** is significantly red-shifted.

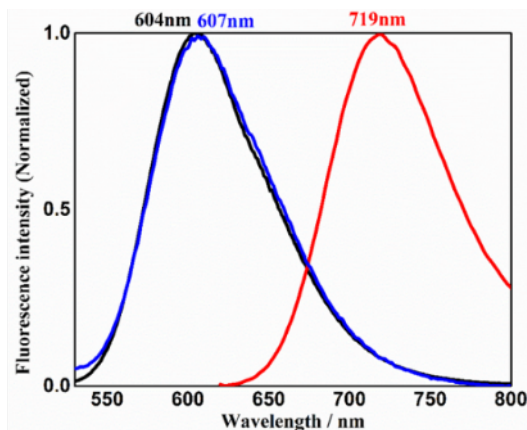


Figure (1.37). Superimposed emission spectra of complexes **2** (red), **3** (blue) and $[\text{Ru}^{\text{II}}(\text{bpy})_3]$ (black). Excitation wavelengths are reported on top of each spectrum.

The fluorescence quantum yield of **3** was measured by a previously reported comparative method ⁵³, using the $[\text{Ru}^{\text{II}}(\text{bpy})_3]$ (quantum yield (Φ) = 0.095) as standard ¹²³. Integration of the fluorescence spectrum was plotted against the absorption intensity at increasing complex concentrations, **see supporting information (S10)**. The slopes obtained by the linear regression of the graph give the desired parameter, according to **equation (1.6)**.

$$\Phi_S = \Phi_R \left(\frac{G_S}{G_R} \right) \left(\frac{n_S^2}{n_R^2} \right) \quad (1.6)$$

Where Φ_S and Φ_R represent the quantum yield of the sample and the reference, respectively; G_S and G_R represent the gradient of the sample and the reference, respectively; and n is the refractive index of the solvent, which its quotient goes to unity if same solvent is used for the sample and the reference.

As expected for this class of terpyridine-based Ru(II) complexes, **3** has only limited fluorescence quantum yield, approximately tenfold less than $[\text{Ru}^{\text{II}}(\text{bpy})_3]$ ($\Phi(\mathbf{3})=0.009$; $\Phi([\text{Ru}^{\text{II}}(\text{bpy})_3])=0.095$)¹²³. Despite the obtained fluorescence quantum yield, any strong correlation can be devised between the extent of radiative decay and photo-induced charge-transfer capability (or as photosensitizer efficiency).

As previously reported by many authors, the reduction potential of the excited state ($[\text{Ru}]^{3+}/[\text{Ru}]^{2+*}$) may be estimated from the spectroscopic data^{69,129,130}. To accomplish this task, energy difference of the Ru^{2+} singlet to triplet transition energy must be subtracted from the $[\text{Ru}]^{3+}/[\text{Ru}]^{2+}$ reduction potential in the ground state, **Figure (1.38)**.

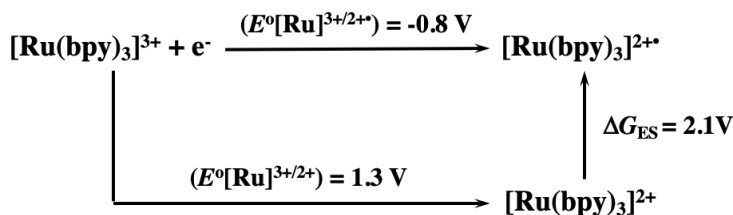


Figure (1.38). Thermodynamic cycle for calculating the excited state reduction potential of $[\text{Ru}^{\text{II}}(\text{bpy})_3]$ ¹³¹.

Energy difference between triplet and ground state in their thermal equilibrium levels essentially corresponds to the E_{0-0} value, which can be estimated by averaging the intersection point of the lowest energy absorbance and emission features and the emission maximum wavenumbers. These values for complex **3** correspond to $18,200 \text{ cm}^{-1}$ and $16,500 \text{ cm}^{-1}$, respectively, the average being $17,350 \text{ cm}^{-1}$ (2.15 eV). The latter value is in good agreement with the 0-0 energy reported for a close analogue of **3**, lacking the carboxyl moiety ($17,100 \text{ cm}^{-1}$)¹²⁷. According to our spectral data, the same value could be obtained in the case of $[\text{Ru}^{\text{II}}(\text{bpy})_3]$ within the experimental error, which corresponds to the E_{0-0} value reported in the

literature ^{129,131}. ($[\text{Ru}]^{3+}/[\text{Ru}]^{2+}$) couple reduction potentials in the ground state can be taken from published results for $[\text{Ru}^{\text{II}}(\text{bpy})_3]$ and for a very close analogue of **3** (1.26 V and 1.46 V, respectively) ^{85,129,131}.

According to these values, we may estimate the $E^0([\text{Ru}]^{3+}/[\text{Ru}]^{2+*})$ for both complexes, being -0.66 V for complex **3** and -0.86 V for $[\text{Ru}^{\text{II}}(\text{bpy})_3]$. The latter value is in perfect agreement with the literature, thus supporting the here presented estimation also for complex **3**.

1.3.4. Theoretical calculations

Understanding the electronic properties of the ruthenium(II)-complexes is significant for the elucidation of the related photophysical and photochemical properties, and the structure-to-function relationships ¹³². Therefore, the theoretical calculations based on the density functional theory (DFT) and time-dependent DFT (TD-DFT) methods were performed. In order to aid in the understanding of the electronic properties of the synthesized complex (**3**), a comparative study was also performed for both **2** and $[\text{Ru}^{\text{II}}(\text{bpy})_3]$. The details about the computational methods and the level of theory are provided in the experimental section, **section (1.5.2; p. 69)**.

First, the structural optimization of the complexes was performed in ACN solvent via DFT calculations, while the TD-DFT calculations were used for studying the electronic transition and compared to the experimental results.

1.3.4.1. Structural optimization

The DFT-based optimized structural calculations, **Figure (1.39)** were accepted after the calculated frequencies values went to positive values, and the guessed stationary points matched the energetic minimum points.

The optimized structure of the synthesized complex **3**, **Figure (1.39)** was found in good agreement with structural NMR analysis, in **section (1.3.2.2; p. 46)**. Moreover, structural parameters for **2** and $[\text{Ru}^{\text{II}}(\text{bpy})_3]$ were compared with literature values and satisfying agreement was achieved with the adopted level of theory^{69,125}.

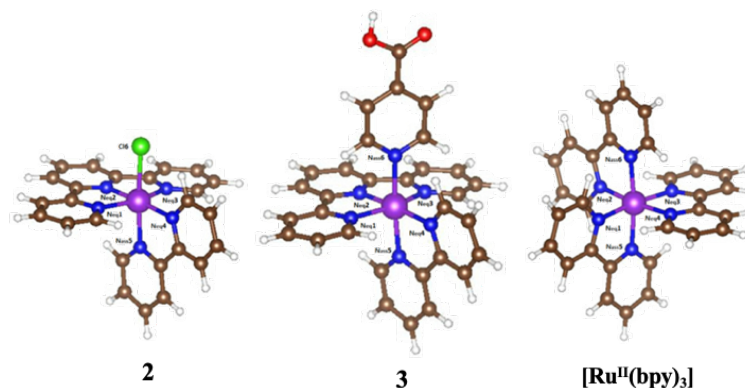


Figure (1.39). Optimized structures of the Ru^{II} -complexes (**2**, **3**, and $[\text{Ru}^{\text{II}}(\text{bpy})_3]$). Atoms are colored as Ru (Purple), C (Brown), H (White), N (Blue), O (Red), and Cl (Green).

1.3.4.2. Binding energy calculation

The stability of the complexes could be inferred by evaluating the binding energy values, which are given by the following equation, **equation (1.7)**:

$$\Delta E = E_{\text{Complex}} - (E_{\text{Metal}} + E_{\text{ligand}}) \quad (1.7)$$

The calculated binding energy was defined from the optimized calculations of the complex structure, free-ligands structures, and metal ion in ACN as the solvent, at the same level of theory.

SCF (energy deduced from DFT structure optimization) and ZPE (zero-point energy derived from harmonic oscillator approximation) calculations were summed to account for the energies of both the complex and the associated free-

ligands. Whereas, the energy of the metal center was defined based on the ZPE-derived energy value. The following equation summarizes the adopted approach:

$$\Delta E = (SCF + ZPE)_{Complex} - \left[ZPE_{Metal} + \sum_i \{(SCF + ZPE)_{ligand}\}_i \right]$$

The calculated binding energies (ΔE_{Calc}) are reported in the **Table 1.2**. As expected, $[Ru^{II}(bpy)_3]$ was found to be the most stable complex owing to the most negative binding energy, energy differences with respect to **3** and **2** being within 8 and 15 kcal.mol⁻¹, respectively.

Table 1.2. Calculated binding energy value of the Ru^{II}-complexes (**2**, **3**, and $[Ru^{II}(bpy)_3]$).

METAL COMPLEX	ΔE (kcal/mol)
2	-237.13
3	-243.85
$[Ru^{II}(bpy)_3]$	-252.13

The higher stability of the $[Ru^{II}(bpy)_3]$ complex can be attributed to the chelating effect of the bpy-ligands. The lower stability of complex **2** can be accounted for by the presence of the labile Cl⁻ ligand, which shows less affinity for coordination with the Ru^{II}. This less-stability of the **2** is in agreement with what been observed in the synthetic part of the **section (1.3.1.1; p. 37)**. The here synthesized complex **3** has shown considerably high stability, but less than the $[Ru^{II}(bpy)_3]$ complex, which can be mostly charged to the anchoring of a monodentate ligand (pyCOOH). Nevertheless, the significantly higher stability of **3** compared to **2** is in agreement with its stability under HPLC acidic conditions, where no water exchange was observed, as compared with fast ligand exchange observed for complex **2**.

1.3.4.3. Electronic transition calculation

The electronic transitions of the ruthenium(II)-complexes were determined by performing TD-DFT calculations. The electronic transition intensity is related to oscillator strength (f_{osc}), as defined in the following equation, **equation (1.8)**:

$$f_{osc} = \int \epsilon(\bar{\nu}) d\bar{\nu} = \frac{4\pi^2 N_A \bar{\nu}}{3 \times 10^4 c n^2 \hbar l} |\bar{M}|^2 \quad (1.8)$$

Where f_{osc} represents the oscillator strength; $\epsilon(\bar{\nu})$, the molar absorptivity; N_A , the Avogadro's number; n , the refractive index of the solvent, \hbar , the Planks constant, l , the path-length; and \bar{M} , the transition moment vector.

Therefore, the electronic transitions could be determined upon calculating the energies of the active vertical transitions and their transition moment. Subsequently, the energy of the first excited state was defined.

The energies of the first ten excited states of each Ru^{II}-complex were calculated, and the active electronic transitions for each metal complex were determined according to the electronic transitions with non-zero f_{osc} (active electronic transition; $f_{osc} \neq 0$). Therefore, the energy of the electronic transition between excited and ground states, and the linked wavelength were derived.

Table 1.3 reports the results of the TD-DFT of the ruthenium(II)-complexes in the MLCT region. It shows that the estimated wavelength of the electronic transitions was 584.20, 477.27 and 447.30 nm, respectively. These calculated wavelengths are in very good agreement with the obtained experimental values were shown in **section (1.3.3)**. Such correspondence between the theoretical and experimental wavelengths assures the reliability of the conducted calculations.

Table 1.3. Electronic transitions and molecular orbital analysis of the complexes; **2**, **3**, and [Ru^{II}(bpy)₃].

METAL COMPLEX	λ (nm)	Electronic Transition	f_{osc}
2	584.20	HOMO \rightarrow LUMO	0.0164
3	477.27	HOMO \rightarrow LUMO	0.0113
[Ru ^{II} (bpy) ₃]	447.30	HOMO ₋₁ \rightarrow LUMO	0.0172

The AVERA program was used to visualize and analyze the molecular-orbitals (MO) corresponding to the calculated ground (HOMO) and excited (LUMO) states. **Figure (1.40)** shows the isodensity plots ($\sigma = 0.04$) HOMO and LUMO of the three Ru(II)-complexes. The following features could be observed:

- (i) The three-studied complexes possess the expected MLCT “ $d\pi(M) \rightarrow \pi^*(L)$ ” electronic transition. In which, the observed transitions are occurring between the HOMO with high contribution of the metal electronic, together with the LUMO having more ligand (p orbitals of C and N) electronic contribution.
- (ii) In [Ru^{II}(bpy)₃] complex, the LUMO has homogeneous electronic density distribution on the bpy ligands. While, **2** and **3** show non-homogeneous electronic density distribution, with more contribution from the tpy-ligand.
- (iii) In complex **2**, (ground state) significant electronic density was localized on the Cl⁻ ligand, with anti-bonding character to the $d\pi$ -orbital of the metal. The high contribution from the Cl⁻ ligand helps in explaining the bathochromic shift observed in this complex absorption of spectrum. In contrast, the HOMO of **3** and [Ru^{II}(bpy)₃] complexes show similar electronic density distribution, owing to the predominant contribution from the $d\pi$ of the metal-center. Also, the similarity of the HOMO characteristics

shown for complex **3** and $[\text{Ru}^{\text{II}}(\text{bpy})_3]$ is actively explaining the close absorption features that were previously reported in **section (1.3.3; p. 49)**.

- (iv) In complex **3**, the electronic density of LUMO (the excited state) shows a high contribution from carboxyl moiety. This may represent extremely positive on its electron-transfer features. This result is even more crucial if we consider that the conjugation between **3** and other molecular assemblies will be performed through this moiety.

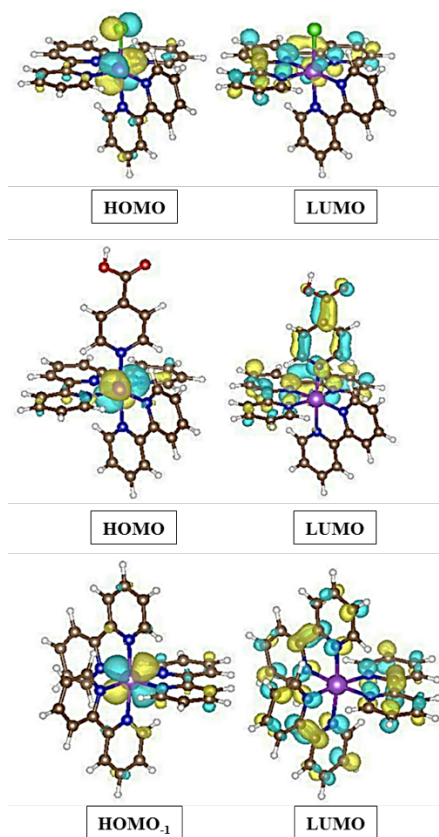
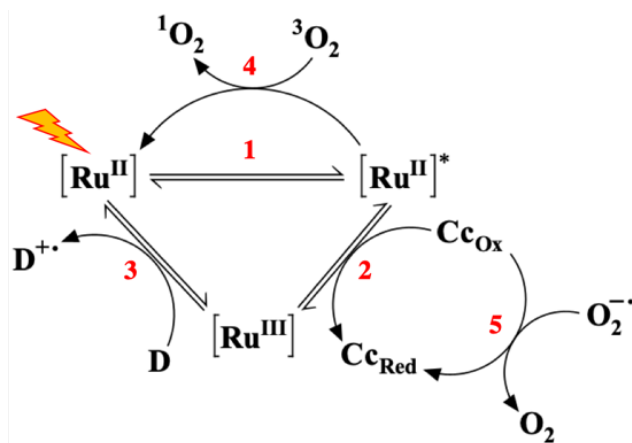


Figure (1.40). Isodensity plots of HOMO and LUMO orbitals for the Ru^{II} -complexes; **2** (Top), **3** (Middle), and $[\text{Ru}^{\text{II}}(\text{bpy})_3]$ (Bottom). [Color code: surfaces of the bonding MO orbitals (light blue), surfaces of the anti-bonding MO orbitals (yellow)]; All orbitals have been computed at an isovalue of 0.04.

1.3.5. Photochemical characterization of the complex **3**

Photo-induced electron transfer (PET) to Cytochrome c (Cc) has been performed to test the photochemical performance of **3**, and the obtained results have been compared to complex [Ru^{II}(bpy)₃]. Cc is particularly convenient for such experiments, owing characteristic *Soret* and *Q* bands, which are sensitive to the iron oxidation state. The Soret band of the oxidized form (Cc_{ox}) is located at 409 nm, redshifting to 414 nm upon reduction. Moreover, Q band located at 550 nm, is much more intense for Cc_{red} than Cc_{ox} ($\epsilon(550; \text{Cc}_{\text{red}}) - \epsilon(550; \text{Cc}_{\text{ox}}) = 18.3 \text{ mM}^{-1} \text{ cm}^{-1}$)¹³³.

A kinetic investigation on a multi-component system has been performed, using aniline (5.4 mM), **3** (27.9 μM) and Cc (5.5 μM) as sacrificial electron donor, photo-induced reductant and terminal electron acceptor, respectively, **Scheme (1.2)**. The reaction was carried out under inert atmosphere to avoid any undesired O₂-dependent side reaction: (i) ³MLCT quenching, **step 4 in Scheme (1.2)**, and consequential formation of singlet dioxygen (¹O₂) and reactive oxygen species (ROS)^{64,134}; (ii) off-pathway Cc_{ox} reduction by superoxo radical anion, **step 5 in scheme (1.2)**^{133,135}.



- 1: Ruthenium(II) complex absorbs a photon and the excited state is formed ($[\text{Ru}^{\text{II}}]^*$).
- 2: Oxidative photoreduction of CcOx by $[\text{Ru}^{\text{II}}]^*$.
- 3: $[\text{Ru}^{\text{III}}]$ reduction by sacrificial electron donor (D).
- 4: O_2 -dependent quenching the $[\text{Ru}^{\text{II}}]^*$ and singlet dioxygen formation.
- 5: superoxo-dependent reduction of CcOx .

Scheme (1.2)

Upon blue LED light irradiation, **Figure (1.41, A)**, slow but appreciable changes in the UV-Vis spectrum were observed, **Figure (1.41, B)**.

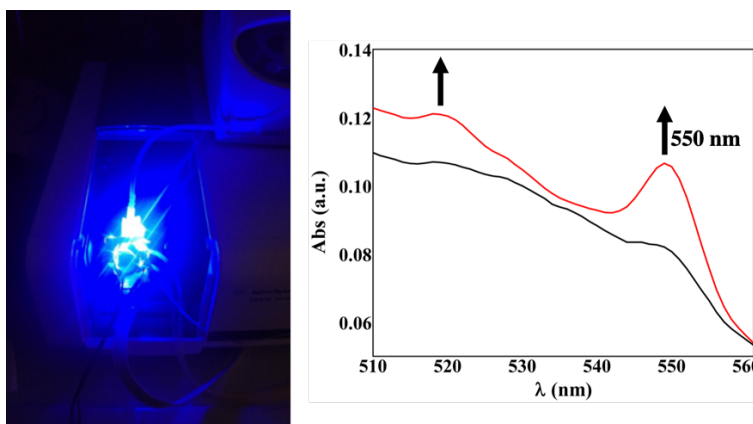


Figure (1.41). Photographic shot of the adopted irradiation setup; A blue LED ribbon coiled around the reaction-cell. The reaction progress was monitored by UV-Vis spectroscopy from 200-800nm with a scan-rate of 800 nm/min. Under constant stirring and 25°C temperature by a Peltier control unit.

Difference absorption spectra (ΔA) show the distinctive footprint of Cc-red formation over time, **Figure (1.42)**. Together with *Soret* and *Q* bands increase, ruthenium complexes depletion could be appreciated by the quenching of the MLCT band at 447 nm. These changes confirm the PET process for both complexes (**3** and $[\text{Ru}^{\text{II}}(\text{bpy})_3]$).

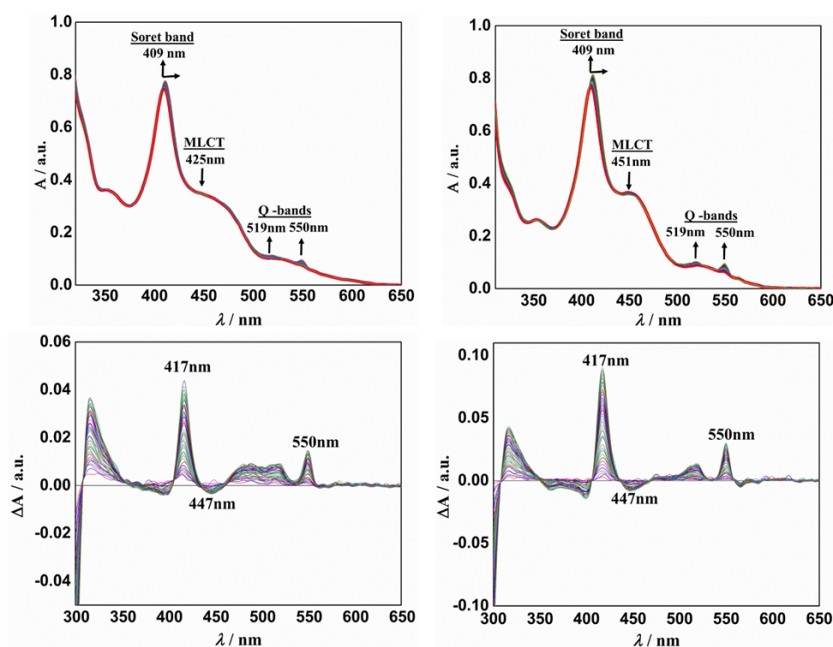


Figure (1.42). Absorption spectra (**Top**) and difference absorption spectra (**Bottom**) over time for the photoinduced reduction of Cc ($5.5\mu\text{M}$), in the presence of 5eq of **3** (**Left**), or $[\text{Ru}^{\text{II}}(\text{bpy})_3]$ (**Right**) and aniline (5.5 mM) in phosphate buffer (0.1 M ; $\text{pH } 6.89$), 25°C . Red-line indicates the starting (dark) spectrum, arrows indicate the band directions over time.

Further kinetic studies were performed to investigate the mechanism of the PET-activity for **3** and $[\text{Ru}^{\text{II}}(\text{bpy})_3]$. Firstly, photo-reduction of Cc was performed at different photosensitizer concentrations, **see supporting Information (S11)** to probe its effect on the electron-transfer rate. The initial rate vs. Ru^{II} -concentrations

was plotted, **Figure (1.43)**, which has been found linear against concentrations of both complexes, meaning the reaction is first-order on the photosensitizer.

Apparent rate constants (k') have been evaluated from the linear fits as $2.9 \cdot 10^{-5} \text{ s}^{-1}$ and $3.8 \cdot 10^{-5} \text{ s}^{-1}$ for **3** and $[\text{Ru}^{\text{II}}(\text{bpy})_3]$, respectively, complex **3** being 76% as efficient as $[\text{Ru}^{\text{II}}(\text{bpy})_3]$.

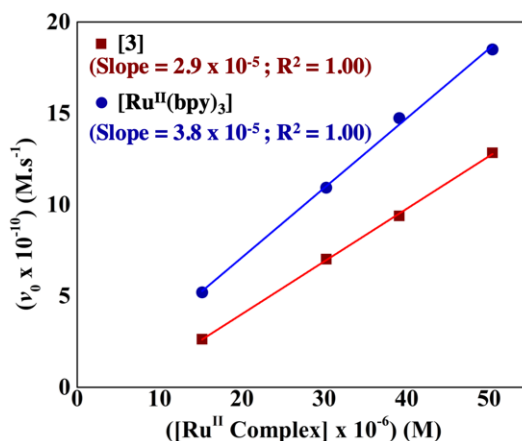


Figure (1.43). PET initial rate vs. concentration plot for both ruthenium(II)-complexes (**3** and $[\text{Ru}^{\text{II}}(\text{bpy})_3]$). Initial rates were extrapolated from a single exponential fit of the kinetic traces at $\lambda = 550 \text{ nm}$. The slope of the linear fit corresponds to the apparent rate-constant (k' reported as μs^{-1}), for a $v_0 = k'[\text{Ru}]_0$ rate law.

The activation energy (E_a) for each photosensitizer (**3** and $[\text{Ru}^{\text{II}}(\text{bpy})_3]$) was obtained by evaluating the apparent rate constant at different temperatures, see **supporting information (S12)**. Arrhenius-plot ($\ln k'$ vs. $1/T$), **Figure (1.44)** shows the activation energies of **3** and $[\text{Ru}^{\text{II}}(\text{bpy})_3]$ are 29.1 and $25.4 \text{ kJ}\cdot\text{mol}^{-1}$, respectively. Activation energy is slightly higher for **3** when compared with $[\text{Ru}^{\text{II}}(\text{bpy})_3]$, E_a difference being ca. $3.7 \text{ kJ}\cdot\text{mol}^{-1}$, most probably due to the higher reorganization energy during PET for terpyridine ligands, as already described by the literature ⁷⁸.

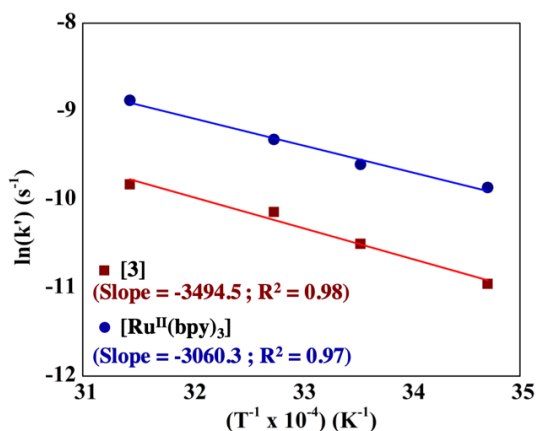


Figure (1.44). Arrhenius ($\ln k'$ vs. $1/T$) plot for both Ru^{II}-complexes (**3** and [Ru^{II}(bpy)₃]). The slope of the linear fits gives the activation energy E_a upon applying the equation: $\ln k' = \ln A - (E_a/R) (1/T)$. Cc (5.5 μM), in the presence of 35.5 μM of either **3** (red), or [Ru^{II}(bpy)₃] (blue) and aniline (5.5 mM) in phosphate buffer (0.1 M; pH 6.89)

Our results are not immediately comparable to previously reported kinetic constants for electron-transfer (k_{PET}), which are generally evaluated by transient absorption techniques, mostly because radiative decay and/or energy transfer processes could not be discarded under our steady-state conditions. Nonetheless, the evaluated first-order k' value falls in the range of reported k_{PET} ($10^5 - 10^6 \text{ s}^{-1}$), evaluated with both diffusing [Ru^{II}(bpy)₃] + MP8 systems and with Ru^{II}-complex -Cc covalent analogues^{103,129}. Slightly lower kinetic constant for complex **3** correlate with the previously extrapolated lower redox potential of the excited state, suggesting that the thermodynamic driving force is also participating in the observed lower kinetics.

1.4. Concluding Remarks

The synthesis and characterization of a new tris-heteroleptic polypyridine ruthenium(II)-complex of the form $[\text{Ru}^{\text{II}}(\text{bpy})(\text{tpy})(\text{L})]$, where L is pyridine-4-carboxylic acid ligand, were performed. Photophysical and photochemical analyses, supported by DFT calculation, were performed to assess the proficiency of **3** in performing PET processes with bio-molecular systems (cytochrome *c*).

Absorption/fluorescence steady-state experiments showed that **3** has enhanced molar absorptivity than its previously reported analogues, and only slightly lower than $[\text{Ru}^{\text{II}}(\text{bpy})_3]$. As expected for this class of terpyridine-based Ru^{II} -complexes, **3** has only limited fluorescence quantum yield, approximately tenfold less than $[\text{Ru}^{\text{II}}(\text{bpy})_3]$. From the obtained data, and by comparison with the literature, a reasonable value of the excited state redox potential could be estimated, being $E^0([\mathbf{3}]^{3+}/[\mathbf{3}]^{2+*}) = -0.66 \text{ V}$.

The TD-DFT calculations pointed out that the Py-COOH ligand is involved in the LUMO orbital of the MLCT transition, which can be beneficial in transferring electrons to molecules eventually conjugated to the acyl moiety.

Further, our results have shown that complex **3** is capable of PET to Cc. The PET process is first-order against Ru complex concentration, **3** being 76% as active as $\text{Ru}^{\text{II}}(\text{bpy})_3$. Such lower activity may be accounted for by the higher activation energy barrier (ca. $3.7 \text{ kJ}\cdot\text{mol}^{-1}$), which is connected either to the lower energetic driving force (1.12 eV for $[\text{Ru}^{\text{II}}(\text{bpy})_3]$; 0.92 eV for **3**; $E^0[\text{Fe}^{3+}\text{Cc}/\text{Fe}^{2+}\text{Cc}] = 0.26 \text{ V}$).

1.5. Materials and Methods

1.5.1. Materials, reagents, and solvents

Ruthenium chloride ($\text{RuCl}_3 \cdot x\text{H}_2\text{O}$), 2,2'-bipyridine (bpy), 2,2':6',2''-terpyridine (tpy) and Isonicotinic acid "4-pyridine carboxylic acid" (pyCOOH) were purchased from Sigma Aldrich and used as received. The solvents (absolute-ethanol, DMF) were HPLC-grade and purchased from Romil, the water used in synthesis was *milli-Q* water.

The solvents used for purification and chromatographic analysis were HPLC-grade (Romil), while the solvents that were used for spectroscopic (UV-Vis and Fluorescence) analysis were in a high degree of purity (UPS-grade) from Romil. The HCl solvent used for atomic absorption spectroscopy (AAS) was ultra-pure and traced of metal.

1.5.2. Instrumentations and techniques

HPLC analysis was performed with Shimadzu LC-10ADvp equipped with a diode-array detector, type SPD M10 Avp, and auto-injector. Reverse-phase C18 column was used, Model of Vydac 218TP (5μ) (length 150mm x ID 4.6mm). 0.1% TFA acidified solvents of (acetonitrile and water) were used. Running method including isocratic part of (10% acetonitrile) for 5min, a linear gradient of (10% - 50% acetonitrile) over 30min, and washing part of (95% acetonitrile) for further 5min with flow-rate of 1 mL/min.

The Purification of products was performed using flash chromatography from Biotage Isolera flash purification system, equipped with a diode-array detector. Biotage SNAP Ultra-C18 cartage (10 g; CV 15mL) was used in purification, the cartage were equilibrated using a recommended procedure by Biotage, LLC, and the running coarse with linear gradient of (10% - 95% 0.1% TFA acidified

acetonitrile/H₂O) for 20 CV in flow-rate 12 mL/min after dissolving the crude in concentrated solution in H₂O.

The mass-spectra were performed using LCMS-IT-TOF from SHIMADZU, with a direct injection of 0.2 μ L of the solution prepared in acetonitrile (100 μ M).

The atomic absorption spectroscopic (AAS) measurements were performed using a Shimadzu AA-7000 equipped with the flame atomizer. The solutions were prepared using 80% HCl traces of metals solvent.

The UV-Vis spectra were recorded using an Agilent technologies Cary 60 UV spectrophotometer, equipped with a thermostated cell and magnetic stirrer, in acetonitrile solvent, from 200-800 nm with a scan rate of 600 nm/min, 1 cm quartz-cuvette were used for the measurements.

The steady-state emission spectra were conducted using a Fluoromax-4 spectrophotometer from HORIBA Scientific Co., in acetonitrile solvent, S1/R1c corrected spectra were recorded, excitation as mentioned in the texts and emission of 500-800 nm, 5 mm slits with 1 nm increment, at 25 °C thermostat under stirring. The absorption/emission data were treated using the AE-software and Spectrograph-software after subtracting the solvents-spectrum, and data plots were treated using originLab program.

NMR-spectra was conducted using a 600 MHz Bruker instrument. The samples were prepared in deuterated acetonitrile (10 mM). ¹H-NMR, as well as to the 2D-experiments (TOCSY, COSY and ROESY), were recorded based on the experiments previously obtained by literature ¹²⁰⁻¹²².

Theoretical calculations were carried out using the DFT and TD-DFT calculation methods via the Gaussian-09 Package. Theory level of; Hybrid functional B3LYP for GS and excited states calculations, Basis set of 6-

31++G(d,p) for C, N and H atoms, pseudopotential SDD for Ru atom, The PCM model for acetonitrile solvent, and D3 Empirical Dispersion.

1.5.3. General procedure for preparation of the complex 3

The preparation of complex **3** was performed by typical successive ligation methods of such complexes mentioned by literature ¹³⁶, with a modified procedure.

1st step: the **1** (Dark greenish) was prepared by reacting 1eq RuCl₃.xH₂O (ca. 280 mg; 10 mM) with 1.1eq tpy (257.20 mg; 11mM) in ethanol (80mL) and refluxed at 80°C with continuous stirring under nitrogen. The dark greenish powders of **1** product were collected by centrifuge the reaction mixture and washed three times with ethanol and three times with diethyl ether. The dry product weight was 401.68 mg (Yield ca. 91%).

2nd step: The **2**·TFA (Dark red) was prepared by preparing solution of **1** (200.61 mg; 10.1mM) in 80% (EtOH: H₂O) solvent system (45mL) with 2eq bpy-ligand (171.80 mg; 220.0 mM) from the same solvent system (5mL), the reaction was started by adding the bpy-solution infractions to the one solution mixture at 50°C, then reflux at 85°C for 4h, under inert atmosphere. The resulting deep red solution was cooled to room temperature, and rotary evaporated, then the final solids were purified by re-dissolving in water and purified using (C18) reverse-phase flash chromatography, then lyophilized. The purified product weight was 236.91 mg (Yield ca. 93%, Purity = 77%) rest was [Ru^{II}(bpy)(tpy)(OH₂)]. For spectroscopic measurements, further purification was needed using size-exclusive chromatography using Sephadex LH20 resin and methanol eluted solvent, which lowers the yield but gets complex **2** with purity exceeds 99%.

3rd step: The **3**·TFA complex (Dark orange) was prepared by reacting 1eq of **2** (236.91 mg; 11.25mM) with 10eq isonicotinic acid (503.53 mg; 102.5mM) in

water (40 mL) and reflux at 85°C for 3h, The resulting dark orange solution was cooled to room temperature, and rotary evaporated, then the final solids were purified by re-dissolving in water and purified using reverse-phase flash chromatography, then lyophilized. The purified product weight was 462.60 mg (Yield ca. 85%, Purity = 99.9%).

References

1. Hoffert, M.I., Caldeira, K., Benford, G., Criswell, D.R., Green, C., Herzog, H., Jain, A.K., Kheshgi, H.S., Lackner, K.S., Lewis, J.S., et al. (2002). Advanced technology paths to global climate stability: energy for a greenhouse planet. **Science** **298**, 981–987.
2. Lewis, N.S., and Nocera, D.G. (2006). Powering the planet: Chemical challenges in solar energy utilization. **Proc. Natl. Acad. Sci.** **103**, 15729–15735.
3. Barber, J. (2008). Photosynthetic energy conversion: natural and artificial. **Chem. Soc. Rev.** **38**, 185–196.
4. Kalisky, Y. (2018). Spectroscopy and solar energy – in honor to Professor Renata Reisfeld. **J. Lumin.** **193**, 10–12.
5. Solar Panel Efficiency: What panels are most efficient? | Energysage (2020). Sol. News. <https://news.energysage.com/what-are-the-most-efficient-solar-panels-on-the-market/>. (Accessed 30/01/2020)
6. Dimroth, F., Tibbits, T.N.D., Niemeyer, M., Predan, F., Beutel, P., Karcher, C., Oliva, E., Siefer, G., Lackner, D., Fus-Kailuweit, P., et al. (2016). Four-junction wafer-bonded concentrator solar cells. **IEEE J. Photovolt.** **6**, 343–349.
7. Johansson, T.B., Kelly, H., Reddy, A.K.N., and Williams, R.H. (1993). Renewable fuels and electricity for a growing world economy: defining and achieving the potential. **Energy Stud. Rev.** **4**.

8. Tsoutsos, T., Gekas, V., and Marketaki, K. (2003). Technical and economical evaluation of solar thermal power generation. *Renew. Energy* **28**, 873–886.
9. Sundström, V. (2000). Light in elementary biological reactions. *Prog. Quantum Electron.* **24**, 187–238.
10. Barber, J., and Andersson, B. (1994). Revealing the blueprint of photosynthesis. *Nature* **370**, 31–34.
11. Sagadevan, A., and Greaney, M.F. (2019). *meta*-Selective C–H activation of arenes at room temperature using visible light: dual-function ruthenium catalysis. *Angew. Chem. Int. Ed.* **58**, 9826–9830.
12. Zhang, J., Jiang, C., Figueiró Longo, J.P., Azevedo, R.B., Zhang, H., and Muehlmann, L.A. (2018). An updated overview on the development of new photosensitizers for anticancer photodynamic therapy. *Acta Pharm. Sin. B* **8**, 137–146.
13. Qin, Y., and Peng, Q. (2012). Ruthenium sensitizers and their applications in dye-sensitized solar cells. *Int. J. Photoenergy* **2012**, 1–21.
14. Adeloye, A., and Ajibade, P. (2014). Towards the development of functionalized polypyridine ligands for Ru(II) complexes as photosensitizers in dye-sensitized solar cells (DSSC). *Molecules* **19**, 12421–12460.
15. Nazeeruddin, Md.K., Zakeeruddin, S.M., Humphry-Baker, R., Jirousek, M., Liska, P., Vlachopoulos, N., Shklover, V., Fischer, C.-H., and Grätzel, M. (1999). Acid–base equilibria of (2,2′-bipyridyl-4,4′-dicarboxylic acid) ruthenium(ii) complexes and the effect of protonation on charge-transfer sensitization of nanocrystalline titania. *Inorg. Chem.* **38**, 6298–6305.
16. Young, J.L., Steiner, M.A., Döscher, H., France, R.M., Turner, J.A., and Deutsch, T.G. (2017). Direct solar-to-hydrogen conversion via inverted metamorphic multi-junction semiconductor architectures. *Nat. Energy* **2**, 1–8.

17. Savage, D.F., Way, J., and Silver, P.A. (2008). Defossilizing fuel: How synthetic biology can transform biofuel production. **ACS Chem. Biol.** *3*, 13–16.
18. Andreiadis, E.S., Chavarot-Kerlidou, M., Fontecave, M., and Artero, V. (2011). Artificial photosynthesis: from molecular catalysts for light-driven water splitting to photoelectrochemical cells. **Photochem. Photobiol.** *87*, 946–964.
19. Varadhan, P., Fu, H.-C., Kao, Y.-C., Horng, R.-H., and He, J.-H. (2019). An efficient and stable photoelectrochemical system with 9% solar-to-hydrogen conversion efficiency via InGaP/GaAs double junction. **Nat. Commun.** *10*, 1–9.
20. Pan, L., Liu, Y., Yao, L., Dan Ren, Sivula, K., Grätzel, M., and Hagfeldt, A. (2020). Cu₂O photocathodes with band-tail states assisted hole transport for standalone solar water splitting. **Nat. Commun.** *11*, 318.
21. Nogueira, A.E., Oliveira, J.A., da Silva, G.T.S.T., and Ribeiro, C. (2019). Insights into the role of CuO in the CO₂ photoreduction process. **Sci. Rep.** *9*, 1316-1326.
22. Shoute, L.C.T., and Loppnow, G.R. (2003). Excited-state metal-to-ligand charge transfer dynamics of a ruthenium(II) dye in solution and adsorbed on TiO₂ nanoparticles from resonance raman spectroscopy. **J. Am. Chem. Soc.** *125*, 15636–15646.
23. Gagliardi, C.J., Westlake, B.C., Kent, C.A., Paul, J.J., Papanikolas, J.M., and Meyer, T.J. (2010). Integrating proton coupled electron transfer (PCET) and excited states. **Coord. Chem. Rev.** *254*, 2459–2471.
24. Abrahamse, H., and Hamblin, M.R. (2016). New photosensitizers for photodynamic therapy. **Biochem. J.** *473*, 347–364.
25. Shimakoshi, H., and Hisaeda, Y. (2019). Bioorganometallic B12 as versatile catalyst for green organic synthesis. in advances in bioorganometallic chemistry (**Elsevier**), pp. 379–398.

26. Juris, A., Balzani, V., Barigelletti, F., Campagna, S., Belser, P., and von Zelewsky, A. (1988). Ru(II)-polypyridine complexes: photophysics, photochemistry, electrochemistry, and chemiluminescence. **Coord. Chem. Rev.** *84*, 85–277.
27. Medlycott, E.A., and Hanan, G.S. (2005). Designing tridentate ligands for ruthenium(II) complexes with prolonged room temperature luminescence lifetimes. **Chem. Soc. Rev.** *34*, 133–142.
28. Thandu, M., Comuzzi, C., and Goi, D. (2015). Phototreatment of water by organic photosensitizers and comparison with inorganic semiconductors. **Int. J. Photoenergy** *2015*, 1–22.
29. Majek, M., Filace, F., and Wangelin, A.J. von (2014). On the mechanism of photocatalytic reactions with eosin Y. **Beilstein J. Org. Chem.** *10*, 981–989.
30. Hedley, G.J., Ruseckas, A., and Samuel, I.D.W. (2017). Light harvesting for organic photovoltaics. **Chem. Rev.** *117*, 796–837.
31. Lovell, J.F., Liu, T.W.B., Chen, J., and Zheng, G. (2010). Activatable photosensitizers for imaging and therapy. **Chem. Rev.** *110*, 2839–2857.
32. Aumaitre, C., Rodriguez-Seco, C., Jover, J., Bardagot, O., Caffy, F., Kervella, Y., López, N., Palomares, E., and Demadrille, R. (2018). Visible and near-infrared organic photosensitizers comprising isoindigo derivatives as chromophores: synthesis, optoelectronic properties and factors limiting their efficiency in dye solar cells. **J. Mater. Chem. A** *6*, 10074–10084.
33. Buck, J.T., Wilson, R.W., and Mani, T. (2019). Intramolecular long-range charge-transfer emission in donor–bridge–acceptor systems. **J. Phys. Chem. Lett.** *10*, 3080–3086.
34. Zhao, J., Wu, W., Sun, J., and Guo, S. (2013). Triplet photosensitizers: from molecular design to applications. **Chem. Soc. Rev.** *42*, 5323–5351.
35. Balzani, V. (2001). Catalysis of electron transfer, heterogeneous systems, gas-phase systems. In *Electron Transfer in Chemistry*. (Wiley-VCH: Weinheim) **5**.

36. Vogler, A., and Kunkely, H. (2000). Photochemistry induced by metal-to-ligand charge transfer excitation. **Coord. Chem. Rev.** *208*, 321–329.
37. Vogler, A., and Kunkely, H. (2006). Photochemistry of peroxy complexes induced by LMCT, MLCT and peroxide IL/LLCT excitation. **Coord. Chem. Rev.** *250*, 1622–1626.
38. Hasegawa, Y., Nakagawa, T., and Kawai, T. (2010). Recent progress of luminescent metal complexes with photochromic units. **Coord. Chem. Rev.** *254*, 2643–2651.
39. Matveev, S.M., Mereshchenko, A.S., Panov, M.S., and Tarnovsky, A.N. (2015). Probing the fate of lowest-energy near-infrared metal-centered electronic excited states: CuCl_4^{2-} and IrBr_6^{2-} . **J. Phys. Chem. B** *119*, 4857–4864.
40. Treffert-Ziemelis, S.M., Golus, J., Strommen, D.P., and Kincaid, J.R. (1993). Resonance raman and time-resolved resonance raman studies of tris(4-methyl-2,2'-bipyridine)ruthenium(II). Polarization of the radical fragment of the $^3\text{MLCT}$ states. **Inorg. Chem.** *32*, 3890–3894.
41. Schatz, P.N., McCaffery, A.J., Suëtaka, W., Henning, G.N., Ritchie, A.B., and Stephens, P.J. (1966). Faraday effect of charge-transfer transitions in $\text{Fe}(\text{CN})_6^{3-}$, MnO_4^- , and CrO_4^{2-} . **J. Chem. Phys.** *45*, 722–734.
42. Yip, A.M.-H., and Lo, K.K.-W. (2018). Luminescent rhenium(I), ruthenium(II), and iridium(III) polypyridine complexes containing a poly(ethylene glycol) pendant or bioorthogonal reaction group as biological probes and photocytotoxic agents. **Coord. Chem. Rev.** *361*, 138–163.
43. Miessler, G.L., Fischer, P.J., and Tarr, D.A. (2014) Inorganic chemistry. "5th Ed.". **Pearson Education Inc.**, 430-431.
44. B. J. McC. (1971). Molecular complexes. R.S. Mulliken and W.B. Person, Wiley-Interscience, New York and London, 1969, pp. 498, **J. Mol. Struct.** *10*, 155–155.

45. Kendrow, C., Baum, J.C., and Marzzacco, C.J. (2009). Investigating the thermodynamics of charge-transfer complexes. A Physical Chemistry Experiment. **J. Chem. Educ.** **86**, 1330.
46. Connell, T.U., and Donnelly, P.S. (2018). Labelling proteins and peptides with phosphorescent d6 transition metal complexes. **Coord. Chem. Rev.** **375**, 267–284.
47. Dixon, I.M., Lebon, E., Sutra, P., and Igau, A. (2009). Luminescent ruthenium–polypyridine complexes & phosphorus ligands: anything but a simple story. **Chem. Soc. Rev.** **38**, 1621-1634.
48. Jain, A., Blum, C., and Subramaniam, V. (2009). Fluorescence lifetime spectroscopy and imaging of visible fluorescent proteins. In *Advances in Biomedical Engineering (Elsevier)*, pp.147–176.
49. Yasuda, R. (2019). Principle and application of fluorescence lifetime imaging for neuroscience. In *Neurophotonics and Biomedical Spectroscopy (Elsevier)*, pp. 53–64.
50. Omary, M.A., and Patterson, H.H. (2017). Luminescence, theory. in *encyclopedia of spectroscopy and spectrometry (Elsevier)*, pp. 636–653.
51. Stadler, E., Eibel, A., Fast, D., Freißmuth, H., Holly, C., Wiech, M., Moszner, N., and Gescheidt, G. (2018). A versatile method for the determination of photochemical quantum yields *via* online UV-Vis spectroscopy. **Photochem. Photobiol. Sci.** **17**, 660–669.
52. Ishida, H., Tobita, S., Hasegawa, Y., Katoh, R., and Nozaki, K. (2010). Recent advances in instrumentation for absolute emission quantum yield measurements. **Coord. Chem. Rev.** **254**, 2449–2458.
53. Allen, M.W., and Scientific, T.F. Measurement of fluorescence quantum yields. 4. <https://www.scribd.com/doc/315476091/Measurement-of-Fluorescence-Quantum-Yields>. (Accessed 30/01/2020)

54. Rurack, K. (2008). Fluorescence quantum yields: methods of determination and standards. in standardization and quality assurance in fluorescence measurements I, U. Resch-Genger, ed. (**Springer Berlin Heidelberg**), pp. 101–145.
55. Marcus, R.A. (1993). Electron Transfer Reactions in Chemistry: Theory and experiment (nobel lecture). **Angew. Chem. Int. Ed. Engl.** **32**, 1111–1121.
56. Formosinho, S., and Arnaut, L. (1997). Electron-transfer reactions in organic chemistry. **Bull. Chem. Soc. Jpn.** **70**, 977–986.
57. D. Ward, M. (1997). Photo-induced electron and energy transfer in non-covalently bonded supramolecular assemblies. **Chem. Soc. Rev.** **26**, 365–375.
58. Wenger, O.S. (2015). Proton-coupled electron transfer with photoexcited ruthenium(II), rhenium(I), and iridium(III) complexes. **Coord. Chem. Rev.** **282–283**, 150–158.
59. de Silva, A.P., Fox, D.B., Huxley, A.J.M., and Moody, T.S. (2000). Combining luminescence, coordination and electron transfer for signaling purposes. **Coord. Chem. Rev.** **205**, 41–57.
60. Marcus, R.A. (1989). Relation between charge transfer absorption and fluorescence spectra and the inverted region. **J. Phys. Chem.** **93**, 3078–3086.
61. Mikhnenko, O.V., Blom, P.W.M., and Nguyen, T.Q. (2015). Exciton diffusion in organic semiconductors. **Energy Environ. Sci.** **8**, 1867--1888.
62. Bolink, H.J., Cappelli, L., Coronado, E., and Gaviña, P. (2005). Observation of electroluminescence at room temperature from a ruthenium(ii) bis-terpyridine complex and its use for preparing light-emitting electrochemical cells. **Inorg. Chem.** **44**, 5966–5968.
63. Hara, D., Komatsu, H., Son, A., Nishimoto, S., and Tanabe, K. (2015). Water-soluble phosphorescent ruthenium complex with a fluorescent coumarin unit for ratiometric sensing of oxygen levels in living cells. **Bioconjug. Chem.** **26**, 645–649.

64. Heinemann, F., Karges, J., and Gasser, G. (2017). Critical overview of the use of ru(ii) polypyridyl complexes as photosensitizers in one-photon and two-photon photodynamic therapy. **Acc. Chem. Res.** *50*, 2727–2736.
65. Chen, B., and Sleiman, H.F. (2004). Ruthenium bipyridine-containing polymers and block copolymers via ring-opening metathesis polymerization. **Macromolecules** *37*, 5866–5872.
66. Liu, Y., Wu, W., Zhao, J., Zhang, X., and Guo, H. (2011). Accessing the long-lived near-IR-emissive triplet excited state in naphthalene diimide with light-harvesting diimine platinum(II) bisacetylde complex and its application for up conversion. **Dalton Trans.** *40*, 9085–9089.
67. Meyer, T.J. (1986). Photochemistry of metal coordination complexes: metal to ligand charge transfer excited states. **Pure Appl. Chem.** *58*, 1193–1206.
68. Angerani, S., and Winssinger, N. (2019). Visible light photoredox catalysis using ruthenium complexes in chemical biology. **Chem. – Eur. J.** *25*, 6661–6672.
69. Diamantis, P., Gonthier, J.F., Tavernelli, I., and Rothlisberger, U. (2014). Study of the redox properties of singlet and triplet tris(2,2'-bipyridine)ruthenium(II) ($[\text{Ru}(\text{bpy})_3]^{2+}$) in aqueous solution by full quantum and mixed quantum/classical molecular dynamics simulations. **J. Phys. Chem. B** *118*, 3950–3959.
70. Ceroni, P., Credi, A., Venturi, M., and Balzani, V. (2010). Light-powered molecular devices and machines. **Photochem. Photobiol. Sci.** *9*, 1561–1573.
71. Paris, J.P., and Brandt, W.W. (1959). Charge transfer luminescence of a ruthenium(II) chelate. **J. Am. Chem. Soc.** *81*, 5001–5002.
72. Armaroli, N. (2001). Photoactive mono- and polynuclear Cu(I)–phenanthrolines. A viable alternative to Ru(II)–polypyridines. **Chem. Soc. Rev.** *30*, 113–124.
73. Johansson, O. (2004). Ruthenium(II) polypyridyl complexes: Applications in artificial photosynthesis. **PhD thesis** (Sweden, Stockholm University).

74. Armstrong, E.A.P., Brown, R.T., Sekwale, M.S., Fletcher, N.C., Gong, X.-Q., and Hu, P. (2004). The unexpected preference for the fac-isomer with the tris(5-ester-substituted-2,2'-bipyridine) complexes of ruthenium(II). **Inorg. Chem.** **43**, 1714–1722.
75. Richard Keene, F. (1997). Stereochemistry and polymetallic ligand-bridged molecular assemblies. **Coord. Chem. Rev.** **166**, 121–159.
76. Abrahamsson, M., Jäger, M., Kumar, R.J., Österman, T., Persson, P., Becker, H.-C., Johansson, O., and Hammarström, L. (2008). Bistridentate ruthenium(II)polypyridyl-type complexes with microsecond ³MLCT state lifetimes: sensitizers for rod-like molecular arrays. **J. Am. Chem. Soc.** **130**, 15533–15542.
77. Maestri, M., Armaroli, N., Balzani, V., Constable, E.C., and Thompson, A.M.W.C. (1995). Complexes of the ruthenium(II)-2,2':6',2''-terpyridine family. Effect of electron-accepting and -donating substituents on the photophysical and electrochemical properties. **Inorg. Chem.** **34**, 2759–2767.
78. Sauvage, J.P., Collin, J.P., Chambron, J.C., Guillerez, S., Coudret, C., Balzani, V., Barigelletti, F., De Cola, L., and Flamigni, L. (1994). Ruthenium(II) and osmium(II) bis(terpyridine) complexes in covalently-linked multicomponent systems: synthesis, electrochemical behavior, absorption spectra, and photochemical and photophysical properties. **Chem. Rev.** **94**, 993–1019.
79. Mongal, B.N., Pal, A., Mandal, T.K., Datta, J., and Naskar, S. (2015). Synthesis, characterisation, electrochemical study and photovoltaic measurements of a new terpyridine and pyridine-quinoline based mixed chelate ruthenium dye. **Polyhedron** **102**, 615–626.
80. Medlycott, E.A., and Hanan, G.S. (2006). Synthesis and properties of mono- and oligo-nuclear Ru(II) complexes of tridentate ligands: The quest for long-lived excited states at room temperature. **Coord. Chem. Rev.** **250**, 1763–1782.

81. Wang, J., Fang, Y.-Q., Hanan, G.S., Loiseau, F., and Campagna, S. (2005). Synthesis and properties of the elusive ruthenium(II) complexes of 4'-cyano-2,2':6',2''-terpyridine. **Inorg. Chem.** *44*, 5–7.
82. Constable, E.C., Cargill Thompson, A.M.W., Armaroli, N., Balzani, V., and Maestri, M. (1992). Ligand substitution patterns control photophysical properties of ruthenium(II)-2,2':6',2''-terpyridine complexes—room temperature emission from [Ru(tpy)₂]²⁺ analogues. **Polyhedron** *11*, 2707–2709.
83. Harriman, A., Mayeux, A., De Nicola, A., and Ziessel, R. (2002). Synthesis and photophysical properties of ruthenium(II) bis(2,2':6',2''-terpyridine) complexes constructed from a diethynylated-thiophene residue. **Phys. Chem. Chem. Phys.** *4*, 2229–2235.
84. Hecker, C.R., Gushurst, Ann.K.I., and McMillin, D.R. (1991). Phenyl substituents and excited-state lifetimes in ruthenium(II) terpyridyls. **Inorg. Chem.** *30*, 538–541.
85. Brewster, T.P., Konezny, S.J., Sheehan, S.W., Martini, L.A., schmittenmaer, c.a., batista, v.s., and crabtree, r.h. (2013). hydroxamate anchors for improved photoconversion in dye-sensitized solar cells. **Inorg. Chem.** *52*, 6752–6764.
86. Wasylenko, D.J., Ganesamoorthy, C., Koivisto, B.D., Henderson, M.A., and Berlinguette, C.P. (2010). Insight into water oxidation by mononuclear polypyridyl Ru catalysts. **Inorg. Chem.** *49*, 2202–2209.
87. Sano, Y., Onoda, A., and Hayashi, T. (2012). Photocatalytic hydrogen evolution by a diiron hydrogenase model based on a peptide fragment of cytochrome c556 with an attached diiron carbonyl cluster and an attached ruthenium photosensitizer. **J. Inorg. Biochem.** *108*, 159–162.
88. Yang, X.-J., Drepper, F., Wu, B., Sun, W.-H., Haehnel, W., and Janiak, C. (2005). From model compounds to protein binding: syntheses, characterizations and fluorescence studies of [Ru^{II}(bipy)(terpy)L]²⁺ complexes (bipy = 2,2'-bipyridine; terpy = 2,2':6',2''-terpyridine; L = imidazole, pyrazole and derivatives, cytochrome c). **Dalton Trans.** *2*, 256–267.

89. Isied, S.S., Ogawa, M.Y., and Wishart, J.F. (1992). Peptide-mediated intramolecular electron transfer: long-range distance dependence. **Chem. Rev.** **92**, 381–394.
90. Winkler, J.R., and Gray, H.B. (1992). Electron transfer in ruthenium-modified proteins. **Chem. Rev.** **92**, 369–379.
91. Luo, J., Reddy, K.B., Salameh, A.S., Wishart, J.F., and Isied, S.S. (2000). Ruthenium Bisbipyridine Complexes of Horse Heart Cytochrome c: Characterization and Comparative Intramolecular Electron-Transfer Rates Determined by Pulse Radiolysis and Flash Photolysis. **Inorg. Chem.** **39**, 2321–2329.
92. Winkler, J.R., and Gray, H.B. (2014). Long-Range Electron Tunneling. **J. Am. Chem. Soc.** **136**, 2930–2939.
93. Kalyanasundaram, K. (1982). Photophysics, photochemistry and solar energy conversion with tris(bipyridyl)ruthenium(II) and its analogues. **Coord. Chem. Rev.** **46**, 159–244.
94. Chang, I.J., Gray, H.B., and Winkler, J.R. (1991). High-driving-force electron transfer in metalloproteins: intramolecular oxidation of ferrocycytochrome c by Ru(2,2'-bpy)2(im)(his-33)3+. **J. Am. Chem. Soc.** **113**, 7056–7057.
95. Jetzschmann, K.J., Yarman, A., Rustam, L., Kielb, P., Urlacher, V.B., Fischer, A., Weidinger, I.M., Wollenberger, U., and Scheller, F.W. (2018). Molecular LEGO by domain-imprinting of cytochrome P450 BM3. **Colloids Surf. B Biointerfaces** **164**, 240–246.
96. Kotani, H., Suenobu, T., Lee, Y.-M., Nam, W., and Fukuzumi, S. (2011). Photocatalytic generation of a non-heme oxoiron(IV) complex with water as an oxygen source. **J. Am. Chem. Soc.** **133**, 3249–3251.

97. Berardi, S., Drouet, S., Francàs, L., Gimbert-Suriñach, C., Guttentag, M., Richmond, C., Stoll, T., and Llobet, A. (2014). Molecular artificial photosynthesis. **Chem. Soc. Rev.** *43*, 7501–7519.
98. Kärkäs, M.D., Verho, O., Johnston, E.V., and Åkermark, B. (2014). Artificial photosynthesis: molecular systems for catalytic water oxidation. **Chem. Rev.** *114*, 11863–12001.
99. Frischmann, P.D., Mahata, K., and Würthner, F. (2013). Powering the future of molecular artificial photosynthesis with light-harvesting metallosupramolecular dye assemblies. **Chem. Soc. Rev.** *42*, 1847–1870.
100. Fukuzumi, S. (2015). Artificial photosynthetic systems for production of hydrogen. **Curr. Opin. Chem. Biol.** *25*, 18–26.
101. Simmons, T.R., Berggren, G., Bacchi, M., Fontecave, M., and Artero, V. (2014). Mimicking hydrogenases: From biomimetics to artificial enzymes. **Coord. Chem. Rev.** *270–271*, 127–150.
102. Skubi, K.L., Blum, T.R., and Yoon, T.P. (2016). Dual Catalysis strategies in photochemical synthesis. **Chem. Rev.** *116*, 10035–10074.
103. Winkler, J.R., Nocera, D.G., Yocom, K.M., Bordignon, E., and Gray, H.B. (1982). Electron-transfer kinetics of penta-ammine ruthenium(III) (histidine-33)-ferricytochrome c. Measurement of the rate of intramolecular electron transfer between redox centers separated by 15.Å in a protein. **J. Am. Chem. Soc.** *104*, 5798–5800.
104. Yocom, K.M., Shelton, J.B., Shelton, J.R., Schroeder, W.A., Worosila, G., Isied, S.S., Bordignon, E., and Gray, H.B. (1982). Preparation and characterization of a penta-ammine ruthenium(III) derivative of horse heart ferricytochrome c. **Proc. Natl. Acad. Sci.** *79*, 7052–7055.

105. Crane, B.R., Di Bilio, A.J., Winkler, J.R., and Gray, H.B. (2001). Electron tunneling in single crystals of *Pseudomonas aeruginosa* azurins. **J. Am. Chem. Soc.** *123*, 11623–11631.
106. Zadvornyy, O.A., Lucon, J.E., Gerlach, R., Zorin, N.A., Douglas, T., Elgren, T.E., and Peters, J.W. (2012). Photo-induced H₂ production by [NiFe]-hydrogenase from *T. roseopersicina* covalently linked to a Ru(II) photosensitizer. **J. Inorg. Biochem.** *106*, 151–155.
107. Ju Youn, H., Terpetschnig, E., Szmecinski, H., and Lakowicz, J.R. (1995). Fluorescence energy transfer immunoassay based on a long-lifetime luminescent metal–ligand complex. **Anal. Biochem.** *232*, 24–30.
108. Ryan, E.M., O’Kennedy, R., Feeney, M.M., Kelly, J.M., and Vos, J.G. (1992). Covalent linkage of ruthenium polypyridyl compounds to poly(L-lysine), albumins, and immunoglobulin G. **Bioconjug. Chem.** *3*, 285–290.
109. Chalker, J.M., Bernardes, G.J.L., Lin, Y.A., and Davis, B.G. (2009). Chemical modification of proteins at cysteine: opportunities in chemistry and biology. **Chem. – Asian J.** *4*, 630–640.
110. Terpetschnig, E., Dattelbaum, J.D., Szmecinski, H., and Lakowicz, J.R. (1997). Synthesis and spectral characterization of a thiol-reactive long-lifetime Ru(II) complex. **Anal. Biochem.** *251*, 241–245.
111. Weh, J., Duerkop, A., and Wolfbeis, O.S. (2007). A resonance energy transfer immunoassay based on a thiol-reactive ruthenium donor dye and a longwave-emitting acceptor. **ChemBioChem** *8*, 122–128.
112. Geren, L., Durham, B., and Millett, F. (2009). Chapter 28 Use of ruthenium photoreduction techniques to study electron transfer in cytochrome oxidase. In *Methods in Enzymology* (**Elsevier**), pp. 507–520.

113. Castellano, F.N., Dattelbaum, J.D., and Lakowicz, J.R. (1998). Long-lifetime Ru(II) Complexes as labeling reagents for sulfhydryl groups. **Anal. Biochem.** **255**, 165–170.
114. Hamachi, I., Tsukiji, S., Shinkai, S., and Oishi, S. (1999). Direct observation of the ferric-porphyrin cation radical as an intermediate in the phototriggered oxidation of ferric- to ferryl-heme tethered to Ru(bpy)₃ in reconstituted myoglobin. **J. Am. Chem. Soc.** **121**, 5500–5506.
115. Immoos, C.E., Di Bilio, A.J., Cohen, M.S., Van Der Veer, W., Gray, H.B., and Farmer, P.J. (2004). Electron-transfer chemistry of Ru-linker-(heme)-modified myoglobin: Rapid intraprotein reduction of a photogenerated porphyrin cation radical. **Inorg. Chem.** **43**, 3593–3596.
116. Glazer, E.C., Nguyen, Y.H.L., Gray, H.B., and Goodin, D.B. (2008). Probing inducible nitric oxide synthase with a pterin–ruthenium(II) Sensitizer wire. **Angew. Chem. Int. Ed.** **47**, 898–901.
117. van der Salm, H., Elliott, A.B.S., and Gordon, K.C. (2015). Substituent effects on the electronic properties of complexes with dipyrrophenazine and triazole ligands: Electronically connected and disconnected ligands. **Coord. Chem. Rev.** **282–283**, 33–49.
118. Mulyana, Y., Keene, F.R., and Spiccia, L. (2014). Cooperative effects in homogenous water oxidation catalysis by mononuclear ruthenium complexes. **Dalton Trans** **43**, 6819–6827.
119. Wüthrich, K. (1986). NMR with proteins and nucleic acids. **Europhys. News** **17**, 11–13.
120. Bax, A., and Davis, D.G. (1985). MLEV-17-based two-dimensional homonuclear magnetization transfer spectroscopy. **J. Magn. Reson.** **1969 65**, 355–360.
121. Piantini, U., Sorensen, O.W., and Ernst, R.R. (1982). Multiple quantum filters for elucidating NMR coupling networks. **J. Am. Chem. Soc.** **104**, 6800–6801.

122. Griesinger, C., and Ernst, R.R. (1987). Frequency offset effects and their elimination in NMR rotating-frame cross-relaxation spectroscopy. **J. Magn. Reson.** **1969 75**, 261–271.
123. Suzuki, K., Kobayashi, A., Kaneko, S., Takehira, K., Yoshihara, T., Ishida, H., Shiina, Y., Oishi, S., and Tobita, S. (2009). Reevaluation of absolute luminescence quantum yields of standard solutions using a spectrometer with an integrating sphere and a back-thinned CCD detector. **Phys. Chem. Chem. Phys.** **11**, 9850–9860.
124. Zhou, M., Robertson, G.P., and Roovers, J. (2005). Comparative study of ruthenium(II) Tris(bipyridine) Derivatives for Electrochemiluminescence Application. **Inorg. Chem.** **44**, 8317–8325.
125. Jakubikova, E., Chen, W., Dattelbaum, D.M., Rein, F.N., Rocha, R.C., Martin, R.L., and Batista, E.R. (2009). Electronic structure and spectroscopy of $[\text{Ru}(\text{tpy})_2]^{2+}$, $[\text{Ru}(\text{tpy})(\text{bpy})(\text{H}_2\text{O})]^{2+}$, and $[\text{Ru}(\text{tpy})(\text{bpy})(\text{Cl})]^+$. **Inorg. Chem.** **48**, 10720–10725.
126. Gao, X.-D., Li, X.-M., and Gan, X.-Y. (2013). Enhancing the light harvesting capacity of the photoanode films in dye-sensitized solar cells. *Sol. Cells - Res. Appl. Perspect. Intechopen Europe*, 169-202
127. Tsai, C.-N., Allard, M.M., Lord, R.L., Luo, D.-W., Chen, Y.-J., Schlegel, H.B., and Endicott, J.F. (2011). Characterization of low energy charge transfer transitions in (terpyridine)(bipyridine)ruthenium(II) complexes and their cyanide-bridged bi- and tri-metallic analogues. **Inorg. Chem.** **50**, 11965–11977.
128. Braun, J.D., Lozada, I.B., Kolodziej, C., Burda, C., Newman, K.M.E., van Lierop, J., Davis, R.L., and Herbert, D.E. (2019). Iron(II) coordination complexes with panchromatic absorption and nanosecond charge-transfer excited state lifetimes. **Nat. Chem.** **11**, 1144–1150.
129. Navon, Gil., and Sutin, Norman. (1974). Mechanism of the quenching of the phosphorescence of tris(2,2'-bipyridine) ruthenium(II) by some cobalt(III) and ruthenium(III) complexes. **Inorg. Chem.** **13**, 2159–2164.

130. Creutz, C., Chou, M., Netzel, T.L., Okumura, M., and Sutin, N. (1980). Lifetimes, spectra, and quenching of the excited states of polypyridine complexes of iron(II), ruthenium(II), and osmium(II). **J. Am. Chem. Soc.** *102*, 1309–1319.
131. Thompson, D.W., Ito, A., and Meyer, T.J. (2013). $[\text{Ru}(\text{bpy})_3]^{2+*}$ and other remarkable metal-to-ligand charge transfer (MLCT) excited states. **Pure Appl. Chem.** *85*, 1257–1305.
132. Zampella, G., Bruschi, M., Fantucci, P., and De Gioia, L. (2005). DFT Investigation of H_2 Activation by $[\text{M}(\text{NHPnPr}_3)(\text{S}_3)]$ (M = Ni, Pd). Insight into Key Factors relevant to the design of hydrogenase functional models. **J. Am. Chem. Soc.** *127*, 13180–13189.
133. Butler, J., Koppenol, W.H., and Margoliash, E. (1982). Kinetics and mechanism of the reduction of ferricytochrome c by the superoxide anion. **J. Biol. Chem.** *257*, 10747–10750.
134. Lu, Y., Conway-Kenny, R., Twamley, B., McGoldrick, N., Zhao, J., and Draper, S.M. (2017). 1,10-Phenanthroline ruthenium(II) complexes as model systems in the search for high-performing triplet photosensitisers: Addressing Ligand versus metal effects. **Chem. Photo. Chem.** *1*, 544–552.
135. Batinić-Haberle, I., Spasojević, I., Stevens, R.D., Hambright, P., and Fridovich, I. (2002). Manganese(III) meso-tetrakis(ortho-N-alkylpyridyl)porphyrins. Synthesis, characterization, and catalysis of O_2^- dismutation. **J. Chem. Soc. Dalton Trans.** *13*, 2689–2696.
136. Sullivan, B.P., Calvert, J.M., and Meyer, T.J. (1980). Cis-trans isomerism in $(\text{trpy})(\text{PPh}_3)\text{RuCl}_2$. Comparisons between the chemical and physical properties of a cis-trans isomeric pair. **Inorg. Chem.** *19*, 1404–1407.

Chapter Two

**Building a photosensitizing framework
for a class of artificial porphyrin-based
hydrogenases**

2.1. Introduction

In the last century, modern society has reached a peak of energy consumption, which is required to sustain its technological progress and population growth. Fossil fuel is the primary source of energy, despite its impact on environmental pollution, global warming, and limited supply. According to a report from the International Energy Agency, “By 2040, it is expected that the global energy demand will expand about 30%, and the CO₂ emissions will reach as large as 35.7 Gt.year⁻¹”¹⁻⁴. Hence, developing alternative sources of energy, replacing or minimizing the utility of fossil fuel, is one of the most urgent societal challenges.

Different sustainable and renewable alternatives to fossil fuel were developed to address environmental and energy crises, such as Solar, wind, and hydropower energies³⁻⁶. Among all renewable energy sources, solar energy represents one of the most efficient sources of energy. However, the spatial and temporal intermittency is an essential limitation to the wide spreading of its applications^{7,8}. One of the promising solutions is to transform solar energy by converting it into a chemical fuel that can be easily stored and transport^{4,7}. There are diverse processes (so-called artificial photosynthesis) for harnessing sunlight and transforming its energy into chemical bonds, such as the formation of molecular hydrogen from water or hydrocarbons from CO₂⁷.

In Nature, photosynthesis is the way for harnessing sunlight in plants, and for converting its energy to the chemical bonds of glucose molecules. Photosystem II (PSII) is a large membrane-bound enzyme that is proficient in harvesting sunlight through the photo-induced charge separation process. In such process, the absorbed photon by chlorophyll is used to transfer the electron gained from water, by fascinating pathway, to a primary acceptor, and then further through an electron cascade towards the final acceptor in the reaction center, where the carbon dioxide

is converted to glucose, **Figure (2.1)**^{9,10}. Many researchers have devoted their efforts to developing PSII-inspired photocatalysts, suitable in the formation of small molecules such as hydrogen, carbon dioxide, and oxygen, robust, clean, and sustainable energy vectors.

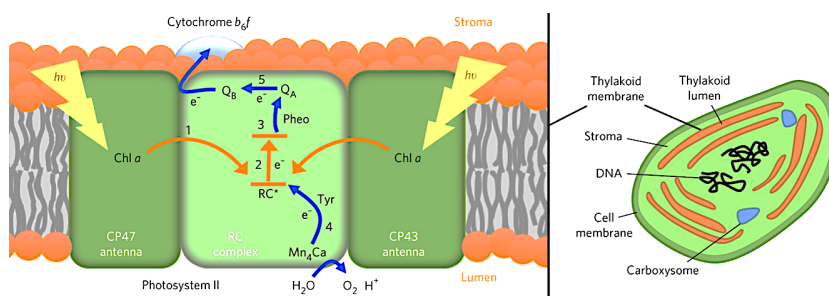
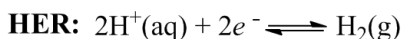


Figure (2.1). Schematic representation of the energy/charge transfer pathways in the PSII from the thylakoid membrane of a cyanobacterium. The numbers indicate the sequence of the energy and charge transfer pathways. The orange arrows represent energy transfer pathways resulting from light ($h\nu$) absorption. The blue arrows represent CT pathways in oxygenic photosynthesis. [Reproduced from 'Ref. 10' with permission of the publisher]

Hydrogen (H_2) is one of the most efficient and eco-friendly fuels. Among all chemical fuels, it has the highest gravimetric energy density (142 MJ.kg^{-1}), and it is considered as the ultimate eco-friendly energy carrier, as the consumption of hydrogen, produces zero-emission of carbonaceous species^{4,11}. However, over 95% of hydrogen is currently produced upon the reforming of fossil-fuels, a CO_2 -releasing process¹². On the other hand, water electrolysis is a clean process for hydrogen and oxygen production by so-called hydrogen evolution reaction (**HER**) and oxygen evolution reaction (**OER**), which still represent no more than 4% of the currently used processes, **Scheme (2.1)**. The low-scale production and the lack of cheap and effective processes for water splitting are the main drawbacks to its widespread implementation¹³⁻¹⁵.

Chemical reactions involved in water splitting

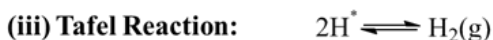


Scheme (2.1)

The fundamental target of electrochemical hydrogen evolution is the minimization of the overpotential requirement in the cathodic reduction under acidic medium. The mechanistic understanding of the hydrogen evolution under mainly acidic conditions is essential for further development of novel materials with enhanced activity and stability for HERs^{13,14}.

Under acidic media, the cathodic reduction of dissolved protons in water (the hydronium ions H_3O^+) generates gaseous hydrogen molecules. Thermodynamically, this process occurs at the reduction potential of the normal hydrogen electrode (NHE), and it is a multi-step electrode reaction:

Chemical reactions involved in electrochemical hydrogen evolution.



Where the 2H^\bullet : Adsorbed hydrogen atom

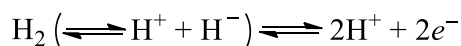
Scheme (2.2)

The **Volmer reaction, (i) in Scheme (2.2)**, the reduction of the adsorbed proton in the active sites of the catalyst surface (i.e., electrode surface), followed by molecular hydrogen (H_2) evolution either through **Heyrovsky mechanism, (ii) in Scheme (2.2)**, in which the second electron/proton transfer occurs, or through

Tafel mechanism, (iii) in **Scheme (2.2)**, the couple of adsorbed and reduced hydrogen atoms recombined together¹⁵⁻¹⁷. Usually, one step is kinetically limiting the reaction rate (called the rate-determining step), which strongly depends on the catalyst nature (i.e., the electrode type)¹⁵. Therefore, it is clear that the kinetics depends on several parameters depending on the catalyst itself, such as its composition, surface orientation, and the topology of the active-site (at that specific surface of the electrode). Other important parameters are critical, such as durability, stability, and oxygen-sensitivity of the catalyst in carrying hydrogen reduction reaction, which also should be considered. In this respect, many recent efforts are focusing on the design and the development of novel materials and catalysts for the electrochemical hydrogen evolution, or even on alternative processes, such as light-driven catalysis of the HERs. In particular, even more attention is conveyed to the bio-inspired model systems, for instance, hydrogenase-like catalysts¹⁸.

2.1.1. Hydrogenases: natural enzymes for hydrogen reduction

Nature possesses active catalysts, called hydrogenases (HGs), for both the hydrogen oxidation (conversion of molecular dihydrogen into protons and electrons) and its reduction (the formation of molecular dihydrogen):¹⁹



HGs are widespread in Nature, e.g., Archaea, Bacteria, and in a few Eukarya, whose primary function is to provide the energy needed by the organisms, through oxidation of molecular hydrogen and to balance the redox potential of the cell^{19,20}. HGs can be classified, based on their metal-center active sites (where the reaction takes place, and the heterolytic splitting of molecular hydrogen occurs), in three classes: [FeFe], [NiFe], and [Fe] hydrogenases, **Figure (2.2)**²¹.

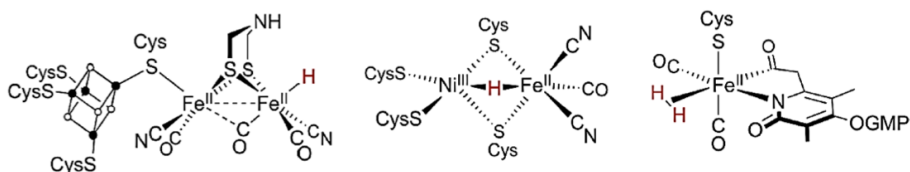


Figure (2.2). Schematic representations of [FeFe] (**Left**), [NiFe] (**Mid**), and [Fe] (**Right**) HGs the active sites. The magenta **H**'s represent the hydrogen binding the vacant coordination site of the metal-cofactor. [*Reproduced from Ref. 21, with permission of the publisher*]

The [FeFe] and [NiFe] HGs are undoubtedly the most studied. They are characterized by iron atoms that are coordinated by CN^- and CO^- ligands and by sulfur-bridged bimetallic clusters, with an open coordination site on one metal site, where the reaction takes place, **Figure (2.2)**¹⁹. Hydrogen can reach the active sites by a hydrophobic gas channel, and the electrons, produced from H_2 oxidation or required for H^+ reduction, generally transfer through an iron-sulfur cluster adjacent to the metal center, **Figure (2.3)**. The third class of HGs is the [Fe] HG, which has a peculiar and unique coordination sphere. These enzymes, so-called “[Fe] hydrogenases or iron-only hydrogenases” can activate H_2 only in the presence of a second substrate, the methenyltetrahydromethanopterin (Methenyl-H4MPT⁺)²¹.

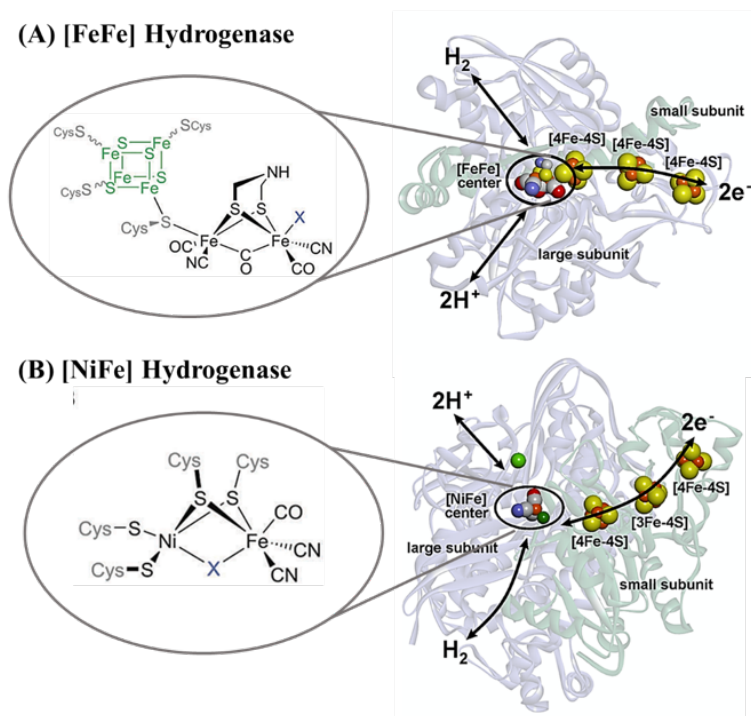


Figure (2.3). Representative model structures of [FeFe] HG (A) and [NiFe] HG (B). The corresponding active sites depicted inside balloons (The site of catalytic H_2 /proton turnover is marked with X). [Insert: Schematic arrows in the model, indicating the CT chain (via iron–sulfur centers), and the pathways for the dihydrogen and the proton transfer]. [Reproduced from ‘Ref. 19, Ref. 22’ with permission of the publisher]

2.1.1.1. [FeFe] Hydrogenases

[FeFe] HGs are considered the highest catalytically active enzymes for the hydrogen production (ca. $8,000 \mu\text{mol } H_2 \text{ min}^{-1}\text{mg}^{-1}$ of protein and TOF ca. $10,000 \text{ s}^{-1}$)^{23–25}. [FeFe] HGs can be found in bacteria and some eukaryotes, in particular, anaerobic prokaryotes, and play important roles in the energy and carbon metabolism in anoxic ecosystems^{26–28}.

[FeFe] HGs are complex metalloproteins that catalyze the reversible reduction of protons to molecular hydrogen in the active site, so-called “*H*-cluster.” The *H*-

cluster in [FeFe] HGs is the assembly of two distinct iron-sulfur sub-clusters, the diiron-bridged sub-cluster ([2Fe]_H) linked to a proximal [4Fe4S] cubane sub-cluster ([4Fe]_H) via a Cysteine (Cys) residue, the latter attaching to the protein scaffold via three more Cys residues, **Figure (2.4)** ²⁹.

Four proximal residues in *H-cluster*, Cys299, Glu279, Ser319, and Glu282, **Figure (2.4)** ²⁹, are involved in the process of the proton transport towards and away from the active site. The “required or produced” electrons in hydrogen “reduction or oxidation” reaction are transferred through a channel of [4Fe4S] iron-sulfur clusters ²⁹. The crystallographic structure obtained from *Clostridium pasteurianum* ^{30–32}, *Desulfovibrio desulfuricans* ³³, and the eukaryotic algae *Chlamydomonas reinhardtii* ^{34,35} have shown similar architecture of the active site, which consisted of a [4Fe4S] cluster domain linked with the *H-cluster* ²⁸.

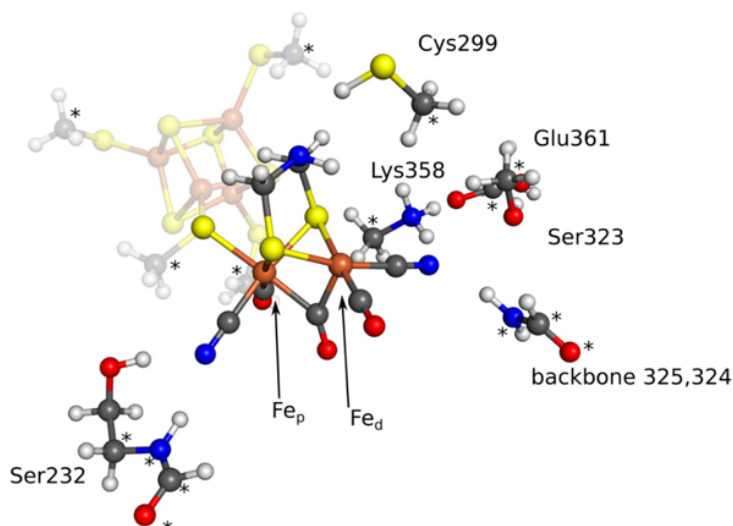


Figure (2.4). The model structure represents the (*H-cluster*) active site of the [FeFe] HGs and the auxiliary residues in the second sphere. It shows the proximal (Fe_p) and distal (Fe_d) iron-centers, and the auxiliary residues for proton transport (Ser232, Cys299, Ser323, Lys258, and Glu361). [Reproduced from ‘Ref. 29’ with permission of the publisher]

Both the $[4\text{Fe}]_{\text{H}}$ cubane, and the $[2\text{Fe}]_{\text{H}}$ di-iron active site are active redox species, which can go through six different oxidation states. Two different oxidation states (+2 and +1) are available for the cubane sub-cluster and three states for the diiron center $[\text{Fe}_p^{\text{II}}\text{Fe}_d^{\text{II}}]$, $[\text{Fe}_p^{\text{I}}\text{Fe}_d^{\text{II}}]$, and $[\text{Fe}_p^{\text{I}}\text{Fe}_d^{\text{I}}]$. However, under physiologic conditions, only a few of these states are accessible, the “active oxidized” state $\text{H}_{\text{ox}}([\text{4Fe}]_{\text{H}}^{2+}-[\text{Fe}_p^{\text{I}}\text{Fe}_d^{\text{II}}])$ and the “active reduced state” state $\text{H}_{\text{red}}([\text{4Fe}]_{\text{H}}^{2+}-[\text{Fe}_p^{\text{I}}\text{Fe}_d^{\text{I}}])$ ³⁶.

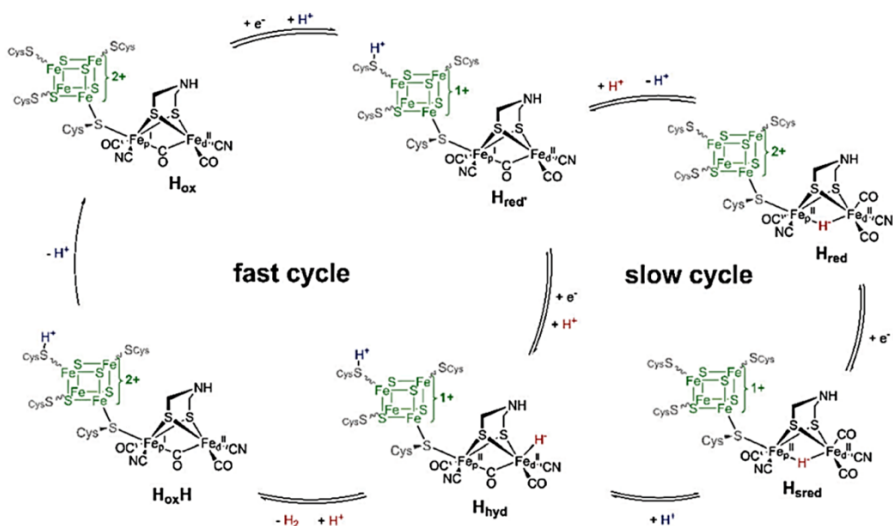
The catalytic cycle of the $[\text{FeFe}]$ HG is not well-recognized, as the participation in the catalytic cycle of certain redox species is still not clear²². The first reported catalytic cycle is named the slow cycle, **Scheme (2.3)**. It starts from the H_{ox} that is converted to H_{red} by a proton-coupled electron transfer (PCET) on the $[4\text{Fe}]_{\text{H}}$ sub-cluster. The PCET renders the formation of H_{red} charge neutral and facilitate a second reduction step at a similar redox potential. The $\text{H}_{\text{ox}}-\text{H}_{\text{red}}$ transition appears more likely than a direct conversion into H_{red} , which would result in drastic ligand reorientation and loss of the “rotated structure”²². The formation of H_{red} evolves at high concentration of protons in acidic solutions, which lead to the protonation of the $[2\text{Fe}]_{\text{H}}$ site and withdrawal of electron density from the $[4\text{Fe}]_{\text{H}}$ sub-cluster, resulting in a bridging hydride (μH^-), subsequently leading to the reduced form (H_{sred}).

The alternative proposed pathway, named the fast cycle, **Scheme (2.3)**, is about the protonation and reduction of H_{red} to form the H_{hyd} , then the H_{hyd} intermediate, accessible to further protonation, yields to H_2 release and recovery of the protonated resting state ($\text{H}_{\text{ox}}\text{H}$), which still carries an additional proton at the $[4\text{Fe}]_{\text{H}}$ sub-cluster and after losing this “regulatory” proton, the H_{ox} is formed, and the catalytic cycle can start over again²².

The μH^- ligand is thermodynamically more stable than a terminal hydride, and therefore, reacts slowly with additional protons in the H_2 release reaction.

Moreover, the formation of H_{hyd} from H_{sred} requires another geometry reorganization. Given that, the participation of H_{red} and H_{sred} as catalytic intermediates in hydrogen turnover is therefore under question ²².

Proposed catalytic cycle of [FeFe] HGs



Scheme (2.3)

[Reproduced from 'Ref. 22' with permission of the publisher]

2.1.1.2. [NiFe] Hydrogenases

[NiFe] HGs are widespread in bacteria and archaea, are usually involved in H_2 oxidation, making the high reducing power of this substrate available to the cell ³⁷. In contrast to [FeFe] HGs, which are oxygen-sensitive enzymes, [NiFe] HGs are oxygen tolerant, and therefore, there is a growing interest toward the understanding of their biogenesis and catalytic mechanism ³⁸.

[NiFe] HGs are composed of two subunits, one being larger than the other about 34 kDa. The large subunit bears the [NiFe] bimetallic active site, and the small subunit contains the iron-sulfur clusters. In contrast to the [FeFe] HGs, the iron-

sulfur clusters in [NiFe] HGs are composed of three different sites: the proximal and distal [4Fe4S] clusters, and the medial [3Fe4S] cluster. These facilitate long-range transfer of electrons and protons from the surface toward the active site and vice versa during H₂ oxidation or H⁺ reduction^{20,39}.

The bimetallic [NiFe] active site is coordinated to the protein backbone through four cysteine residues: two-terminal cysteine are ligated to the Ni metal, and the others are bridging both the Ni and Fe. Besides, The iron is coordinated by strong π -acid CO⁻ and two CN⁻ ligands, which keep the iron site at low spin^{39,40}, **Figure (2.5)**.

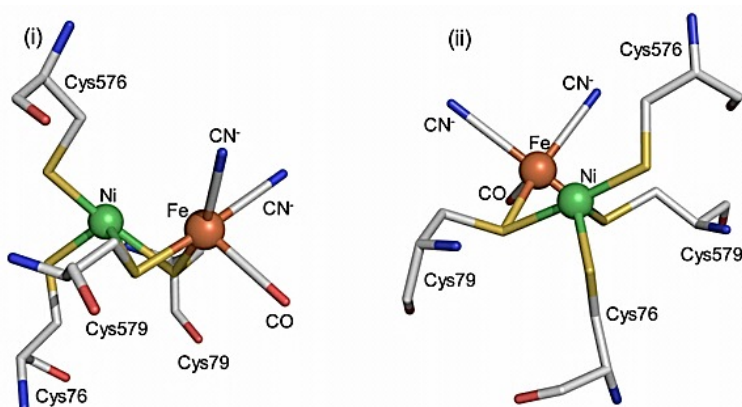


Figure (2.5). The chemical structure of the [NiFe] active site; represents the amino-acids that forming the 1st-coordination sphere around the metal-cluster. Structures have taken from crystallographic data for *E. coli* Hyd-1 (PDB ID 3USE). [Reproduced from 'Ref. 39' with permission of the publisher]

Beyond the four cysteine residues and the π -acid ligands, which represented the first coordination sphere of the active site, the second coordination sphere involves conserved amino acids (Glu28, Asp118, Arg509, and Asp574) that surround, but not directly coordinate the active site, **Figure (2.6)**. These play a crucial role in proton-transfer mechanism³⁹.

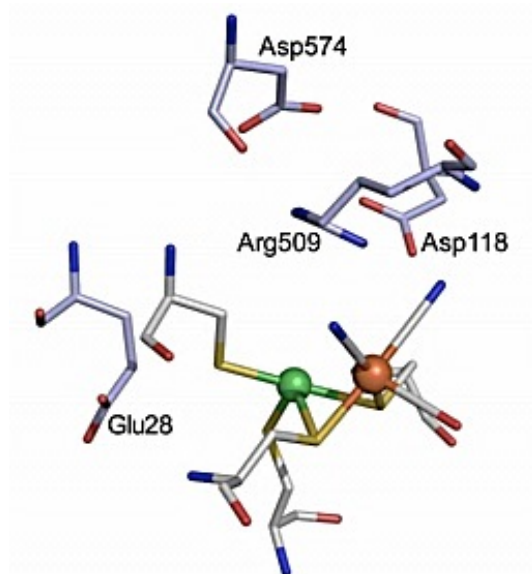


Figure (2.6). Chemical structure of the active site of [NiFe] HGs presenting the position of additional highly conserved amino acid residues. [*Reproduced from 'Ref. 39' with permission of the publisher*]

The catalytic cycle of [NiFe] HGs starts from the resting state, called Ni-Sia, **Figure (2.7)**. The nickel ion is four-coordinated with one open bridge; both metals are in the (+2)-oxidation state. The hydrogen reaches the active site through the gas-channel, then a Ni-mediated heterolytic splitting occurs, releasing protons and hydride ions. A proton jumps to the Cys546 residues, while the hydride ion bridges the two metal ions. This second state in the catalytic cycle is named Ni-R. The latter releases the proton from cysteine-546 and one electron from nickel ion, evolving in a paramagnetic state, identified as Ni-C. The loss of a further electron and a proton leads back to Ni-Sia closing the cycle. Under aerobic conditions, dioxygen constantly inactivates hydrogen catalytic cycle, nonetheless two alternative catalytic cycles may proceed, which end up with the release of water molecules, as shown in, **Figure (2.7)**. However, inactivation of the hydrogenases

catalytic activity may occur due to the accumulation of water molecules in the highly hydrophobic active site ^{19,41}.

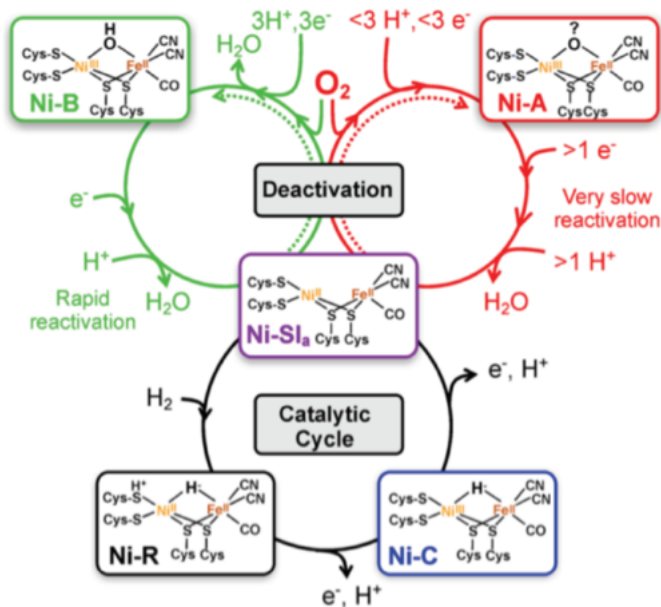


Figure (2.7). Schematic representation of the catalytic cycle for [NiFe] HGs (**Black**). Deactivation and reactivation cycles for [NiFe] HGs (**Red and Green**). [Reproduced from 'Ref. 19' with permission of the publisher]

2.1.1.3. [Fe] Hydrogenases

[Fe] HGs are found only in methanogenic archaea bacteria, and it was thought that the [Fe] HGs were metal free. Until 2004, when it was discovered that the active site includes one iron metal and no iron-sulfur clusters in these enzymes. This HG class is less studied and not well-known in comparison to the other two classes ([FeFe] and [NiFe] HGs) ^{42,43}.

[Fe]-only HGs have a fundamentally different mechanism in terms of redox partners and how electrons transfer to the active site. Unlike the other two HGs classes, which promote long-distance electron transfer assisted by a series of iron-

sulfur cubane clusters, in [Fe]-only HGs, the electrons are directly transferred to the active site by the very close Methenyl-H4MPT⁺ cofactor. The latter cofactor directly accepts the hydride from H₂ in the process. Moreover, the enzyme changes its conformation from close to open when two equivalents of methenyl-H4MPT⁺ bind the enzyme. [Fe]-only hydrogenase is also known as “H₂-forming methylene-H4MPT dehydrogenase”, because its function is the reversible reduction of methenyl-H4MPT⁺ to methylene-H4MPT⁺ ^{42,44}, **Figure (2.8)**.

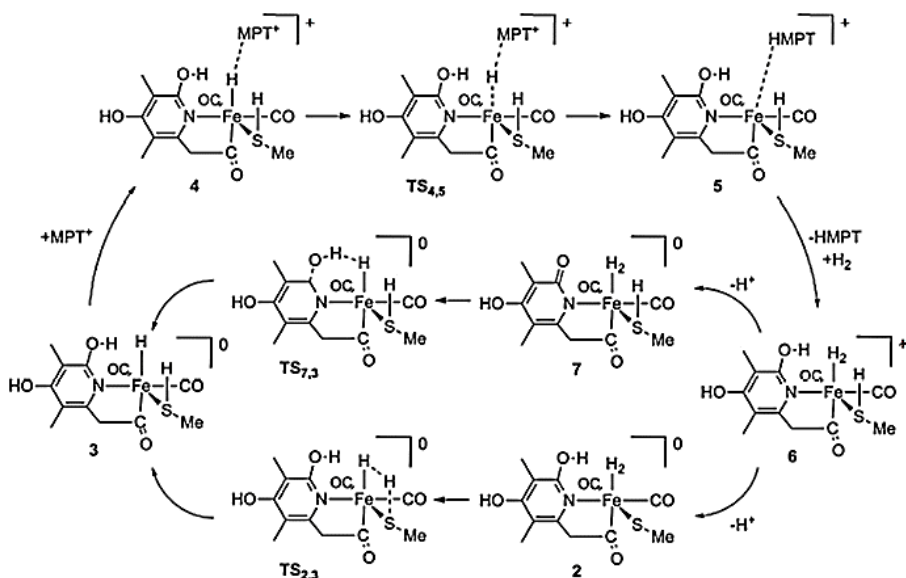


Figure (2.8). Schematic image for the proposed catalytic cycle of the [Fe]-only HGs.

The catalytic cycle of [Fe]-only HGs starts with the binding of methenyl H4MPT⁺ to the open form of the enzyme, **step 4** in **Figure (2.8)** ³⁶. The hydrogen enters toward the active site through a hydrophobic gas-channel. Then, the Fe-cofactor is activated, and a hydrogen molecule binds to the open coordination site, **step 6** in **Figure (2.8)**. The hydrogen molecule is heterolytically cleaved, the proton transferred to the thiol-group of Cys176, **step 2** in **Figure (2.8)**, and the adjacent C14a carbocation of the methenyl-H4MPT⁺ accepts the hydride ion, **step 5** in **Figure (2.8)** ⁴⁵.

2.1.2. Artificial peptides and model systems for HERs

Living organisms produce fascinating enzymes with high catalytic activity, which are exploited by biotechnology in biosynthetic systems, or they can inspire new artificial enzymes mimicking their active sites^{46,47}. These bio-inspired catalysts have versatile applications to diverse fields, e.g., in redox processes, organic synthesis, bio-sensors, and fuel-cell technologies^{48,49}.

HGs represent an example of natural enzymes, whose exploitation would be very much auspicated for catalyzing hydrogen evolution from water near thermodynamic potentials. However, oxygen sensitivity, lack of stability, and low density of active sites due to its mass are limiting their potential application¹⁹. Therefore, the design of bio-inspired model systems or miniaturized artificial enzymes mimicking their active site is a growing field in the literature⁵⁰⁻⁵².

In particular for the H-cluster from [FeFe]-hydrogenases, many attempts have been made in understanding the structure to function relationships behind their catalytic activity. Residues and inorganic ligands of the first and second coordination-spheres have been substituted, and their effect to activity, stability, and turnover numbers has been studied, **Figure (2.9)**⁵³⁻⁵⁶. The learned lessons are considered as the basis in the development of new bioinorganic catalysts for HER either by electrochemical or photochemical water splitting. Herein, we are going to give an insight about some of the artificial or model systems that were inspired by the HGs.

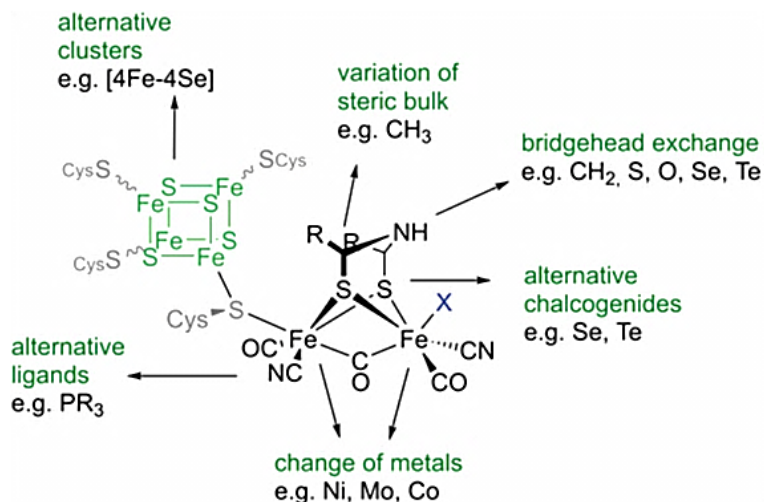


Figure (2.9). Possible alterations of the H-cluster, the active site of [FeFe] HGs. [Reproduced from 'Ref. 22' with permission of the publisher]

In 2005, Picket et al. reported an active site model similar to the architecture of the HGs active site, **Figure (2.10)**, in which a $[\text{Fe}_2(\mu\text{-SR})_3(\text{CO})_5]$ unit attaches the [4Fe4S] cubane cluster via a thiolate bridge⁵⁷, which have been used in providing a route to advanced electrode materials.

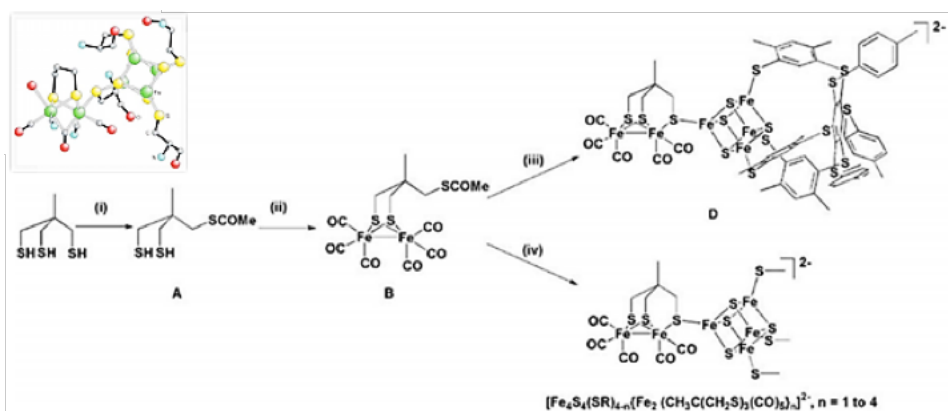
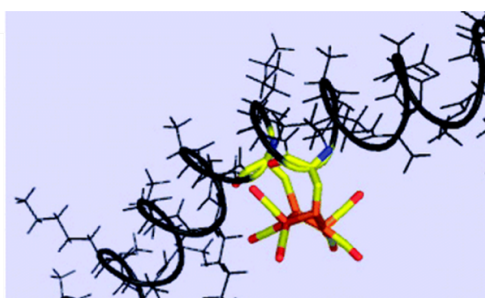


Figure (2.10). Synthetic pathways for the assembling of the H-cluster model. Insert: The Composite structure of the native H-cluster. [Reproduced from 'Ref. 57' with permission of the publisher]

In 2007, Dutton and coworkers reported another active site model of [FeFe] HGs (so-called SynHyd1). *De-novo* design and solid-phase peptide synthesis were coupled to develop a cysteine-containing peptide that reacts with $\text{Fe}_3(\text{CO})_{12}$ to assemble a *maquette*, which binds a diiron cluster close to the [FeFe] hydrogenase diiron site. A simple peptide sequence was prepared that placed two cysteine side chains in the I and i+3 position (CXXC), necessary for the formation of the diiron complex on the same face of an α -helix⁵⁸, **Figure (2.11)**.



Peptide Sequence: $\text{NH}_2\text{-AAKAAAAKAACAKCAAAKAAAAKAAAAKAAAAKAAW-CONH}_2$

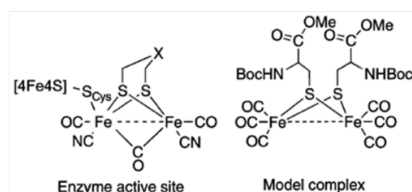


Figure (2.11). Representative structure of the HGs Dutton maquette, SynHyd1 (**Top**). A single peptide sequence incorporated and modulated the [FeFe] HGs model cluster utilizing the cysteine ligands (**Bottom**). [Reproduced from 'Ref. 58' with permission of the publisher]

In 2010, Darensbourg and co-workers reported another small bio-inspired model of [FeFe] hydrogenases. In this model, a new diiron cluster mimicking the *H-cluster* active site, complex-1 in **Figure (2.12)**, has been hosted and included by two β -cyclodextrins (β -CyD), which provided a hydrophobic cavity suitable to host organometallic motifs, and the hydrophilic hydroxyl rims provide hydrogen bonding sites⁵⁹.

Syntheses of Complex 1 and 1-CyD

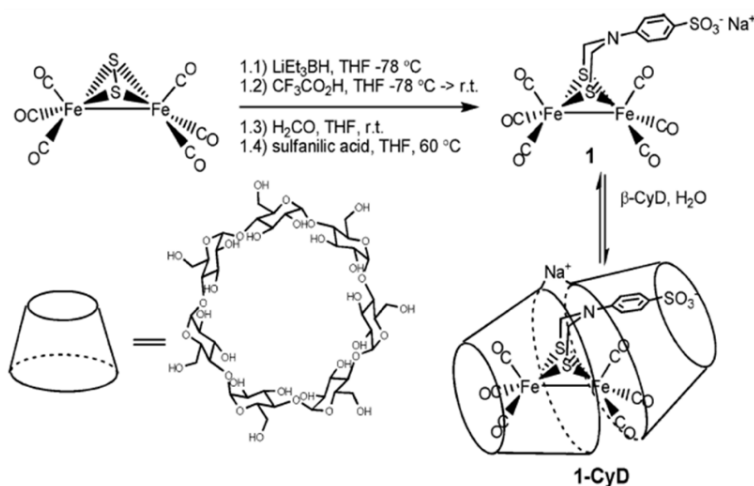


Figure (2.12). Synthesis of the [FeFe] HGs active site model (complex-1) and the (cyclodextrin-complex 1) model system. [Reproduced from 'Ref. 59' with permission of the publisher]

All of the previously reported work illustrated few examples in preparing differently designed models, as attempts to reproduce the enzymatic activity of the [FeFe] HGs active site.

Further effort was focused in developing bio-inspired systems for the hydrogen evolution either by electric-potential or light-driven catalytic systems. Hayashi and coworkers in 2011 and 2012 reported the light-driven photocatalytic H_2 evolution by a diiron $[\text{Fe}_2(\text{CO})_6]$ cluster datively linked to an artificial protein and peptide moieties, respectively. In the first report, the diiron cluster was linked to the two cysteine residues of the native CXXC sequence (Cys14 and Cys17) from the apocytochrome c matrix. It was activated via light-photosensitization by an intermolecular electron transfer, which was promoted by a photoexcited $[\text{Ru}^{\text{II}}(\text{bpy})_3]$ complex in the presence of ascorbate as electron sacrificial agent ⁶⁰, **Figure (2.13, A)**. In the second report, an intramolecular photochemical system

was designed, consisting of both the diiron cluster and a ruthenium(II)-complex ($[\text{Ru}^{\text{II}}(\text{bpy})(\text{tpy})(\text{Cl}^-)]$ photosensitizer) attached to the Cys and His residues, respectively, from the CXXCH sequence of the hydrolytically cleaved C-terminal segment of cytochrome c556 (Octadecapeptide, YIGKACGNCHENFRDKEG)⁶¹, **Figure (2.13, B)**.

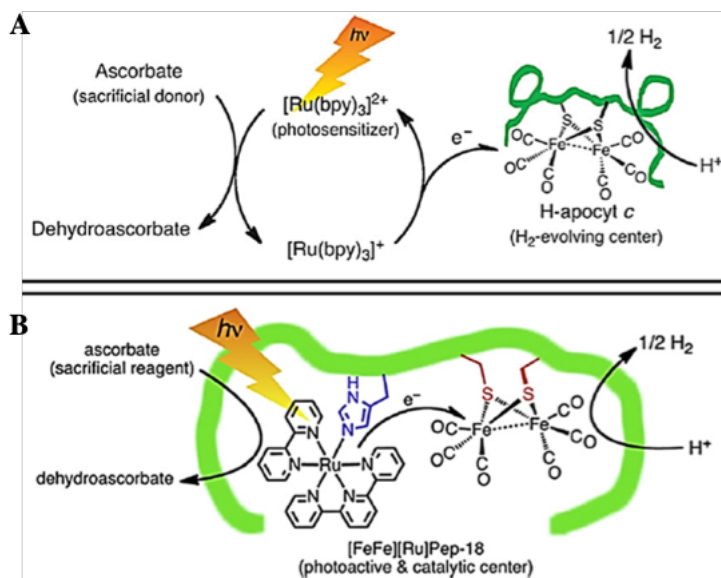


Figure (2.13). Proposed catalytic cycle for the photochemical reduction of protons catalyzed by H-apocyt c in aqueous media (A). [Reproduced from Ref. 60] Proposed catalytic cycle for the photochemical reduction of protons by $[\text{FeFe}][\text{Ru}]\text{Pep-18}$ in aqueous media (B). [Reproduced from 'Ref. 60, 61' with permission of the publisher]

Further bioinspired model systems for electrochemical water splitting including alternative metal cofactors (Fe, Ni, Co ...etc) incorporated inside tetra, and Penta chelated nitrogen and phosphine ligands (e.g., porphyrin, bis-(iminopyridine), 104euteron104e, cyclic diphosphine) have been proposed in **Figure (2.14)**⁶²⁻⁷⁴. These alternative model systems were developed and studied both in the reengineering of biomolecular systems, and to address the previously described limitations of HGs enzymes.

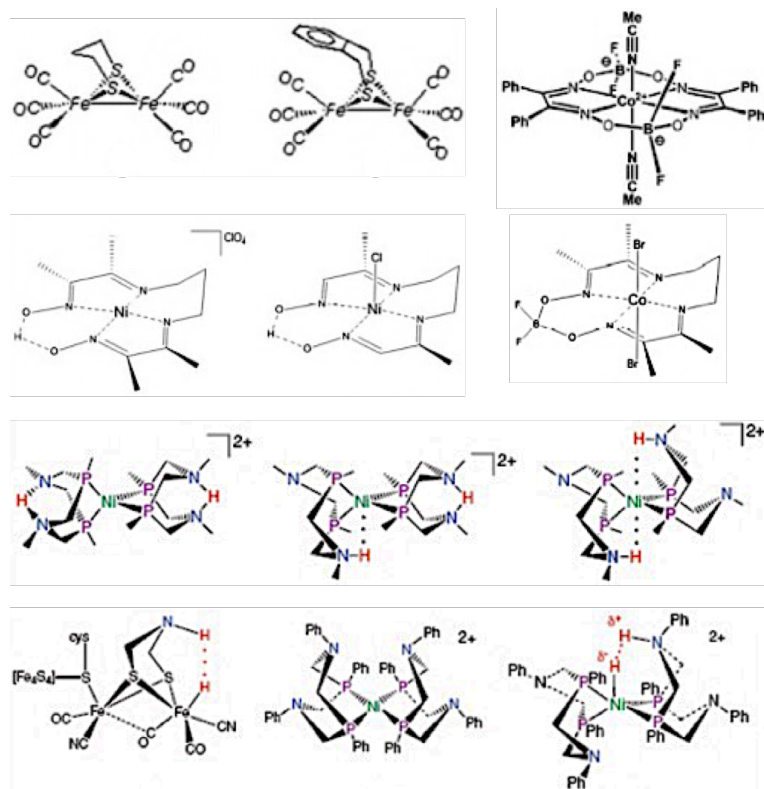


Figure (2.14). Chemical structures of some proposed bio-inspired model systems from HGs active sites reported in the literature. [Reproduced from 'Ref. 62-71']

In 2014, the Bren group reported the first example of bioinorganic catalyst for HERs, involving the cobalt(III)-microperoxidase-11 (Co^{III} -MP11), **Figure (2.15)**, a porphyrin base covalently-linked with the Cyt-c-derived undecapeptide sequence incorporating cobalt metal into the porphyrin tetra-dentate cavity. This bio-inspired system contains a heme c group that is covalently linked through two thioethers bonds to Cys residues of the peptide chain (CXXCH motif), and the role of the proximal His residue is to provide the fifth coordination ligand to the cobalt metal ⁷⁵.

This small artificial and single-chain peptide has shown high activity in electrochemical hydrogen evolution from water splitting at physiological pH. It demonstrated to be oxygen tolerant, with TOF near 6.7 s^{-1} and overpotential of 852 mV. However, the Co^{III} -MP11 is limited in its durability as it bleached rapidly in a few hours (cycling $2.5 \cdot 10^4$ times) ⁷⁵.

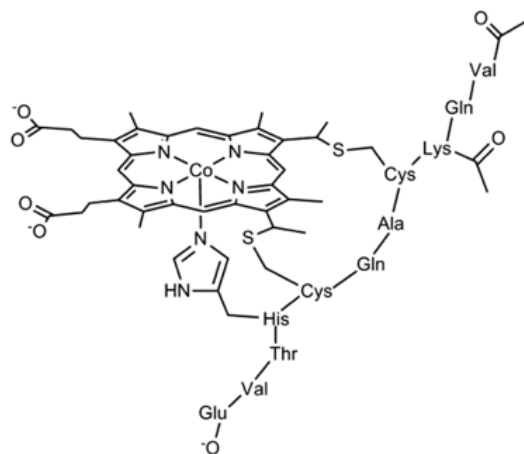


Figure (2.15). Schematic structure representation of Co^{III} -MP11. [*Reproduced from 'Ref. 75' with permission of the publisher*]

In 2016, the same group also reported another model system of the hydrogenase inspired catalysts, which exhibited enhanced catalytic activity for hydrogen evolution from water splitting. This bio-assembly catalyst was obtained by engineering the active site of the *Hydrogenobacter thermophilus* cytochrome c552 (Ht c-552) to obtain the mutant Ht-CoM61A, **Figure (2.16)**. This modified system of Ht-CoM61A showed an overpotential value of 800 mV and a Faradaic efficiency of $92 \pm 8\%$, closer to that of MP11, but with higher turnover numbers $2.7 \cdot 10^5$ ⁷⁶.

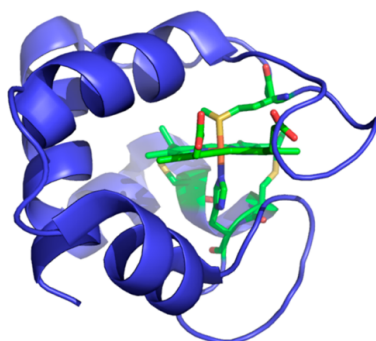


Figure (2.16). Structure of Cytochrome c552 (Ht c-552). [Reproduced from 'Ref. 76' with permission of the publisher]

In 2018, in a cooperative effort between the Lombardi and Bren groups, a cobalt variant of an artificial heme-peptide conjugate, was studied for HER. In particular, the so-called cobalt(III) mimochrome VI*a ($\text{Co}^{\text{III}}\text{MC6}^*a$), **Figure (2.17)**, composed of two peptide sequences incorporating a cobalt(III) deuteroporphyrin in a sandwich-like structure, was investigated. This small artificial system has proven catalytic activity and stability at physiological pH, it was capable of reducing protons at lower overpotential (by 100 mV lower) than $\text{Co}^{\text{III}}\text{-MP11}$ and higher TON (exceeding $2.3 \cdot 10^5$) in the presence of dioxygen ⁷⁷.

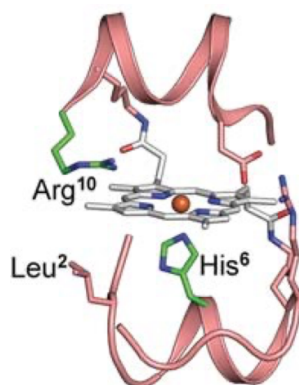


Figure (2.17). Chemical structure of $\text{Co}^{\text{III}}\text{MC6}^*a$. [Reproduced from 'Ref. 78' with permission of the publisher]

2.1.3. Insight on mimochromes as artificial enzymes

Mimochromes (MCs) are a class of heme-protein models, designed through a miniaturization strategy, as model of cytochromes and peroxidases ^{78,96}. Analyzing natural heme-protein structures, it emerges that the prosthetic group is almost completely embedded between two relatively small α -helical peptide fragments.

MCs are artificial heme-peptide conjugates, in which two small α -helix peptides are covalently linked to the 10 β -subunit of heme, giving rise to a sandwiched structure. The first analogue was patterned after the human-hemoglobin, **Figure (2.18)** ⁹⁷.

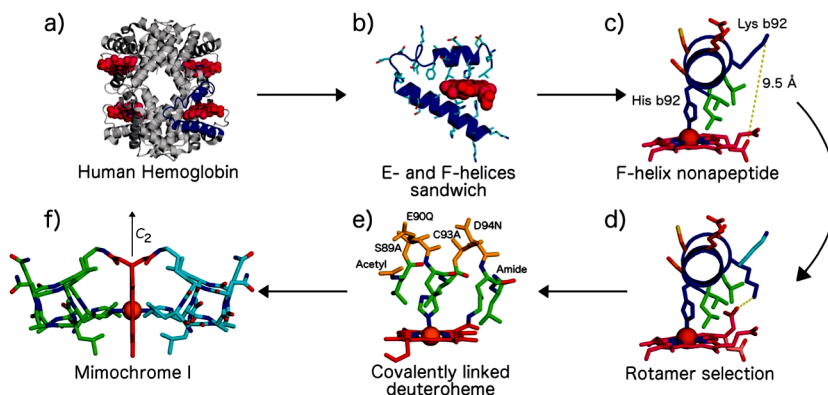


Figure (2.18). Miniaturization design steps from hemoglobin (PDB ID: 2hhb) to mimochrome I. Active site identification and extraction (**a and b**). Isolation of the nonapeptide covering the heme I. The mutual approach of heme propionate towards Lys92 by proper rotamer selection (**d**). Selection of solvent-exposed residues and protoporphyrin IX to deuteroporphyrin mutation I. Symmetrygenerated hexacoordinated deuteron-heme (**f**). [Reproduced from 'Ref. 97' with permission of the publisher]

Mimochrome I (*MCI*) peptide sequence contains: a central His residue to coordinate the heme iron; Leu residues at positions i-4 and i+4 relative to the His to hydrophobically interact with the heme macrocycle; a Lys residue to anchor the heme group; two Ala residues (that substitute Ser₃₉ and Cys₉₃ from natural hemoglobin), chosen for their high α -helical propensity; glutamine and asparagine residues (that substitute Glu₉₀ and Asp₉₄) to remove charge residues that could destabilize the target conformation^{98,99}, **Figure (2.19)**.

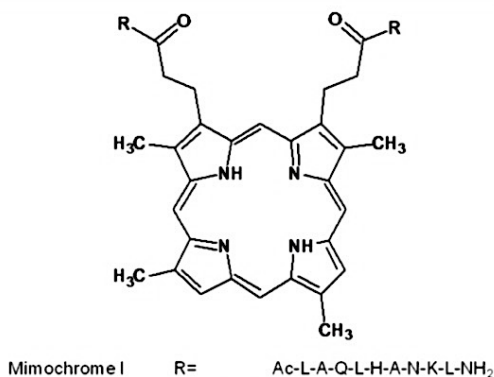


Figure (2.19). Chemical structure of the deuteroporphyrin prosthetic group of *MCI*, and its peptide sequence. [Reproduced from 'Ref. 99' with permission of the publisher]

Deuteroporphyrin IX was preferred to the more common protoporphyrin IX to avoid the possibility of degradation of the sensitive vinyl substituents during the synthesis. Two identical copies of the peptide were covalently linked to the porphyrin propionic groups through the ϵ -amino function of Lys, obtaining a *pseudo-C2*-symmetric dimer.

The insertion of cobalt ion into the porphyrin ring of *MCI* gave two diastereomers. In fact, linker flexibility between the peptide and the deuteroporphyrin ring allows each peptide chain to be positioned either above or below the porphyrin plane, producing enantiomeric configurations around the metal center. The presence of the substituents on the porphyrin ring and the chirality of the peptide chain

contribute to establish a diastereomeric correlation between the Δ and Λ isomers of $\text{Co}^{\text{III}}\text{MCl}$. This finding was confirmed by structural NMR characterization of the two previously separated cobalt(III) complexes, **Figure (2.20)**^{82,100}.

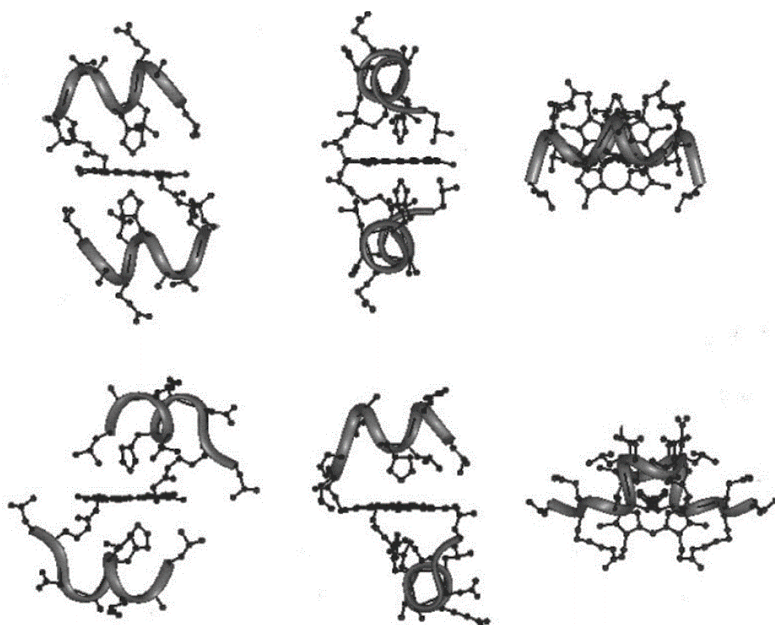


Figure (2.20). Front view (**Left**), side view (**Mid**), and top view (**Right**) of the average molecular structures obtained from NMR data and RMD calculations for Δ isomer (**Top**) and Λ isomer (**Bottom**) of $\text{Co}^{\text{III}}\text{MCl}$. [Reproduced from 'Ref. 82' with permission of the publisher]

The information derived from MCl was applied for improving the design. Over the years, quite a few other models were developed, with same or different peptide chains linked to the deuteroporphyrin ring¹⁰¹⁻¹⁰⁴, **Table 2.1**.

Table 2.1. Peptide sequences of various Mimochrome congeners.

Mimochrome		R1, R2
I	R ₁ = R ₂	Ac-L-A-Q-L- H -A-N- K -L-NH ₂
II	R ₁ = R ₂	Ac-D-L-S-D-L- H -S- K -L-K-I-T-L-NH ₂
IV	R ₁ = R ₂	Ac-E-S-Q-L- H -S-N- K -R-NH ₂
III, V	R ₁	Ac-D-E-H-K-L- H -S- K -R-K-I-T-L-NH ₂
	R ₂	Ac-D-E-H-K-L- Y -S- K -R-K-I-T-L-NH ₂
VI	R ₁	Ac-D-E-Q-Q-L- H -S-Q- K -R-K-I-T-L-NH ₂
	R ₂	Ac-D-E-Q-Q-L-S-S-Q- K -R-NH ₂
VI*a	R ₁	Ac-D-L-Q-Q-L- H -S-Q- K -R-K-I-T-L-NH ₂
	R ₂	Ac-D-E- U -Q-L-S- U -Q- K -R-NH ₂

H = His coordinating the metal center; **Y** = Gly or Ser;
K = Lys bound to deuteroporphyrin; **U** = Aib (Isobutyric acid)

Among the *Mimochrome* family, *MC6* was the first model showing catalytic potential. *MC6* was composed of two asymmetrical α -helices peptide sequences that differ in the chain-length. One of these peptide sequences was a tetradecapeptide (TD) with His₆ in the center available to coordinating the metal cofactor as axial ligand (proximal site), and the other is a decapeptide (D) lacking any coordinative residues, thus providing a vacant site acting as active cavity for catalysis (distal site).

The tertiary-structure of metal-inserted *MC6* was intended to be close to *MC1*, **Figure (2.21)** ^{105,106}.

The main structural features of *MC6* are:

- (i) The tetradecapeptide adopts a small helical conformation (residues 1-9), a loop $\gamma\beta$ D (residues 10 and 11), and a short β -strand (residues 12-14) that folded back to interact with the helical part.
- (ii) The decapeptide chain adopts a helical conformation (residues 1-8).

- (iii) The stabilization of the secondary structure occurs through dipole interaction (the positively charged Arg10 and negatively charged Glu2) of the terminal sides (C- and N-terminal ends) of both helices.
- (iv) The stability of the tertiary-structure is enhanced through inter-chain ion pairs between the carboxylate side chains of a glutamate residue (Glu2) on one helix and the guanidine group of an arginine residue (Arg10) on the other helix; further, coordination between the His6 and the metal keeps the sandwich-like structure.
- (v) Several glutamines (Gln3, Gln4, and Gln8) and a serine (Ser7) are present in the solvent-exposed positions to promote water solubility.

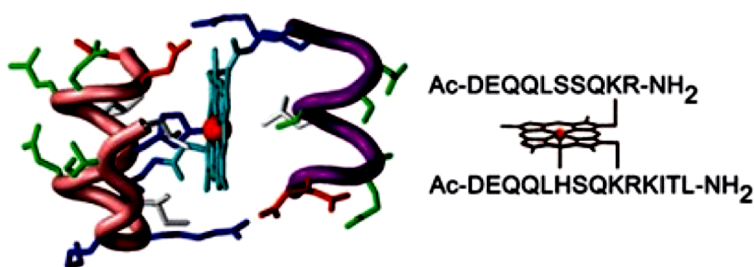


Figure (2.21). Model structure of Fe^{III}MC6 and its amino acid sequence. [Reproduced from 'Ref. 105' with permission of the publisher]

Further efforts were devoted in developing a set of MC6 mutant by screening few key positions, which resulted in the so-called mimochrome VI*a (MC6*a), previously reported in **Figure (2.17)**.

The structural features of the newly design MC6*a, **Figure (2.17)**; **Table 2.1**, are:

- (i) E²L(TD) mutation, in which a leucine replaced the glutamic acid in the position 2 of the tetradecapeptide; this mutation supported the enhancement in the peroxidase-like catalytic activity. This suggested that E²L mutation

allowed the free arginine residue on the D chain (R¹⁰(D)) to be involved into catalysis, by stabilizing the active intermediate.

- (ii) Q³U(D) and S⁷U(D) mutations, in which both glutamine and serine in positions 3 and 7, respectively, were replaced by isobutyric acid (Aib, U), which is well-known for its helical propensity. Moreover, according to NMR data, Aib-residues positioned toward the heme-motif, hence providing the hydrophobicity environment for substrate binding.

The enhanced peroxidase-like catalytic activity of Fe^{III}*MC6*a* consisted in a turnover frequency (k_{cat}) value 2.5-times higher than previous miniaturized proteins, together with higher turnover number ¹⁰⁶.

On the other hand, the cobalt complex of *MC6*a* showed a catalytic activity for electrochemical hydrogen evolution from water splitting, as previously mentioned, in **section (2.1.2, p. 102)** ⁷⁷.

2.2. Aims (chapter 2)

In this context, $\text{Co}^{\text{III}}\text{MC6}^*a$ has shown a robust hydrogenase-like enzymatic activity for electrochemical hydrogen production from water splitting, as previously reported in **section (2.1.2; p. 102)**. However, its overpotential is still a significant limitation to overcome in order to implement such catalyst for hydrogen economy. The development of a photosensitized system for $\text{Co}^{\text{III}}\text{MC6}^*a$, either by multicomponent or binuclear-conjugated assembly, will eventually support in exploiting the free-source of energy from sun.

On the other hand, the previously described Ru^{II} -complex, **3, Chapter (1)**, showed encouraging features such as the simple synthetic route, versatile conjugation/functionalization, and the lack of a stereogenic center. Moreover, complex **3** showed promising photophysical and photochemical properties; as in the case of the previously reported photo-induced charge transfer process towards Cc heme *c* cofactor.

Herein, we report and discuss the generation of a conjugated assembly between **3** and $\text{Co}^{\text{III}}\text{MC6}^*a$, as the photosensitizer and the HER catalyst, respectively. Moreover, we will show the results obtained in the photosynthesis of hydrogen from both the freely-diffusing and the covalent assembly.

2.3. Result and Discussion

2.3.1. Synthesis the prototype bi-metallic assemblies of **3** and $\text{Co}^{\text{III}}\text{MC6}^*a$

In bioinorganic chemistry, different methods have been adopted to functionalize metalloproteins with ruthenium photosensitizers, **see chapter (1)**, generally involving mutation or modification of protein surface residues at specific positions. However, in the context of designing a bimetallic-nuclear assembly of a miniaturized enzyme, like mimochromes (e.g. $\text{Co}^{\text{III}}\text{MC6}^*a$), some challenges must be considered. The presence of a partially exposed metal cofactor with a catalytically proficient coordination position (like cobalt-porphyrin) and the presence of unprotected (chemically or by the surrounding protein matrix) active residues on the peptide scaffold (e.g., Asp (D), Glu (I), and Lys (K)) poses serious issues in the functionalization protocol. Besides, few parameters should be considered regarding the photosensitization and the photo-induced charge transfer, such as: (i) the PET pathway (e.g., ionization cascade or tunneling), (ii) mutual position, distance, and orientation of the active metal sites. Therefore, not only the conjugation method, but also the choice of the linker length and its chemical features result to be critical for the catalytic activity.

As a starting point, the most logical choice is to tackle this coupling targeting the only free amine moiety of Lys_{11} ($\text{K}^{\text{11}}(\text{TD})$) side chain from the TD-peptide sequence of the MC's scaffold. The previously reported structural characterization of MC6^*a has shown that $\text{K}^{\text{11}}(\text{TD})$ residue is located at the exterior of the MC's scaffold, which makes it easy to be attached to the carboxyl moiety of the Ru^{II} -complex (**3**).

In this respect, we proceeded in such conjugation by synthesizing two prototypical assemblies between **3** and $\text{Co}^{\text{III}}\text{MC6}^*a$: (i) by using a crosslinker (spacer) between **3** and $\text{K}^{\text{I}}(\text{TD})$ (ii) with direct attachment of **3** to $\text{K}^{\text{I}}(\text{TD})$, **Figure (2.22)**.

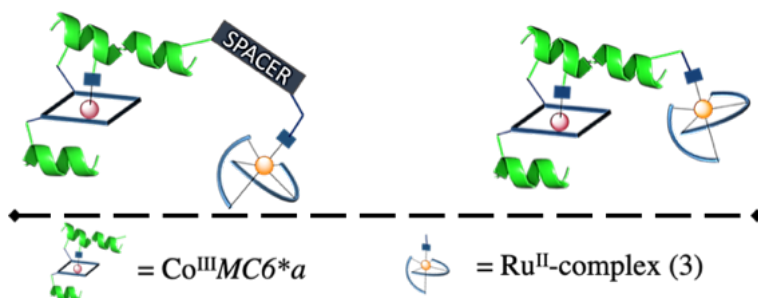


Figure (2.22). Schematic representation of the two proposed prototypical assemblies between **3** and $\text{Co}^{\text{III}}\text{MC6}^*a$: spaced conjugation assembly (**Left**), direct conjugation assembly (**Right**).

2.3.1.1. Synthesis and characterization the 1st prototype conjugate ($3\text{-[DBCO-PEG}_4\text{]Co}^{\text{III}}\text{MC6}^*a$)

The synthesis of the distal-assembly between **3** and MC6^*a was adopted by an azide-derivative of the ruthenium complex **3** and using the DBCO-PEG₄-NHS (**DBCO-PEG₄**) crosslinker, **Figure (2.23)**, as a spacer between the ruthenium-complex and the mimochrome.

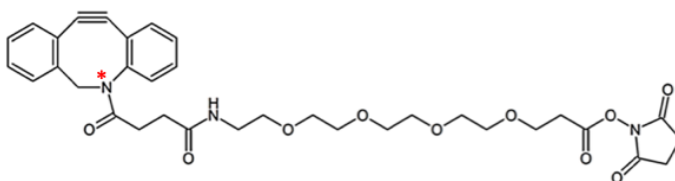
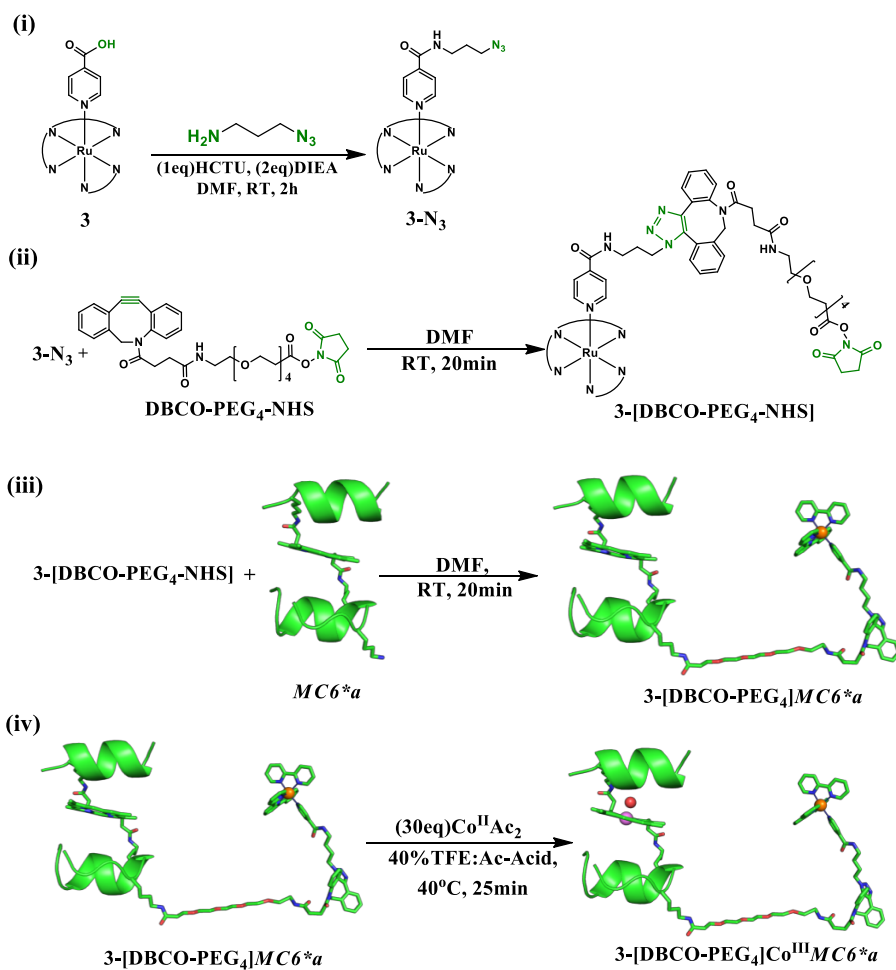


Figure (2.23). The structural formula of DBCO-PEG₄-NHS ester.

The azide-moiety and **DBCO-PEG₄** were chosen because fast and quantitative conjugation could be afforded through copper-free strain-promoted azide–alkyne cycloaddition (**SPAAC**) reaction¹⁰⁷, a widely adopted bio-orthogonal method for

the functionalization of biological molecules. Moreover, spacer length may be tuned to control the distance between the two cofactors. **DBCO-PEG₄** provides two orthogonal active moieties, which can be opportunely and selectively linked (the **NHS** moiety on the one side and the acetylene moiety on the other). The synthesis of the distal assembly was carried out by four steps of preparation/purification, **Scheme (2.4)**.



Scheme (2.4)

The stability of **3** was firstly tested under the harsh conditions of cobalt insertion. 50 equivalents of the cobalt(II)acetate were added to a solution of **3** in acetic acid/TFE (60:40) solvent. RP-HPLC is used to monitor any changes occurring during reaction progress.

The HPLC profile, **Figure (2.24)**, taken after 3h, shows no significant difference from the starting chromatogram; only one peak is observed at 15 min corresponding to the ruthenium-complex **3**. UV-Vis spectra of the eluted peaks are superimposable confirming that no degradation or change in its coordination sphere occurred. The stability of **3**, under the experimental conditions of cobalt-insertion, guarantees that metal insertion can be the last step in MC photosensitization without modification of the conjugated complex.

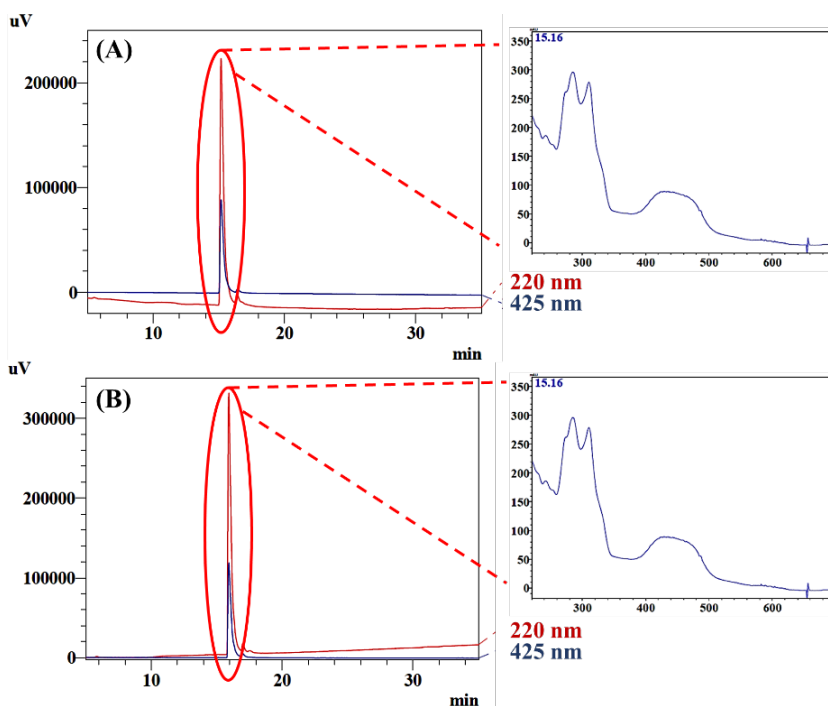
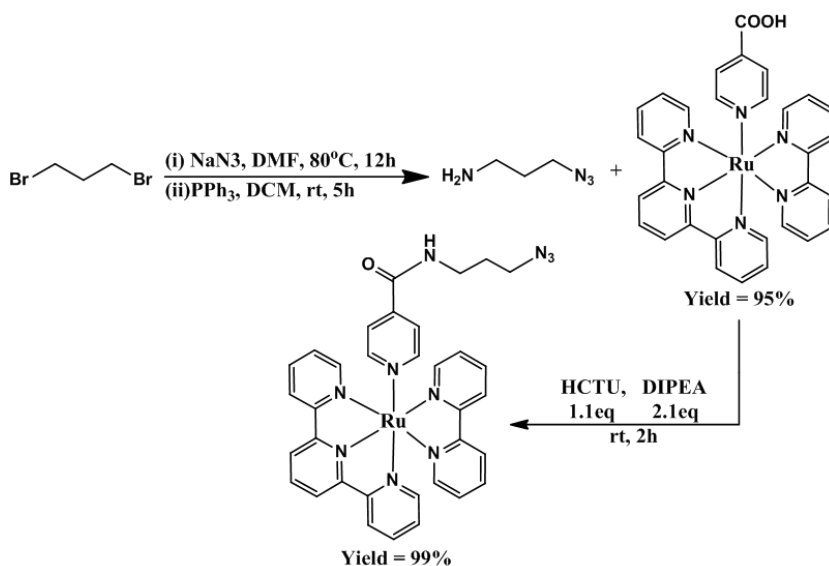


Figure (2.24). RP-HPLC profiles of **3** in the presence of cobalt acetate (50eq) in 40% TFE glacial acetic acid at 37°C, before (A) and after 3h (B). [Insert: on-line UV-Vis spectra of the eluted peak].

Step (i) consisted in the synthesis of the azide-derivative of the ruthenium complex (**3-N₃**). The ruthenium complex was reacted with 3-azido-1-propanamine ($\text{NH}_2\text{C}_3\text{H}_6\text{N}_3$) (**APA**), **Scheme (2.5)**. The **APA** was synthesized by a modified procedure that was reported in the literature¹⁰⁸. The azide derivatized-ruthenium complex (**3-N₃**) was obtained through acylation reaction between the carboxyl group of **3** with the amine moiety of the **APA** (1eq), in the presence of HCTU (1.1eq) and DIPEA (2.2eq).



Scheme (2.5)

The **3-N₃** derivatized complex formation reaction was monitored by HPLC, **Figure (2.25)**, which showed the decreasing in the peak corresponding to **3** ($R_t = 12.2$ min) and the increasing of the derivatized complex at later retention time ($R_t = 17.1$ min). The peak at 13.9 min corresponds to $[\text{Ru}^{\text{II}}(\text{bpy})_3]$, used as internal standard. Reaction progress could be followed by plotting the normalized area of the peak at 17.1 min versus time. Almost complete conversion (>97%) could be observed within 3h.

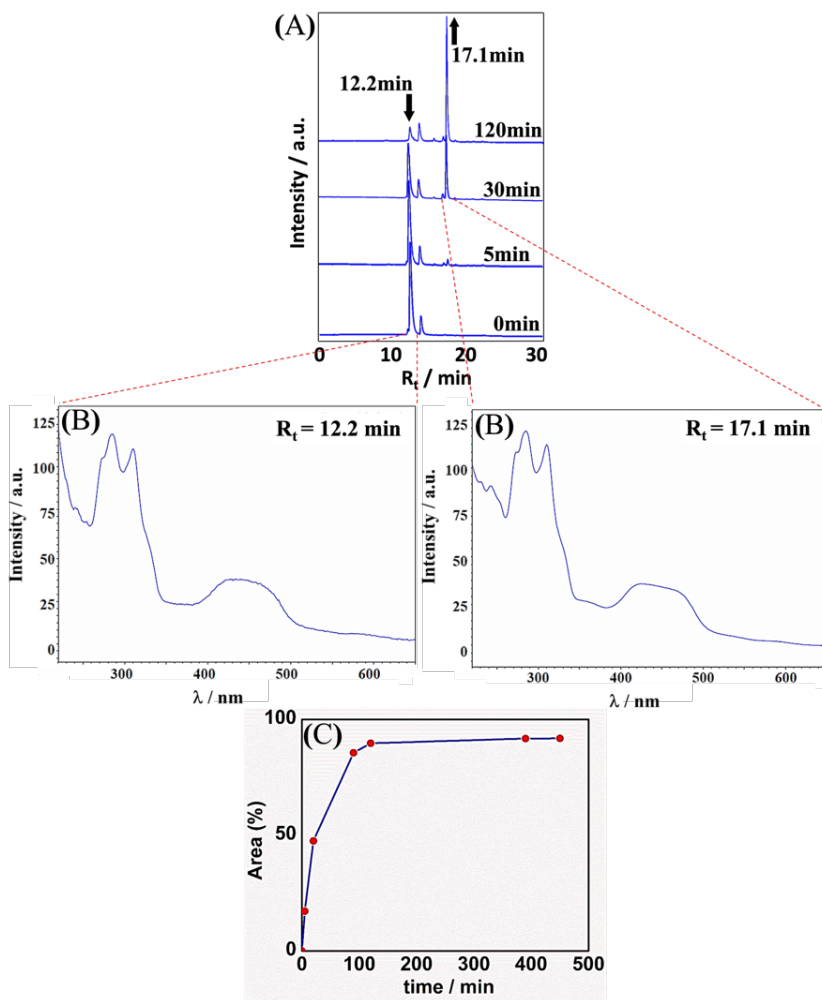


Figure (2.25). RP-HPLC reaction monitoring for the formation of 3-N_3 (PDA wavelength 425 nm). (A) The HPLC profiles were conducted by serial injection of $15\ \mu\text{L}$ of the reaction aliquots (1 mM) diluted with water and abstained at a different time (0, 5, 30, 120 min). (B) The UV-Vis spectra related to the chromatographic peaks. (C) The reaction proceeding plots (peaks intensity vs. time).

The RP-LC was also used to purify 3-N_3 . The HPLC profile of the purified product, **Figure (2.26, A)** showed a peak at 17.0 min (corresponding to the 3-N_3) with purity exceeding 99%. Product identity has been further confirmed by high

resolution MS analysis. Mass spectrum of the synthesized **3-N₃**, **Figure (2.26, B)** shows m/z values at 348.082 ($[M]^{2+}$) 809.156 ($[M^{2+}\cdot TFA^{-}]^{+}$), and 945.131 ($[M^{2+}\cdot 2TFA\cdot Na^{+}]^{+}$) that are consistent with the theoretical mass 696.163 Da. Other peaks are also observed at m/z value of 245.5333 and 604.056, which derived from in-source fragmentation of the complex losing the azido-functionalized monodentate ligand.

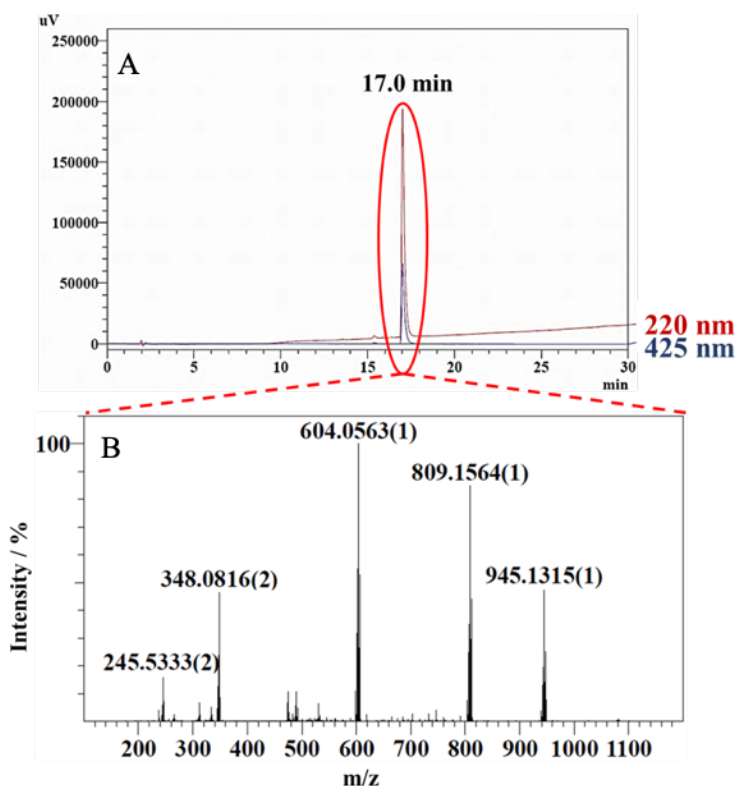


Figure (2.26). RP-HPLC of the flash-chromatographic purified sample (**3-N₃**) (A). IT TOF(MS) spectrum of the **3-N₃** dissolved into Acetonitrile (I) solvent (B).

The NMR analysis, **Figure (2.27)**; **Table 2.2**, confirms the covalent linkage between pyCOOH ligand and N₃-propyl moiety.

Table 2.2. complex 3-N₃ assignment

Complex (3-N ₃)	1H-NMR chemical shift values							
bpy	b2	b1	b3	b2'	b3'	b4	b4'	b1'
	7.06(t)	7.24(d)	7.81(t)	7.82(t)	8.28(t)	8.38(d)	8.64(d)	8.66(d)
tpy	t2, t2'	t1, t1'	t3, t3'	t2''	t4, t4'	t1'', t3''		
	7.39(t)	7.77(d)	8.01(t)	8.19(t)	8.41(d)	8.51(d)		
py	p2, p6	p3, p5	NH	a2	a3	a1		
	7.52(d)	7.79(d)	7.89	1.73(q)	3.32(t)	3.34(t)		

In general, the ¹H-NMR spectrum is characterized by the presence of two set of resonances: one set is in the down field region (7.0-8.8 ppm) and the other one is in the spectral region 1.7-3.4 ppm.

The first set of resonances (7.0-8.8 ppm) was attributed to the aromatic protons of the py-ligands and the three resonances in the high field region of the spectrum (1.73, 3.32, and 3.34 ppm) were assigned to the propyl-protons of the azide-moiety, aliphatic protons, assigned as: a2, a3, and a1, respectively.

Interestingly, the aromatic region of the NMR spectrum has similar features to those of the complex **2**. This region is characterized by no change in the position of the bpy and tpy aromatic proton peaks compared to their positions in the complex **2**, while the H_{p3,p5} of the pyCOOH functionalized ligand are downfield shifted (from 7.61 ppm in **2** to 7.79 ppm in **3**). It is reasonable to assume that this downfield shift could be due to the amide-bond between pyCOOH ligand and azide-moiety.

Furthermore, a careful analysis of this region highlights the presence of a broad-signal at 7.89 ppm, that was unequivocally assigned to the amide proton. This

corroborates that pyCOOH functionalization occurs through amide (CO–NH) linkage.

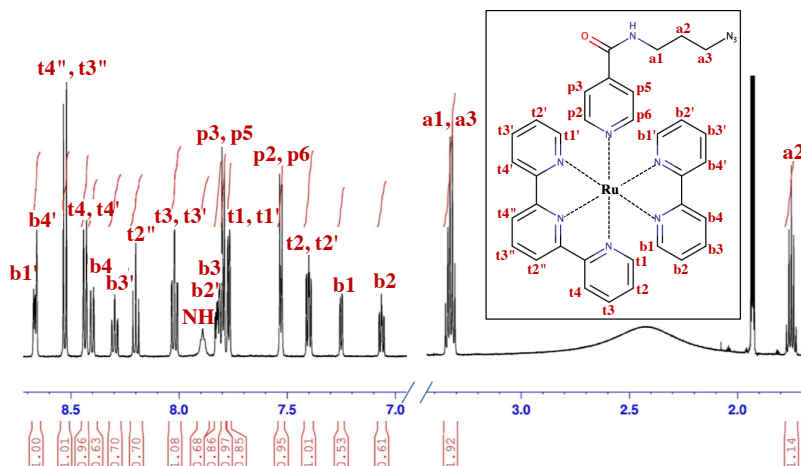


Figure (2.27). $^1\text{H-NMR}$ spectrum of the $\mathbf{3-N_3}$ (10mM) in CD_3CN .

Step (ii) consisted in the functionalization of $\mathbf{3-N_3}$ through SPAAC reaction, forming the triazole moiety on the DBCO-spacer in DMF. The HPLC profile, **Figure (2.28)**, shows that the reaction proceeded almost quantitatively (93%) after 20 min. The formation of the $\mathbf{3-[DBCO-PEG_4-NHS]}$ was followed by the peak eluting at 24.0 min. UV-Vis-spectra confirmed that the observed chromatographic peaks corresponded to $\mathbf{3-N_3}$ and the $\mathbf{3}$ -crosslinker.

No purification was required, and in order to save the active NHS ester from hydrolysis, it was directly used for the next coupling step.

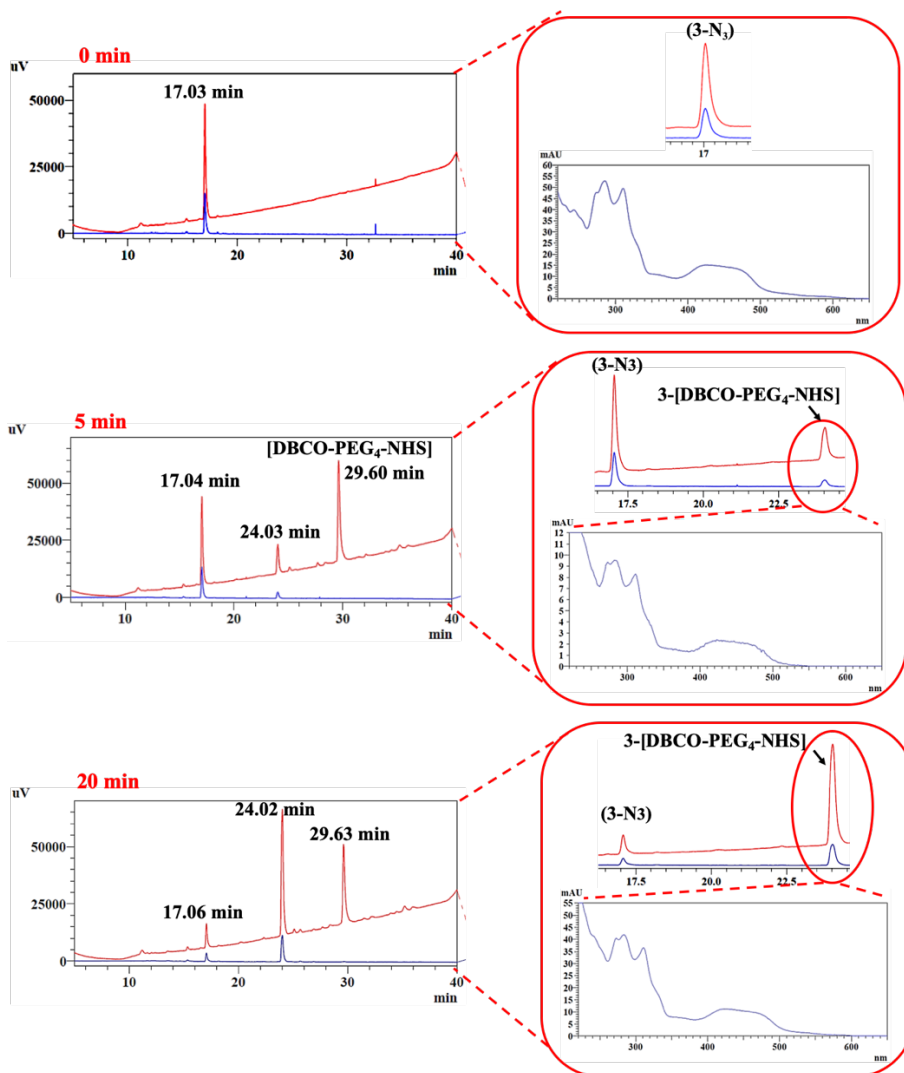


Figure (2.28). RP-HPLC and UV-Vis analyses of **step ii**. Crude was injected at 0, 5 and 20min.

*MC6*a* free base could be also functionalized prior to SPAAC reaction with 3- N_3 , however unpredictable hydrolysis of the amide bond in the DBCO-PEG₄-linker occurred and verified via HPLC, see **supporting information (S13)**. Hydrolysis increased after the purification under acidic conditions.

Step (iii) consisted in the coupling reaction between the previously linked species and $MC6^*a$ to form $3\text{-[DBCO-PEG}_4\text{]}MC6^*a$. The reaction was carried out by adding a solution of 1 eq of $MC6^*a$ and 12 eq of DIPEA in DMF to the previously obtained solution. The HPLC analysis, **Figure (2.29)** showed the successful coupling with 99% yield within 20 min ($R_t = 29.2$ min). The UV-Vis spectrum of the $3\text{-[DBCO-PEG}_4\text{]}MC6^*a$ conjugate showed all the bands corresponding to $MC6^*a$ (the *Soret* and *Q*-bands) and to the Ru^{II} -complex (MLCT and LC).

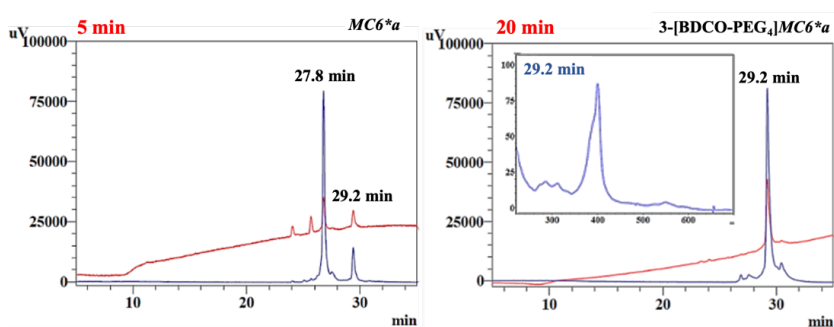


Figure (2.29). RP-HPLC profiles for monitoring the **step iii** of the synthetic approach (Coupling between DBCO-functionalized $3N_3$ and $MC6^*a$) after 5 and 20 min of reaction progress. [Insert: on-line UV-Vis spectrum of the peak at $R_t = 29.2$ min, corresponding to coupled-conjugate].

Finally, cobalt was inserted to obtain the desired binuclear assembly (**Step iv**). Similarly, the previously synthesized direct assembly, the HPLC peak of the final product shifted to earlier retention time within 25 min, **Figure (2.30)**. Again, the broadening of chromatographic peaks due to the cobalt was also observed. A UV-Vis spectrum was registered, which was very similar to the previously synthesized direct assembly.

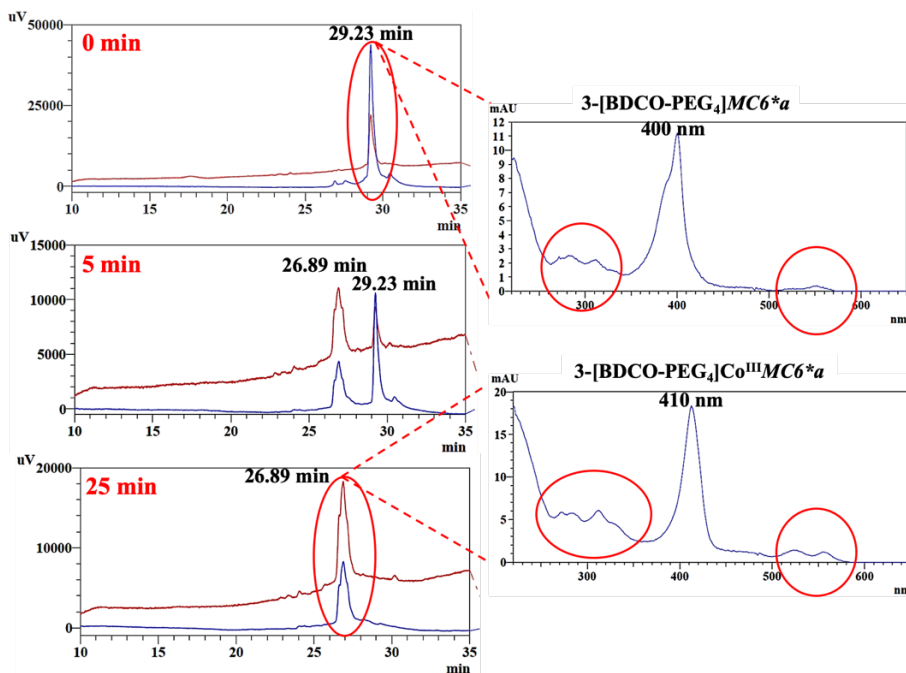


Figure (2.30). RP-HPLC profiles (**Left**) and on-line UV-Vis spectra (**Right**) for monitoring the **step iv** of the synthetic approach (Cobalt-insertion into 3-[DBCO-PEG₄]MC₆*a assembly) after 0, 5 and 25 min.

The HPLC profile of the purified 3-[DBCO-PEG₄]MC₆*a and 3-[DBCO-PEG₄]Co^{III}MC₆*a assemblies, **Figure (2.31)** show >97% pure, and the calculated yield was approximately 98%. The IT-TOF(MS) spectrum of 3-[DBCO-PEG₄]MC₆*a confirms the product identity, **Figure (2.31, A)**. Peak clusters centered around m/z values of 1167.320 ($[M^{2+}+2H]^{4+}$) and 934.261 ($[M^{2+}+3H]^{5+}$) are consistent with the theoretical 3-[DBCO-PEG₄]MC₆*a mass of 4666.254 Da (calc. mass 4666.321). Moreover, the IT-TOF(MS) spectrum of 3-[DBCO-PEG₄]MC₆*a confirms the product identity, **Figure (2.31, B)**. Peak clusters centered around m/z values of 1575.40 ($[M+3H]^{3+}$) and 1181.55 ($[M+3H]^{4+}$), 945.64 ($[M+5H]^{5+}$), and 787.87 ($[M+4H]^{6+}$) are consistent with the theoretical 3-[DBCO-PEG₄]Co^{III}MC₆*a mass of 4723.22 Da (calc. mass 4723.12 Da).

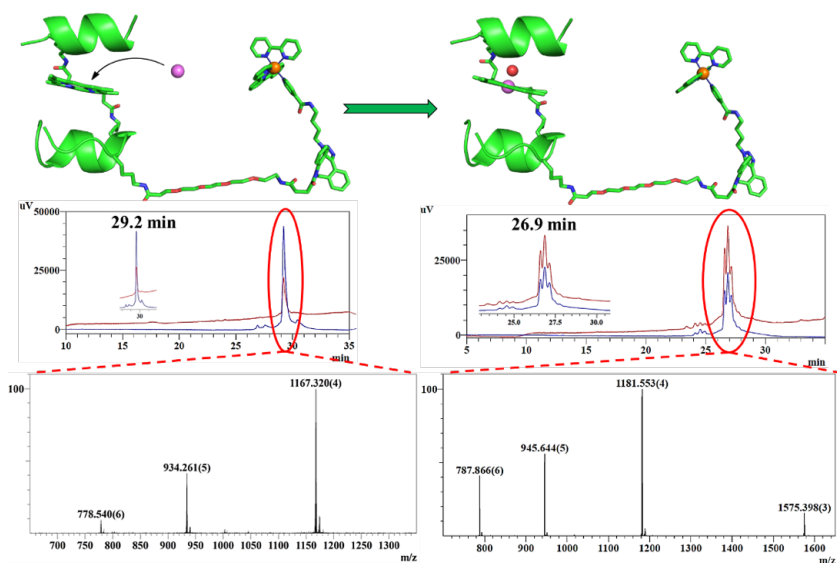


Figure (2.31). Schematic image of the **3**-[DBCO-PEG₄]*MC6*a* and **3**-[DBCO-PEG₄]*Co^{III}MC6*a* assemblies and the corresponding RP-HPLC profiles for the pure products, injected samples prepared in (0.1%TFA: H₂O) (**Top**) and related mass-spectra obtained from the high-resolution IT-TOF(MS) of the marked chromatographic peaks. (**Bottom**).

2.3.1.2. Photo-induced hydrogen evolution by *Co^{III}MC6*a* using **3** and [Ru^{II}(bpy)₃] as photocatalysts

*Co^{III}MC6*a* was tested towards photocatalytic H₂ generation in a well-established assay, consisting of ascorbic acid as the sacrificial donor, and either **3** or [Ru^{II}(bpy)₃] as photosensitizers ¹⁰⁹. The covalent conjugate, **3**-[DBCO-PEG₄]*MC6*a*, was also evaluated under the same conditions. The ascorbic acid/Ru^{II}(bpy)₃ experimental setup has been widely adopted for photocatalytic hydrogen (H₂) generation in the literature ^{110,111}. In particular, Bren and coworkers adopted the same approach to test the photocatalytic activity of cobalt-microperoxidase 11 (CoMP11-Ac)₃, and, more recently, of a small peptide-based

complex, in which cobalt(III) is surrounded by a Gly-Gly-His ligand (CoGGH)
109

Initially, in order to assess the viability of complex **3** as a photosensitizer to Co^{III}-cofactor in Co^{III}MC6*a in comparison with [Ru^{II}(bpy)₃], an excess of both photosensitizers was utilized. Photochemical experiments were performed with Bis-Tris Propane (pK_a 6.9), a bulky buffer that is mostly protonated at pH 6.5, **Figure (2.32)**. While piperazine buffer promoted high performance⁷⁷, it was early avoided in case of unexpected coordination to **3**. The system in which [Ru^{II}(bpy)₃] performs the photo-induced reduction of Co^{III}MC6*a showed appreciable photocatalytic activity in H₂ production, six times less than the background, in which only [Ru^{II}(bpy)₃] was present in solution. However, no H₂ was produced in the presence of excess of **3**. This result indicates that complex **3** is not functioning as a viable photosensitizer for this system under these conditions.

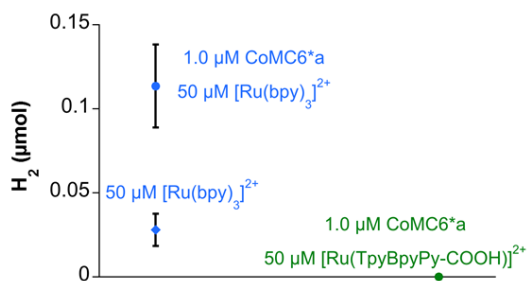


Figure (2.32). Photochemical experiments with excess (50 μM) **3** or [Ru^{II}(bpy)₃]. The experiments were performed with 100 mM ascorbic acid, 1.0 M Bis-Tris Propane (pH 6.5), and blue LEDs (0.15 W, 448 nm). The samples were run in triplicate and collected after 48 hours with standard deviation bars shown in the plot (n = 3). The controls run not containing catalyst are depicted as diamonds (n = 2).

In order to move to the more efficient piperazine buffer, a stability test was then conducted by using both spectroscopic and chromatographic techniques. Two different solutions of complex **3** at 50 μM were prepared either in water or in a

piperazine buffer (1M, pH 7.0), and kept under the same conditions of light irradiation for 5h. The same HPLC profiles were observed for both samples with one intense peak around 13 min, without any further peaks observed (data not shown). Only slight quenching of the MLCT-band, due to the dissolved molecular oxygen, was observed in the piperazine buffer as preciously described. Any unexpected change in the ligand composition could be observed. For this reason, later experiments have been performed in piperazine buffer, to rule out the effect of the buffer.

Given the previous results for the freely diffusing systems, we speculated that the covalent **3**-[DBCO-PEG₄]*MC6*a* conjugate may afford the desired catalysis. In this case, a multicomponent system consisting of a 1:1 mixture of freely-diffusing [Ru^{II}bpy₃] and Co^{III}*MC6*a*, **Figure (2.33, Left)** was compared to the covalent-assembly system, **Figure (2.33, Right)**. Varying concentrations of the photosensitizer/catalyst were assayed (1, 10, 50 μM). The obtained results show that H₂ production almost linearly increased with concentration for the freely diffusing 1:1 system. In contrast, only negligible hydrogen production could be observed when **3**-[DBCO-PEG₄]*MC6*a* was used as photocatalyst.

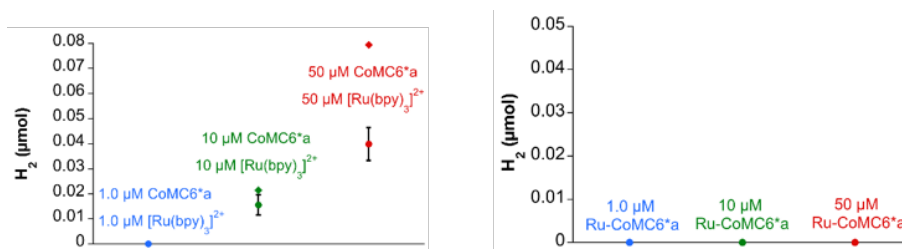


Figure (2.33). Photochemical experiments with 1:1 photosensitizer and catalyst at varying concentrations. 10 mM Ascorbic acid, 1.0 M piperazine (pH 6.5), and blue LEDs (0.15 W, 448 nm) were used. The samples were run in triplicate and collected after 48 hours with standard deviation bars shown in the plot (n = 3). Control runs containing the listed concentration of photosensitizer, 10 mM ascorbic acid, and no catalyst were also performed. The controls are depicted as diamonds (n = 1).

Further photochemical and electrochemical experiments were performed to evaluate the catalytic proficiency of **3**-[DBCO-PEG₄]Co^{III}MC6*a in hydrogen evolution in the presence of [Ru^{II}bpy₃] as the photosensitizer, to rule out any inhibition of the covalently modified catalyst. In principle, the presence of the linker or the proximity of the tethered **3** photosensitizers to Co^{III}MC6*a could inhibit catalysis.

3-[DBCO-PEG₄]Co^{III}MC6*a and the Co^{III}MC6*a produced the same amounts of H₂ in the presence of excess [Ru^{II}(bpy)₃], indicating that the catalytic activity of Co^{III}MC6*a was not hindered, **Figure (2.34)**.

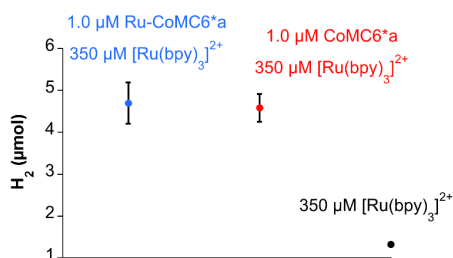


Figure (2.34). H₂ produced with 1.0 µM **3**-[DBCO-PEG₄]Co^{III}MC6*a (**Blue**) and 1.0 µM Co^{III}MC6*a (**Red**) in the presence of excess 350 µM [Ru^{II}(bpy)₃]. 10 mM ascorbic acid and 1.0 M piperazine buffer (pH 7.0) were used. Data were collected after 48 h of irradiation by blue LEDs (448 nm) at a power of 0.25 W and a temperature of 15°C. The samples that contained **3**-[DBCO-PEG₄]Co^{III}MC6*a or Co^{III}MC6*a were run in triplicate with standard deviation bars shown in the plot (n = 3). A control run (n = 1) without a catalyst is shown in black. The control was run under green LEDs (530 nm) due to the number of available blue LEDs at the time of the experiment. It is expected that some H₂ will also be made by [Ru^{II}(bpy)₃] under blue LEDs.

Cyclic voltammetry experiments were run to gauge potential differences between **3**-[DBCO-PEG₄]Co^{III}MC6*a and Co^{III}MC6*a. As demonstrated by the similar magnitude of the peak currents and shape of the cyclic voltammograms, the CV

indicated that the presence of the linker and the tethered the complex (**3**) did not alter either the activity or the overpotential of $\text{Co}^{\text{III}}\text{MC6}^*a$, **Figure (2.35)**.

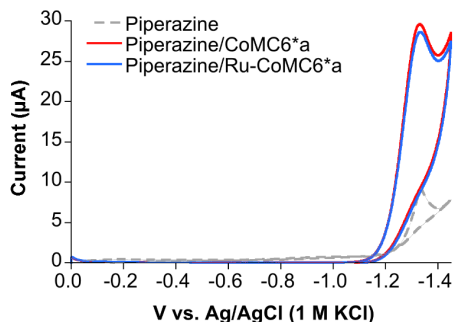


Figure (2.35). Cyclic voltammograms of $\text{Co}^{\text{III}}\text{MC6}^*a$ vs. **3**-[DBCO-PEG₄] $\text{Co}^{\text{III}}\text{MC6}^*a$. CVs were performed in the presence of 100 mM KCl, 25 mM piperazine (pH 6.5) at 100 mV/s scan rate. A hanging mercury drop working electrode, Ag/AgCl (1 M KCl) reference electrode, and a glassy carbon counter electrode were used. The plot displays third scan data.

Overall, our results indicate that the presence of the linker and of the Ru^{II} - complex does not hamper $\text{Co}^{\text{III}}\text{MC6}^*a$ catalyzed hydrogen production, finally demonstrating that **3** is unable to induce cobalt reduction under the tested experimental conditions.

Finally, the Stern-Volmer luminescence quenching studies were performed in order to evaluate whether the ascorbic acid (AscH) was indeed a good electron sacrificial reagent for both **3** and $[\text{Ru}^{\text{II}}(\text{bpy})_3]$. Luminescence quenching was evaluated using the Stern-Volmer equation, **equation (2.1)**:

$$\frac{I_0}{I} = K_{SV} [\text{AscH}] + 1; K_{SV} = k_q \tau_0 \quad (2.1)$$

The measurements were first performed for $[\text{Ru}^{\text{II}}(\text{bpy})_3]$ for comparison, **Figure (2.36, Left)**, and k_q and K_{SV} values were determined to be $1.0 \cdot 10^7 \text{ M}^{-1} \text{ s}^{-1}$ and 6.3 M^{-1} , respectively. The determined k_q (using the known τ_0 of 620 ns) is

comparable to that from literature for quenching of $[\text{Ru}^{\text{II}}(\text{bpy})_3]$ by ascorbic acid is $3.0 \cdot 10^7 \text{ M}^{-1} \cdot \text{s}^{-1}$ at pH 7.0¹¹².

For complex **3**, a K_{SV} value of 30 M^{-1} was determined from the Stern-Volmer plot, **Figure (2.36, Right)**. Excited state lifetime experiments are anyway needed in order to determine the k_q value for quenching of **3** by ascorbic acid. Overall, these data indicate that ascorbic acid quenches complex **3**, suggesting that the used sacrificial electron-donor should be suitable for catalysis.

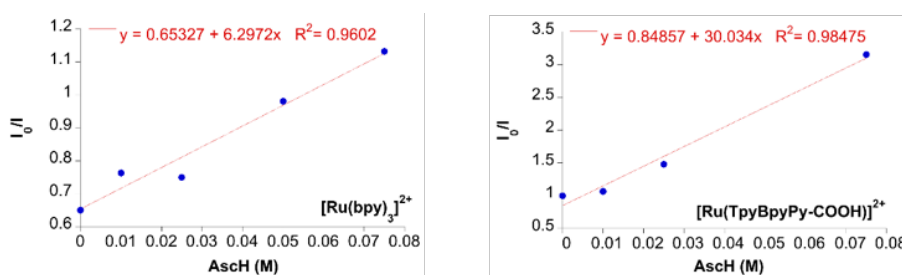


Figure (2.36). Stern-Volmer plots are showing I_0/I (initial luminescence intensity/quenched luminescence intensity) versus increasing concentration of quencher ascorbic acid, [Q]. The quenching of $[\text{Ru}^{\text{II}}(\text{bpy})_3]$ (**Left**) vs. **3** (**Right**) by ascorbic acid is demonstrated.

2.3.1.3. Synthesis and characterization the 2nd prototype conjugate (3-Co^{III}MC6*a)

In order to achieve the direct conjugation between **3** and $\text{Co}^{\text{III}}\text{MC6}^*a$, the carboxyl group of **3** should be activated by common activating agents (e.g., HCTU, DIC/NHS, EDC/NHS, etc.), which facilitate the condensation reaction to the amine-moiety of the K^{I} -residue. However, a one-step synthesis should be avoided, considering that acidic residues from the MC-scaffold could be also readily activated. Therefore, the generation and isolation of an active ester, such as the N-hydroxysuccinimide (NHS) ester, is highly recommended to prevent any undesired side reactions, **Figure (2.37)**. Ideally, the NHS-ester intermediate is

generally active yet sufficiently stable (under specific handled conditions) to be purified and then reused for the conjugation reaction with K^{11} -residue of the $MC6^*a$.

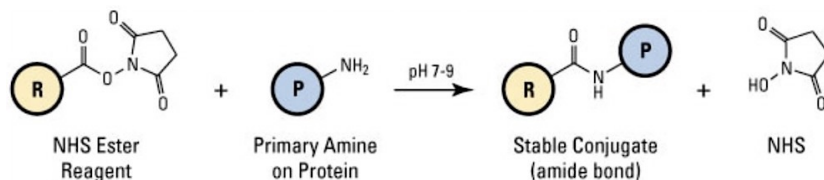


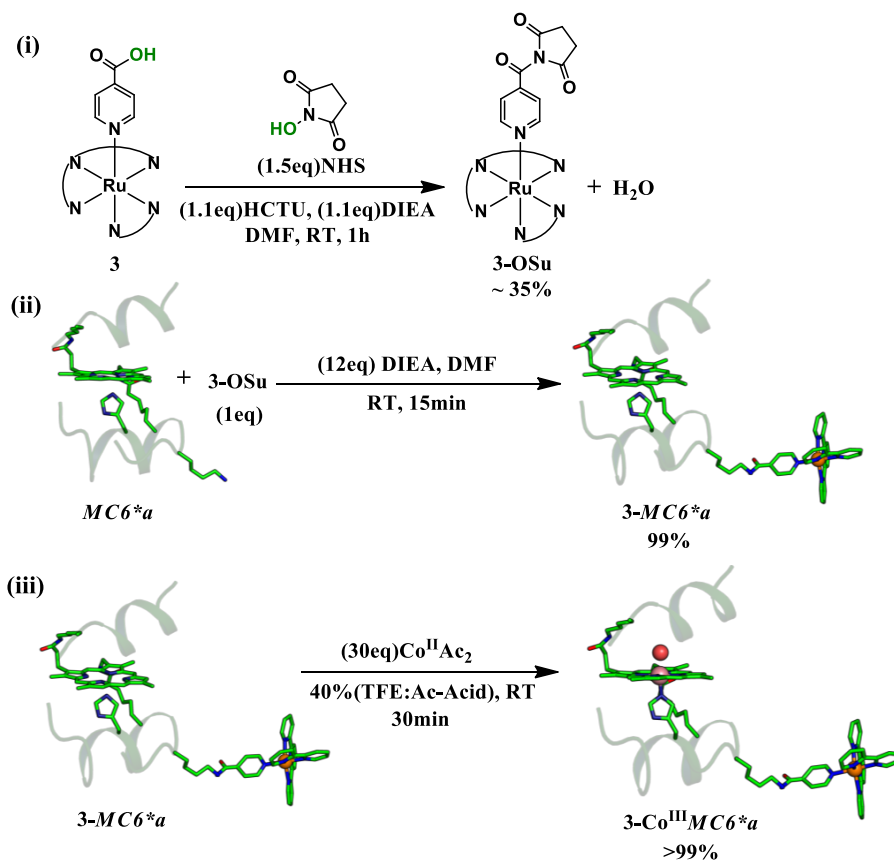
Figure (2.37). Conjugation reaction scheme between a generic primary amine of a protein/peptide and an activated NHS-ester.

The first attempts in the preparation of **3-Osu** derivatized complex were successfully carried out. Nevertheless, the lack of an effective purification procedure, preventing the hydrolysis of the previously formed **3-Osu** ester, hampered the successive coupling step.

In this respect, a modified protocol was adopted in order to achieve this conjugation by *in situ* addition of $MC6^*a$ free base to the readily formed **3-Osu** solution. The functionalization of $MC6^*a$ would then easily allow the insertion of any desired metal, thus generating a general photosensitizing framework for any MC metal complex. Moreover, as previously reported in the case of elder $Co^{III}MCl$ ¹⁰⁵, $Co^{III}MC6^*a$ is in slow-equilibrium among different stereoisomers, which causes technical complications during HPLC monitoring and purification steps.

The adopted conjugation strategy is illustrated in **Scheme (2.6)**. A one-pot stepwise reaction was carried out, first by forming the **3-Osu** activated intermediate, Step (i); **Scheme (2.6)**, by reacting **3** (10eq) with NHS (15eq), in the presence of 5eq of HCTU and DIPEA in “anhydrous-DMF” solvent. Successively, **3-Osu** has been reacted with Lys¹¹ sidechain of $MC6^*a$ (free-base), Step (ii); **Scheme (2.6)**, in a 1:1 molar ratio based on the HPLC yield, by

transferring a pre-prepared solution mixture of *MC6*a* in the presence of DIPEA in the **3-Osu** reaction mixture. After conjugated product purification, cobalt was inserted in the porphyrin of **3-MC6*a** by well-established protocols, Step (iii); **Scheme (2.6)**⁷⁷.



Scheme (2.6).

RP-HPLC profiles and on line UV-Vis spectra can be used to follow the reaction progress. After step (i), a peak at later retention time ($R_t = 16.2$ min) than **3** ($R_t = 14.1$ min) appeared, **Figure (2.38)**, corresponding to the **3-Osu** complex, which had UV-Vis spectrum similar to **3**. The estimated yield of **3-Osu** through peak integration was approximately 35%.

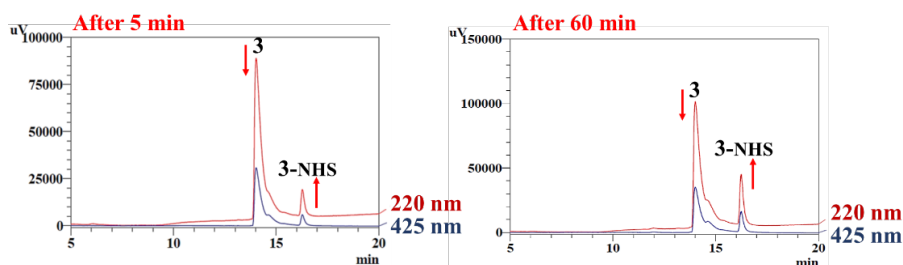


Figure (2.38). RP-HPLC profiles monitoring step (i). The formation of the **3-Osu** complex (R_t = 16.3 min) from **3** (R_t 14.1 min) can be appreciated from the registered chromatograms at 220 and 425 nm.

After step (ii), a new peak at R_t = 28.4 min appeared within 15 minutes, **Figure (2.39)**, corresponding to the desired conjugation product (**3-MC6*a**), whose UV-Vis spectrum showed both the bands of **3** (*MLCT* and *LC*) and *MC6*a* (*Soret* and *Q-bands*). The coupling was very fast (only 15 min) and without appreciable formation of any side products, thus confirming the reliability of our synthetic approach.

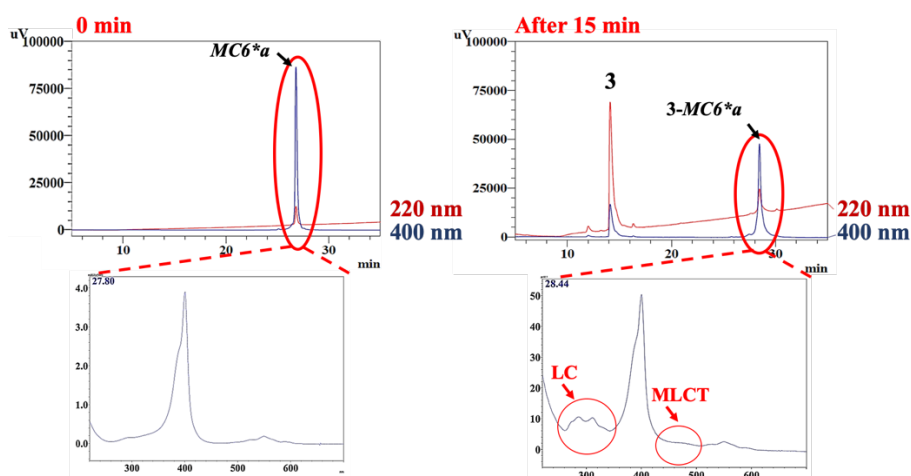


Figure (2.39). RP-HPLC profiles (**Top**) and on-line UV-Vis spectra (**Bottom**) monitoring step (ii). The formation of the **3-MC6*a** was confirmed by the UV-Vis spectra of the eluted peaks.

Finally, cobalt insertion in step (iii) was confirmed by the shift of **3-MC6*a** at earlier retention time ($R_t = 25.7$ min), corresponding to **3-Co^{III}MC6*a**, as previously reported upon metal insertion into the Mimochrome scaffold, **Figure (2.40)**⁸². The chromatographic peak broadening was also observed, due to the previously described formation of MC stereoisomers. The UV-Vis spectrum showed the expected bathochromic shift of the *Soret*-band (from 400 nm to 412 nm) and the multiplicity change of the *Q*-band (from four very broad peaks around 550 nm to two well-resolved peaks at 525 and 555 nm), in agreement with the formation of a six-coordinate cobalt porphyrin complex. Moreover, retention of the characteristic bands of the ruthenium complex excludes any undesired modification at the metal center under the adopted conditions.

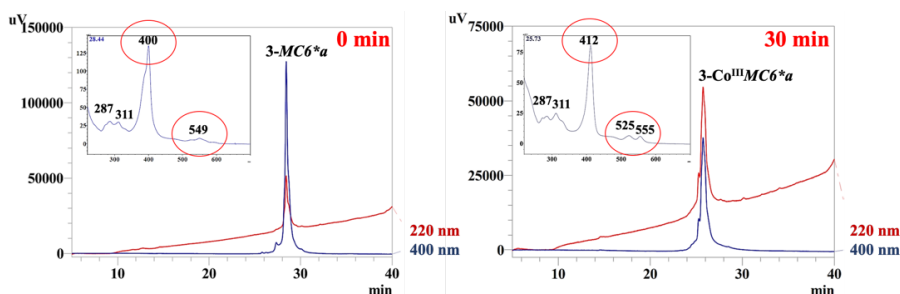


Figure (2.40). RP-HPLC profiles and on-line UV-Vis spectra (**Insert**) monitoring step (iii). The formation of the **3-Co^{III}MC6*a** was confirmed by the UV-Vis spectra of the eluted peaks.

The purification of **3-MC6*a** and **3-Co^{III}MC6*a**, after step (ii), firstly consisted in a precipitation step in diethyl ether to remove the excess of activating agents and organic reagents. A further purification step was performed by RP-LC, in order to isolate the final conjugate product from the Ru^{II}-complex excess. The percentage of recovery of **3** was 75%, and the product yield was close to 97%.

HPLC was then used to test the purity (>98%) of the fractions obtained from RP-LC purification, **Figure (2.41)**.

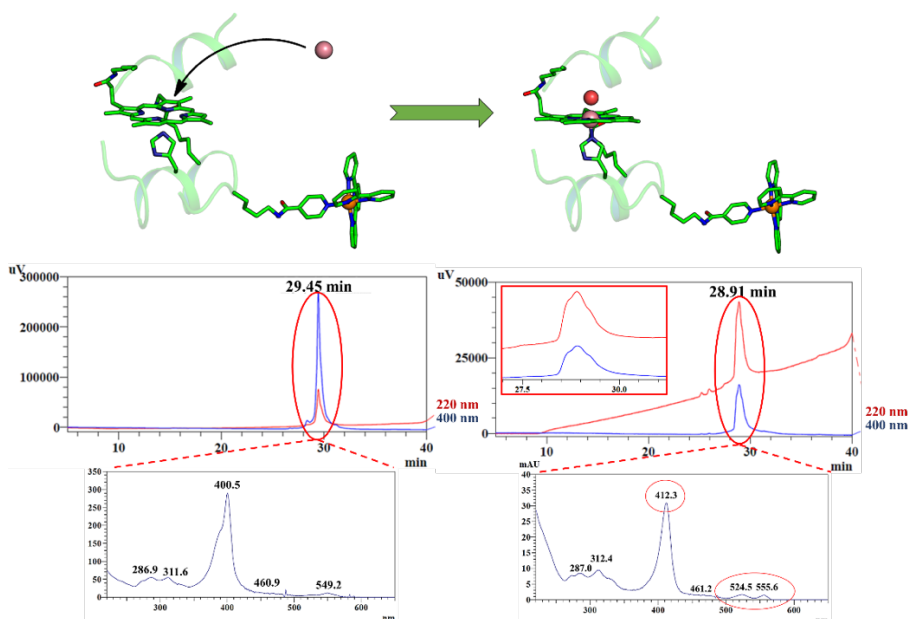


Figure (2.41). Schematic image of the **3-MC6*a** and **3-Co^{III}MC6*a** assemblies and the corresponding RP-HPLC profiles for the pure products, injected samples prepared in (0.1%TFA: H₂O) (**Top**) and on-line UV-Vis spectra of the marked peaks. (**Bottom**).

Product identity has been further confirmed by high resolution MS analysis. Mass spectrum of the synthesized **3-Co^{III}MC6*a**, **Figure (2.42)**, shows *m/z* values at 1363.631 ([M+1H]³⁺) 1022.975 ([M+2H]⁴⁺), and 818.581 ([M+3H]⁵⁺) that are consistent with the theoretical mass 4089.89 Da (calculated mass = 4089.82 Da).

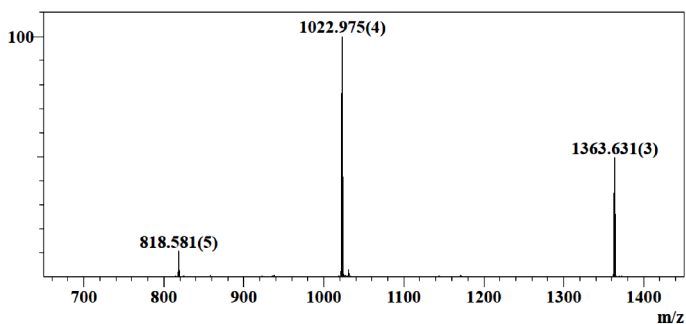


Figure (2.42). IT-TOF(MS) spectrum of **3-Co^{III}MC6*a**.

2.4. Concluding Remarks

In this chapter, we described our main results in the synthesis and characterization of two new photoactive adducts, obtained by crosslinking the newly synthesized complex **3** and $\text{Co}^{\text{III}}\text{MC6}^*a$ either through a long spacer (DBCO-PEG₄) or by direct conjugation. To this end, we developed a framework for MC6^*a photosensitization that, in principle, can be used for any given photosensitizing moiety. A combination of chromatography, UV-Vis spectroscopy and mass spectrometry have confirmed the validity of the here-described synthetic approaches.

In particular, the first one (**3**-[DBCO-PEG₄] $\text{Co}^{\text{III}}\text{MC6}^*a$) was obtained by SPAAC reaction between the azide-derivative, **3-N₃**, and dibenzocyclooctyne-labeled mimochrome. Photo-induced hydrogen evolution was then tested for both the freely diffusing system and the PEG₄-spaced binuclear assembly, and the result compared to the well-known $[\text{Ru}^{\text{II}}(\text{bpy})_3]$. The results indicate that **3** does not work as a photosensitizer under the conditions tested, but they do not indicate that the presence of the linker is inhibiting catalytic H₂ production by $\text{Co}^{\text{III}}\text{MC6}^*a$. Thus, the linker may still be suitable for a different ruthenium photosensitizer complex. In order to functionalize a Ru^{II} -complex with an azide for the “click reaction” with the DBCO linker, there are other Ru^{II} -based photosensitizers that are possible candidates containing the carboxylic acid moiety^{113,114}. It is possible that either the excited state lifetime or the energetics of **3** are not suitable to facilitate catalysis. Nonetheless, according to the photophysical and photochemical analysis presented in Chapter 1, we may speculate that the total thermodynamic driving force is too low for catalysis. As a matter of fact, $\text{Co}^{\text{III}}\text{MC6}^*a$ activity started at ~0.86V (vs SHE) as observed by CV experiments. Such value, perfectly match the redox potential of the $[\text{Ru}^{\text{II}}(\text{bpy})_3]$ excited state, whereas the redox potential of **3** was estimated around 0.66 V.

For the second direct assembly, we developed a tailored NHS-based conjugation protocol, consisting of a one-pot reaction that minimizes activating reagent consumption, resulting in minimal side-reaction products. Such binuclear adduct is now being tested in Bren's lab, but at higher trifluoroethanol (TFE) concentrations as it has been shown that proton reduction overpotential was reduced when $\text{Co}^{\text{III}}\text{MC6}^*a$ was in presence of TFE.

2.5. Materials and Methods

2.5.1. Materials, reagents, and solvents

1,3-dibromopropane ($\text{BrC}_3\text{H}_6\text{Br}$), Sodium azide (NaN_3) and N,N-Diisopropylethylamine (DIPEA) were purchased from Sigma Aldrich and used as received. The coupling reagents, 2-(6-Chloro-1-H-benzotriazole-1-yl)-1,1,3,3-tetramethylaminium hexafluorophosphate (HCTU) and N-Hydroxysuccinimide (NHS), were purchased from Novabiochem. The solvents (absolute-ethanol, DMF) were HPLC-grade and purchased from Romil, the water used in synthesis was milli-Q water.

The solvents that used for purification and chromatographic analysis were HPLC-grade (Romil), while the solvents that were used for spectroscopic (UV-Vis and Fluorescence) analysis were in a high degree of purity (UPS-grade) from Romil. The HCl solvent used for atomic absorption spectroscopy (AAS) was ultra-pure and traced of metal.

2.5.2. Instrumentations and techniques

RP-HPLC chromatograms were acquired by a Shimadzu LC-10Advp equipped with an SPDMS10Avp diode-array detector system, using Vydac C18 column (150 mm x 4.6 mm; 5mm), eluted with linear gradient 10%A to 95%B (A: 0.1%TFA H₂O; B: 0.1%TFA CH₃CN) over 40 min, at 1mL.min⁻¹ flow rate.

The Purification of products was performed using flash chromatography from Biotage Isolera flash purification system, equipped with a diode-array detector. Biotage SNAP Ultra-C18 cartage (10 g; CV 15mL) was used in purification, the cartage were equilibrated using a recommended procedure by Biotage, LLC, and the running coarse with linear gradient of (10% - 95% 0.1% TFA acidified

acetonitrile/H₂O) for 20 CV in flow-rate 12 mL/min after dissolving the crude in concentrated solution of water.

The mass-spectra were performed using LCMS-IT-TOF from SHIMADZU, with a direct injection of 0.2 μL of the solution prepared in acetonitrile (100 μM).

The UV-vis absorption spectra were acquired by a Shimadzu UV-2401PC spectrophotometer, the spectra were recorded at wavelength range of 200–800 nm, scan rate of 200 nm.min⁻¹.

Electrochemical experiments were carried out with a 620D potentiostat (CH Instruments). Ag/AgCl (1 M KCl) and platinum wires were used as reference and counter electrodes, respectively.

The general procedure for cyclic voltammetry is as follows: 5 mL of 1 μM Co^{III}MC6a in 0.5 M KCl and 25 mM potassium phosphate buffer was used. Each measurement was repeated twice and a fresh mercury drop (surface area 0.038 cm²) was used for each experiment. Before start, the solution was purged 15 min with nitrogen. The measurements were performed under gentle nitrogen flow.

The photocatalytic activity of Co^{III}MC6a in hydrogen evolution reaction (HER) was characterized by using GC technique, in which aliquots of the reaction mixture was transferred to the GC cell before and after irradiating the samples, at the reaction condition mentioned before, for 48 h by blue LEDs (448 nm) at a power of 0.25 W and temperature of 15 °C. Before purging the aliquots, the GC cell was purged for 15 min with an N₂/CH₄ mixture (8/2), methane was used as the internal standard. Hydrogen (H₂) quantification was performed by GC analysis of cell headspace. The ratio between hydrogen and methane peak areas was compared with a standard calibration curve.

2.5.3. General Procedure

2.5.3.1. Synthesis the 1st prototype conjugate ((3-[DBCO-PEG₄]Co^{III}MC6*a)

Synthesis of the distal conjugate assembly was performed by reacting to the ruthenium complex **3** with free-base *MC6*a* through [DBCO-PEG₄]-crosslinker after derivatizing the complex **3** with pre-prepared 3-azido-1-propanamine, then followed by the cobalt insertion.

The preparation of 3-Azido-1-propanamine (N₃C₃H₆NH₂) was adopted by a modified synthetic approach that was reported in literature ¹⁰⁸, 1,3-diazidopropane (N₃C₃H₆N₃) was firstly prepared by di-substitution reaction of 1,3-dibromopropane (**BrC₃H₆Br**) precursor using the sodium azide (NaN₃) reagent, followed by the mono-reduction an azide moieties to amine by using half-equivalent of triphenylphosphine (PPh₃) reducing agent to generate the desired product (the N₃C₃H₆NH₂).

The preparation of N₃C₃H₆N₃ was carried out by reacting to **BrC₃H₆Br** (10M) with 2eq NaN₃ in the DMF solvent at 75°C for 12h. The reaction was monitored by Silica-TLC using 5%(Ethylacetate: N-hexane) eluent solvent-system. The spot-test for the precursor was visualized by the iodine-test, while the azide-product visualization-test was performed by Stanger (Ninhydrin/PPh₃) reaction. The final product (the N₃C₃H₆N₃) was purified via extraction in pentane solvent, rotary evocate the pentane to obtain Yield ca. 99% of N₃C₃H₆N₃, the purity ca. 99% (by NMR chemical shifts δ /ppm = 3.41(t; integral 4H) and 1.82(q; integral 2H).

The preparation of N₃C₃H₆NH₂ was carried out by reacting to N₃C₃H₆N₃ (0.45M) with 0.5eq PPh₃ in 50%(Et₂O: AcO) and 5%HCl solvent system inside ice-jacket (near 0-4°C) for 5h; the ice-jacket is used to minimize loosing of the

volatile product. Then the product was purified by extraction in dichloromethane (DCC), careful rotary evaporation. The yield of the obtained oily product ($\text{N}_3\text{C}_3\text{H}_6\text{NH}_2$) was 87%, and purity ca. 97% (by NMR chemical shifts $\delta/\text{ppm} = 1.68(\text{q}; \text{integral } 2\text{H}), 2.75(\text{t}; \text{integral } 2\text{H})$ and $3.36(\text{t}; \text{integral } 2\text{H})$), as shown in **the supporting information (S6)**.

Step I “The preparation of 3-N₃ derivatized complex” was carried out by reacting **3** (0.050M) with 1.1eq $\text{N}_3\text{C}_3\text{H}_6\text{NH}_2$ in the presence of 1.1eq HCTU and 2.2eq DIEA. The reaction occurred in the DMF solvent at room temperature for 5h. The reaction was monitored using RP-HPLC of aliquots prepared by withdrawing $0.5\mu\text{L}$ of the reaction solution and diluted with $50\mu\text{L}$ TFA-acidified H_2O . The product (**3-N₃**) was purified by RP-flash chromatography and lyophilized. The yield was 97% and purity exceeds 99%.

Step ii “The preparation of DBCO-functionalized 3-N₃ complex” was carried out by reacting **3-N₃** (0.045M) with 2eq DBCO-PEG₄-NHS in “anhydrous” DMF solvent at room temperature for 30 min. The reaction was monitored using RP-HPLC of aliquots prepared by withdrawing $0.5\mu\text{L}$ of the reaction solution and diluted with $50\mu\text{L}$ TFA-acidified H_2O . Then in one-put reaction, step iii was performed.

Step iii “The coupling between the functionalized 3-N₃ and MC6*a” was performed by transferring a freshly prepared solution of the **MC6*a** to the reaction solution of **step ii**. The peptide solution was prepared before the functionalized **3-N₃** was formed, from (1eq) **MC6*a** (0.45M) and (15eq) of DIPEA in “anhydrous DMF” solvent. After transferring the peptide solution to the reaction vessel, (1.1eq) of HCTU was added to the reaction solution. The reaction was monitored using RP-HPLC of aliquots prepared by withdrawing $0.5\mu\text{L}$ of the reaction solution and diluted with $50\mu\text{L}$ TFA-acidified H_2O . The reaction occurred at room temperature within 20 min. The product was purified by precipitation in DEE then

via using the flash-chromatographic technique, and lyophilized. The obtained product (3-[DBCO-PEG₄]MC6*a) with yield ca. 98% and purity ca. 97%.

Step iv “The cobalt insertion into 3-[DBCO-PEG₄]MC6*a” was carried out by reacting 3-[DBCO-PEG₄]MC6*a (0.45M) with 30eq Co^{II}acetate in 40%(TFE:Acetic acid) solvent system at 40°C for 30 min. The reaction was monitored using RP-HPLC of aliquots prepared by withdrawing 0.5μL of the reaction solution and diluted with 50μL TFA-acidified H₂O. The product was rotary evaporated, re-dissolved in water, then purified using RP-flash chromatography, and finally lyophilized. The obtained product (3-[DBCO-PEG₄]Co^{III}MC6*a) with yield exceeds 99% and purity ca. 97%.

2.5.3.2. Synthesis the 2nd prototype conjugate ((3-Co^{III}MC6*a)

The synthesis of the direct conjugate assembly was performed by reacting the ruthenium(II) complex (3) with MC6*a through a modified NHS synthesis protocol, followed by cobalt insertion.

Synthesis of 3-MC6*a. The preparation of 1-Osu intermediate complex (step i) was carried out by mixing 1 (0.45M) with 1.5eq of N-hydroxysuccinimide (NHS) in the presence of 1.5eq DIPEA. Anhydrous DMF was used as solvent, temperature was comprised between 0-4 °C. 1.1eq HCTU were then added to the solution to start the ester formation. After 1h, a freshly prepared solution of 1eq MC6*a (according to the HPLC-derived 1-Osu yield from the previous step) and 12eq DIPEA in anhydrous DMF was transferred to the reaction vessel at room temperature. After 15 min, the coupling was accomplished, yield being ca. 99%. The product was then purified by preparative RP-HPLC and cobalt insertion has been carried out by reacting 3-MC6*a (0.45M) with 30eq Cobalt(II)acetate in 6:4 Acetic acid:TFE at 40°C for 30 min. The final product was rotary evaporated, re-dissolved in water, then purified using RP-LC chromatography, and finally

lyophilized. The final 3-Co^{III}MC6*a product was obtained with 98% yield and 99% purity. All the reaction steps were monitored using RP-HPLC by withdrawing 0.5 μL of the reaction mixture and diluting with 50 μL 0.1% TFA water.

References

1. Chu, S., and Majumdar, A. (2012). Opportunities and challenges for a sustainable energy future. **Nature** **488**, 294–303.
2. World Energy Outlook 2017 IEA Webstore. <https://webstore.iea.org/world-energy-outlook-2017>. (Accessed 30/01/2020)
3. You, B., and Sun, Y. (2018). Innovative strategies for electrocatalytic water splitting. **Acc. Chem. Res.** **51**, 1571–1580.
4. Zhao, G., Rui, K., Dou, S.X., and Sun, W. (2018). Heterostructures for electrochemical hydrogen evolution reaction: A review. **Adv. Funct. Mater.** **28**, 1803291.
5. Cheng, Q., and Yi, H. (2017). Complementarity and substitutability: A review of state level renewable energy policy instrument interactions. **Renew. Sustain. Energy Rev.** **67**, 683–691.
6. Binz, C., Gosens, J., Hansen, T., and Hansen, U.E. (2017). Toward technology-sensitive catching-up policies: Insights from renewable energy in china. **World Dev.** **96**, 418–437.
7. Han, Z., and Eisenberg, R. (2014). Fuel from water: The photochemical generation of hydrogen from water. **Acc. Chem. Res.** **47**, 2537–2544.
8. The Future of Solar Energy as an Alternative Energy Source <https://interestingengineering.com/the-future-of-solar-energy-as-an-alternative-energy-source>. (Accessed 30/01/2020)

9. Govindjee, Kern, J.F., Messinger, J., and Whitmarsh, J. (2010). Photosystem II. In encyclopaedia of life sciences, John Wiley & Sons, Ltd, ed. (**John Wiley & Sons, Ltd**), p. a0000669.pub2.
10. Zhang, J.Z., Sokol, K.P., Paul, N., Romero, E., van Grondelle, R., and Reisner, E. (2016). Competing charge transfer pathways at the photosystem II–electrode interface. **Nat. Chem. Biol.** *12*, 1046–1052.
11. Schlapbach, L., Züttel, A., Gröning, P., Gröning, O., and Aebi, P. (2001). Hydrogen for novel materials and devices. **Appl. Phys. A** *72*, 245–253.
12. Hydrogen from renewable power: Technology outlook for the energy transition Publ.Renew.Power. <https://www.irena.org/publications/2018/Sep/Hydrogen-from-renewable-power>. (**Accessed 30/01/2020**)
13. Strmcnik, D., Lopes, P.P., Genorio, B., Stamenkovic, V.R., and Markovic, N.M. (2016). Design principles for hydrogen evolution reaction catalyst materials. **Nano Energy** *29*, 29–36.
14. Cherevko, S., Geiger, S., Kasian, O., Kulyk, N., Grote, J.-P., Savan, A., Shrestha, B.R., Merzlikin, S., Breitbach, B., Ludwig, A., et al. (2016). Oxygen and hydrogen evolution reactions on Ru, RuO₂, Ir, and IrO₂ thin film electrodes in acidic and alkaline electrolytes: A comparative study on activity and stability. **Catal. Today** *262*, 170–180.
15. Dubouis, N., and Grimaud, A. (2019). The hydrogen evolution reaction: from material to interfacial descriptors. **Chem. Sci.** *10*, 9165–9181.
16. Vilekar, S.A., Fishtik, I., and Datta, R. (2010). Kinetics of the Hydrogen Electrode Reaction. **J. Electrochem. Soc.** *157*, B1040.
17. de Chialvo, M.R.G., and Chialvo, A.C. (1994). Hydrogen evolution reaction: Analysis of the Volmer-Heyrovsky-Tafel mechanism with a generalized adsorption model. **J. Electroanal. Chem.** *372*, 209–223.

18. Hallenbeck, P. (2002). Biological hydrogen production; fundamentals and limiting processes. **Int. J. Hydrog. Energy** *27*, 1185–1193.
19. Lubitz, W., Ogata, H., Rüdiger, O., and Reijerse, E. (2014). **Hydrogenases. Chem. Rev.** *114*, 4081–4148.
20. Vignais, P.M., Billoud, B., and Meyer, J. (2001). Classification and phylogeny of hydrogenases. **FEMS Microbiol. Rev.** *25*, 455–501.
21. Schilter, D., Camara, J.M., Huynh, M.T., Hammes-Schiffer, S., and Rauchfuss, T.B. (2016). Hydrogenase Enzymes and Their Synthetic Models: The Role of Metal Hydrides. **Chem. Rev.** *116*, 8693–8749.
22. Wittkamp, F., Senger, M., Stripp, S.T., and Apfel, U.-P. (2018). [FeFe]-Hydrogenases: recent developments and future perspectives. **Chem. Commun.** *54*, 5934–5942.
23. Stripp, S.T., and Happe, T. (2009). How algae produce hydrogen—news from the photosynthetic hydrogenase. **Dalton Trans.** *45*, 9960–9969.
24. Pelmenschikov, V., Birrell, J.A., Pham, C.C., Mishra, N., Wang, H., Sommer, C., Reijerse, E., Richers, C.P., Tamasaku, K., Yoda, Y., et al. (2017). Reaction coordinate leading to H₂ production in [FeFe]-Hydrogenase identified by NRVS and DFT. **J. Am. Chem. Soc.** *139*, 16894–16902.
25. Madden, C., Vaughn, M.D., Díez-Pérez, I., Brown, K.A., King, P.W., Gust, D., Moore, A.L., and Moore, T.A. (2012). Catalytic turnover of [FeFe]-Hydrogenase based on single-molecule imaging. **J. Am. Chem. Soc.** *134*, 1577–1582.
26. Peters, J.W., Schut, G.J., Boyd, E.S., Mulder, D.W., Shepard, E.M., Broderick, J.B., King, P.W., and Adams, M.W.W. (2015). [FeFe]- and [NiFe]-hydrogenase diversity, mechanism, and maturation. **Biochim. Biophys. Acta BBA - Mol. Cell Res.** *1853*, 1350–1369.
27. Greening, C., Biswas, A., Carere, C.R., Jackson, C.J., Taylor, M.C., Stott, M.B., Cook, G.M., and Morales, S.E. (2016). Genomic and metagenomic surveys of

- hydrogenase distribution indicate H₂ is a widely utilised energy source for microbial growth and survival. **ISME J.** *10*, 761–777.
28. Schuchmann, K., Chowdhury, N.P., and Müller, V. (2018). Complex multimeric [FeFe] Hydrogenases: biochemistry, physiology and new opportunities for the hydrogen economy. **Front. Microbiol.** *9*, 2911.
 29. Stiebritz, M.T., Finkelmann, A.R., and Reiher, M. (2011). Oxygen coordination to the active site of hmd in relation to [FeFe] hydrogenase. **Eur. J. Inorg. Chem.** *2011*, 1163–1171.
 30. Bertini, I., Donaire, A., Feinberg, B.A., Luchinat, C., Picciolp, M., and Yuan, H. (1995). Solution structure of the oxidized 2[4Fe-4S] Ferredoxin from *clostridium pasteurianum*. **Eur. J. Biochem.** *232*, 192–205.
 31. Cornish, A.J., Gärtner, K., Yang, H., Peters, J.W., and Hegg, E.L. (2011). Mechanism of Proton transfer in [FeFe]-Hydrogenase from *clostridium pasteurianum*. **J. Biol. Chem.** *286*, 38341–38347.
 32. Peters, J.W., Lanzilotta, W.N., Lemon, B.J., and Seefeldt, L.C. (1998). X-ray Crystal structure of the Fe-only hydrogenase (Cpl) from *Clostridium pasteurianum* to 1.8 angstrom resolution. **Science** *282*, 1853–1858.
 33. Nicolet, Y., Piras, C., Legrand, P., Hatchikian, C.E., and Fontecilla-Camps, J.C. (1999). *Desulfovibrio desulfuricans* iron hydrogenase: the structure shows unusual coordination to an active site Fe binuclear center. **Structure** *7*, 13–23.
 34. García-Sánchez, M.I., Díaz-Quintana, A., Gotor, C., Jacquot, J.-P., De la Rosa, M.A., and Vega, J.M. (2000). Homology predicted structure and functional interaction of ferredoxin from the eukaryotic alga *Chlamydomonas reinhardtii* with nitrite reductase and glutamate synthase. **JBIC J. Biol. Inorg. Chem.** *5*, 713–719.
 35. Mulder, D.W., Boyd, E.S., Sarma, R., Lange, R.K., Endrizzi, J.A., Broderick, J.B., and Peters, J.W. (2010). Stepwise [FeFe]-hydrogenase H-cluster assembly revealed in the structure of HydAΔEFG. **Nature** *465*, 248–251.

36. Mulder, D.W., Ratzloff, M.W., Shepard, E.M., Byer, A.S., Noone, S.M., Peters, J.W., Broderick, J.B., and King, P.W. (2013). EPR and FTIR Analysis of the mechanism of H₂ Activation by [FeFe]-hydrogenase HydA1 from *Chlamydomonas reinhardtii*. **J. Am. Chem. Soc.** *135*, 6921–6929.
37. Fritsch, J., Lenz, O., and Friedrich, B. (2013). Structure, function and biosynthesis of O₂-tolerant hydrogenases. *Nat. Rev. Microbiol.* *11*, 106–114.
38. Friedrich, B., Fritsch, J., and Lenz, O. (2011). Oxygen-tolerant hydrogenases in hydrogen-based technologies. **Curr. Opin. Biotechnol.** *22*, 358–364.
39. Ash, P.A., Hidalgo, R., and Vincent, K.A. (2017). Proton transfer in the catalytic cycle of [NiFe] Hydrogenases: insight from vibrational spectroscopy. **ACS Catal.** *7*, 2471–2485.
40. Wang, X., Li, Z., Zeng, X., Luo, Q., J. Evans, D., J. Pickett, C., and Liu, X. (2008). The iron centre of the cluster-free hydrogenase (Hmd): low-spin Fe(II) or low-spin Fe(0). **Chem. Commun.** *30*, 3555–3557.
41. Yagi, T., and Higuchi, Y. (2013). Studies on hydrogenase. **Proc. Jpn. Acad. Ser. B** *89*, 16–33.
42. Salomone-Stagni, M., Stellato, F., Whaley, C.M., Vogt, S., Morante, S., Shima, S., Rauchfuss, T.B., and Meyer-Klaucke, W. (2010). The iron-site structure of [Fe]-hydrogenase and model systems: an X-ray absorption near edge spectroscopy study. **Dalton Trans. Camb. Engl.** *2003* *39*, 3057–3064.
43. Nicolet, Y., Cavazza, C., and Fontecilla-Camps, J.C. (2002). Fe-only hydrogenases: structure, function and evolution. **J. Inorg. Biochem.** *91*, 1–8.
44. Thauer, R.K., Klein, A.R., and Hartmann, G.C. (1996). Reactions with Molecular Hydrogen in Microorganisms: Evidence for a Purely Organic Hydrogenation Catalyst. **Chem. Rev.** *96*, 3031–3042.
45. Yang, X., and Hall, M.B. (2009). Monoiron Hydrogenase catalysis: hydrogen activation with the formation of a dihydrogen, Fe–Hδ···Hδ+–O, bond and

- methenyl-H4MPT⁺ triggered hydride transfer. **J. Am. Chem. Soc.** *131*, 10901–10908.
46. Di Costanzo, L., Wade, H., Geremia, S., Randaccio, L., Pavone, V., DeGrado, W.F., and Lombardi, A. (2001). Toward the de novo design of a catalytically active helix bundle: A Substrate-accessible carboxylate-bridged dinuclear metal center. **J. Am. Chem. Soc.** *123*, 12749–12757.
47. Groß, A., Hashimoto, C., Sticht, H., and Eichler, J. (2016). Synthetic peptides as protein mimics. **Front. Bioeng. Biotechnol.** *3*. Article 211 1-16
48. Morra, S., Valetti, F., Sarasso, V., Castrignanò, S., Sadeghi, S.J., and Gilardi, G. (2015). Hydrogen production at high Faradaic efficiency by a bio-electrode based on TiO₂ adsorption of a new [FeFe]-hydrogenase from *Clostridium perfringens*. **Bioelectrochemistry** *106*, 258–262.
49. Morra, S., Valetti, F., J. Sadeghi, S., W. King, P., Meyer, T., and Gilardi, G. (2011). Direct electrochemistry of an [FeFe]-hydrogenase on a TiO₂. **Electrode. Chem. Commun.** *47*, 10566–10568.
50. Ekström, J., Abrahamsson, M., Olson, C., Bergquist, J., Kaynak, F.B., Eriksson, L., Sun, L., Becker, H.-C., Åkermark, B., Hammarström, L., et al. (2006). Bio-inspired, side-on attachment of a ruthenium photosensitizer to an iron hydrogenase active site model. **Dalton Trans.** *38*, 4599–4606.
51. Ott, S., Borgström, M., Kritikos, M., Lomoth, R., Bergquist, J., Åkermark, B., Hammarström, L., and Sun, L. (2004). Model of the iron hydrogenase active site covalently linked to a ruthenium photosensitizer: Synthesis and photophysical properties. **Inorg. Chem.** *43*, 4683–4692.
52. Cui, H., Wang, M., Duan, L., and Sun, L. (2008). Preparation, characterization and electrochemistry of an iron-only hydrogenase active site model covalently linked to a ruthenium tris(bipyridine) photosensitizer. **J. Coord. Chem.** *61*, 1856–1861.

53. Mi, S., N, B., Jh, R., and My, D. (2008). Synthetic support of de novo design: sterically bulky [FeFe]-hydrogenase models. *Angew. Chem. Int. Ed Engl.* **47**, 9492–9495.
54. Almazahreh, L.R., Imhof, W., Talarmin, J., Schollhammer, P., Görls, H., El-khateeb, M., and Weigand, W. (2015). Ligand effects on the electrochemical behavior of $[\text{Fe}_2(\text{CO})_5(\text{L})\{\mu\text{-(SCH}_2)_2(\text{Ph})\text{PO}\}]$ (L = PPh_3 , P(OEt)_3) hydrogenase model complexes. *Dalton Trans.* **44**, 7177–7189.
55. Harb, M.K., Apfel, U.-P., Sakamoto, T., El-khateeb, M., and Weigand, W. (2011). Diiron dichalcogenolato (Se and Te) complexes: Models for the active site of [FeFe] hydrogenase. *Eur. J. Inorg. Chem.* **2011**, 986–993.
56. Wang, W., Rauchfuss, T.B., Bertini, L., and Zampella, G. (2012). Unsensitized photochemical hydrogen production catalyzed by diiron hydrides. *J. Am. Chem. Soc.* **134**, 4525–4528.
57. Tard, C., Liu, X., Ibrahim, S.K., Bruschi, M., Gioia, L.D., Davies, S.C., Yang, X., Wang, L.-S., Sawers, G., and Pickett, C.J. (2005). Synthesis of the H-cluster framework of iron-only hydrogenase. *Nature* **433**, 610–613.
58. Jones, A.K., Lichtenstein, B.R., Dutta, A., Gordon, G., and Dutton, P.L. (2007). Synthetic hydrogenases: incorporation of an iron carbonyl thiolate into a designed peptide. *J. Am. Chem. Soc.* **129**, 14844–14845.
59. Singleton, M.L., Reibenspies, J.H., and Darensbourg, M.Y. (2010). A cyclodextrin host/guest approach to a hydrogenase active site biomimetic cavity. *J. Am. Chem. Soc.* **132**, 8870–8871.
60. Sano, Y., Onoda, A., and Hayashi, T. (2011). A hydrogenase model system based on the sequence of cytochrome c: photochemical hydrogen evolution in aqueous media. *Chem. Commun.* **47**, 8229.
61. Sano, Y., Onoda, A., and Hayashi, T. (2012). Photocatalytic hydrogen evolution by a diiron hydrogenase model based on a peptide fragment of cytochrome c556 with

- an attached diiron carbonyl cluster and an attached ruthenium photosensitizer. **J. Inorg. Biochem.** *108*, 159–162.
62. Chong, D., Georgakaki, I.P., Mejia-Rodriguez, R., Sanabria-Chinchilla, J., Soriaga, M.P., and Darensbourg, M.Y. (2003). Electrocatalysis of hydrogen production by active site analogues of the iron hydrogenase enzyme: structure/function relationships. **Dalton Trans.** *21*, 4158–4163.
 63. Hu, X., Brunschwig, B.S., and Peters, J.C. (2007). Electrocatalytic hydrogen evolution at low overpotentials by cobalt macrocyclic glyoxime and tetraimine complexes. **J. Am. Chem. Soc.** *129*, 8988–8998.
 64. Jacques, P.-A., Artero, V., Pecaut, J., and Fontecave, M. (2009). Cobalt and nickel diimine-dioxime complexes as molecular electrocatalysts for hydrogen evolution with low overvoltages. **Proc. Natl. Acad. Sci.** *106*, 20627–20632.
 65. Sun, Y., Bigi, J.P., Piro, N.A., Tang, M.L., Long, J.R., and Chang, C.J. (2011). Molecular cobalt pentapyridine catalysts for generating hydrogen from water. **J. Am. Chem. Soc.** *133*, 9212–9215.
 66. Stubbert, B.D., Peters, J.C., and Gray, H.B. (2011). Rapid water reduction to H₂ catalyzed by a cobalt bis(iminopyridine) complex. **J. Am. Chem. Soc.** *133*, 18070–18073.
 67. Helm, M.L., Stewart, M.P., Bullock, R.M., DuBois, M.R., and DuBois, D.L. (2011). A synthetic nickel electrocatalyst with a turnover frequency above 100,000 s⁻¹ for H₂ production. **Science** *333*, 863–865.
 68. McCrory, C.C.L., Uyeda, C., and Peters, J.C. (2012). Electrocatalytic hydrogen evolution in acidic water with molecular cobalt tetraazamacrocycles. **J. Am. Chem. Soc.** *134*, 3164–3170.
 69. Carroll, M.E., Barton, B.E., Rauchfuss, T.B., and Carroll, P.J. (2012). Synthetic models for the active site of the [FeFe]-hydrogenase: catalytic proton reduction and

- the structure of the doubly protonated intermediate. **J. Am. Chem. Soc.** *134*, 18843–18852.
70. McNamara, W.R., Han, Z., Yin, C.-J. (Madeline), Brennessel, W.W., Holland, P.L., and Eisenberg, R. (2012). Cobalt-dithiolene complexes for the photocatalytic and electrocatalytic reduction of protons in aqueous solutions. **Proc. Natl. Acad. Sci.** *109*, 15594–15599.
71. Valdez, C.N., Dempsey, J.L., Brunschwig, B.S., Winkler, J.R., and Gray, H.B. (2012). Catalytic hydrogen evolution from a covalently linked dicobaloxime. **Proc. Natl. Acad. Sci.** *109*, 15589–15593.
72. Zampella, G., Bruschi, M., Fantucci, P., and De Gioia, L. (2005). DFT investigation of H₂ activation by [M(NHPnPr₃)(‘S₃‘)] (M = Ni, Pd). Insight into key factors relevant to the design of hydrogenase functional models. **J. Am. Chem. Soc.** *127*, 13180–13189.
73. Basu, D., Bailey, T.S., Lalaoui, N., Richers, C.P., Woods, T.J., Rauchfuss, T.B., Arrigoni, F., and Zampella, G. (2019). Synthetic designs and structural investigations of biomimetic Ni–Fe thiolates. **Inorg. Chem.** *58*, 2430–2443.
74. Bertini, L., Alberto, M.E., Arrigoni, F., Vertemara, J., Fantucci, P., Bruschi, M., Zampella, G., and Gioia, L.D. (2018). On the photochemistry of Fe₂(edt)(CO)₄(PMe₃)₂, a [FeFe]-hydrogenase model: A DFT/TDDFT investigation. **Int. J. Quantum Chem.** *118*, e25537.
75. Sun, Y., Benabbas, A., Zeng, W., Kleingardner, J.G., Bren, K.L., and Champion, P.M. (2014). Investigations of heme distortion, low-frequency vibrational excitations, and electron transfer in cytochrome c. **Proc. Natl. Acad. Sci.** *111*, 6570–6575.
76. Kandemir, B., Chakraborty, S., Guo, Y., and Bren, K.L. (2016). Semisynthetic and biomolecular hydrogen evolution catalysts. **Inorg. Chem.** *55*, 467–477.

77. Firpo, V., Le, J.M., Pavone, V., Lombardi, A., and Bren, K.L. (2018). Hydrogen evolution from water catalyzed by cobalt-mimochrome VI*a, a synthetic mini-protein. **Chem. Sci.** *9*, 8582–8589.
78. Chino, M., Leone, L., Zambrano, G., Pirro, F., D’Alonzo, D., Firpo, V., Aref, D., Lista, L., Maglio, O., Natri, F., et al. (2018). Oxidation catalysis by iron and manganese porphyrins within enzyme-like cages. **Biopolymers** *109*, e23107.
79. Malmstrom, B.G., and Neilands, J.B. (1964). Metalloproteins. **Annu. Rev. Biochem.** *33*, 331–354.
80. Karlin, K.D. (1993). Metalloenzymes, structural motifs, and inorganic models. **Science** *261*, 701–708.
81. Lin, Y.-W. (2019). Rational design of artificial metalloproteins and metalloenzymes with metal clusters. **Molecules** *24*, 2743.
82. Lombardi, A., Natri, F., and Pavone, V. (2001). Peptide-based heme–protein models. **Chem. Rev.** *101*, 3165–3190.
83. Schäfer, G., Purschke, W., and Schmidt, C.L. (1996). On the origin of respiration: electron transport proteins from archaea to man. **FEMS Microbiol. Rev.** *18*, 173–188.
84. Gursahani, S., Schoephoerster, R.T., and Prabhakaran, M. (2008). Exploring electron transfer between heme proteins of cytochrome c super family in biosensors: A Molecular mechanics study. **J. Biomol. Struct. Dyn.** *26*, 329–338.
85. Gray, H.B., and Winkler, J.R. (1996). Electron transfer in proteins. **Annu. Rev. Biochem.** *65*, 537–561.
86. Terwilliger, N.B. (1998). Functional adaptations of oxygen-transport proteins. **J. Exp. Biol.** *201*, 1085–1098.
87. Cowley, A.B., Kennedy, M.L., Silchenko, S., Lukat-Rodgers, G.S., Rodgers, K.R., and Benson, D.R. (2006). Insight into heme protein redox potential control and

- functional aspects of six-coordinate ligand-sensing heme proteins from studies of synthetic heme peptides. **Inorg. Chem.** *45*, 9985–10001.
88. Rone, M.B., Fan, J., and Papadopoulos, V. (2009). Cholesterol transport in steroid biosynthesis: Role of protein–protein interactions and implications in disease states. **Biochim. Biophys. Acta BBA - Mol. Cell Biol. Lipids** *1791*, 646–658.
 89. Inoue, S., Aida, T., and Konishi, K. (1992). Selective synthesis with metalloporphyrin catalysts. **J. Mol. Catal.** *74*, 121–129.
 90. Immenschuh, S., and Ramadori, G. (2000). Gene regulation of heme oxygenase-1 as a therapeutic target. **Biochem. Pharmacol.** *60*, 1121–1128.
 91. Hollenberg, P.F. (1992). Mechanisms of cytochrome p450 and peroxidase-catalyzed xenobiotic metabolism. **FASEB J.** *6*, 686–694.
 92. Everse, J. (1998). The structure of heme proteins compounds I and II: Some misconceptions. **Free Radic. Biol. Med.** *24*, 1338–1346.
 93. Smith, L.J., Kahraman, A., and Thornton, J.M. (2010). Heme proteins—diversity in structural characteristics, function, and folding. **Proteins Struct. Funct. Bioinforma.** *78*, 2349–2368.
 94. Veitch, N.C., and Smith, A.T. (2000). Horseradish peroxidase. **Adv. Inorg. Chem.** *55*, 107–162.
 95. Tanaka, M., Ishimori, K., Mukai, M., Kitagawa, T., and Morishima, I. (1997). Catalytic activities and structural properties of horseradish peroxidase distal His42 -> Glu or Gln mutant. **Biochemistry** *36*, 9889–9898.
 96. Leone, L., D’Alonzo, D., Balland, V., Zambrano, G., Chino, M., Nastri, F., Maglio, O., Pavone, V., and Lombardi, A. (2018). Mn-mimochrome VI*a: An artificial metalloenzyme with peroxygenase activity. **Front. Chem.** *6*, 590.

97. Nastri, F., Chino, M., Maglio, O., Bhagi-Damodaran, A., Lu, Y., and Lombardi, A. (2016). Design and engineering of artificial oxygen-activating metalloenzymes. **Chem. Soc. Rev.** **45**, 5020–5054.
98. Nastri, F., Lombardi, A., Morelli, G., Maglio, O., D’Auria, G., Pedone, C., and Pavone, V. (1997). Hemoprotein models based on a covalent helix–heme–helix sandwich: 1. Design, synthesis, and characterization. **Chem. Eur. J.** **3**, 340–349.
99. Nastri, F., Lombardi, A., Morelli, G., Pedone, C., Pavone, V., Chottard, G., Battioni, P., and Mansuy, D. (1998). Hemoprotein models based on a covalent helix-heme-helix sandwich. 3. Coordination properties, reactivity and catalytic application of Fe(III)- and Fe(II)-mimochrome I. **JBIC J. Biol. Inorg. Chem.** **3**, 671–681.
100. D’Auria, G., Maglio, O., Nastri, F., Lombardi, A., Mazzeo, M., Morelli, G., Paolillo, L., Pedone, C., and Pavone, V. (1997). Hemoprotein models based on a covalent helix–heme–helix sandwich: 2. Structural characterization of Co(III) mimochrome I δ and δ isomers. **Chem. Eur. J.** **3**, 350–362.
101. Lombardi, A., Nastri, F., Sanseverino, M., Maglio, O., Pedone, C., and Pavone, V. (1998). Miniaturized hemoproteins: design, synthesis and characterization of mimochrome II. **Inorganica Chim. Acta** **275–276**, 301–313.
102. Di Costanzo, L., Geremia, S., Randaccio, L., Nastri, F., Maglio, O., Lombardi, A., and Pavone, V. (2004). Miniaturized heme proteins: crystal structure of Co(III)-mimochrome IV. **JBIC J. Biol. Inorg. Chem.** **9**, 1017–1027.
103. Ranieri, A., Monari, S., Sola, M., Borsari, M., Battistuzzi, G., Ringhieri, P., Nastri, F., Pavone, V., and Lombardi, A. (2010). Redox and electrocatalytic properties of mimochrome VI, a synthetic heme peptide adsorbed on gold. **Langmuir** **26**, 17831–17835.
104. Nastri, F., Lista, L., Ringhieri, P., Vitale, R., Faiella, M., Andreozzi, C., Travascio, P., Maglio, O., Lombardi, A., and Pavone, V. (2011). A heme–peptide metalloenzyme mimetic with natural peroxidase-like activity. **Chem. Eur. J.** **17**, 4444–4453.

105. Lombardi, A., Nistri, F., Marasco, D., Maglio, O., Sanctis, G.D., Sinibaldi, F., Santucci, R., Coletta, M., and Pavone, V. (2003). Design of a new mimochrome with unique topology. **Chem. Eur. J.** **9**, 5643–5654.
106. Caserta, G., Chino, M., Firpo, V., Zambrano, G., Leone, L., D’Alonzo, D., Nistri, F., Maglio, O., Pavone, V., and Lombardi, A. (2018). Enhancement of peroxidase activity in artificial mimochrome VI catalysts through rational design. **ChemBioChem** **19**, 1823–1826.
107. Jewett, J.C., and Bertozzi, C.R. (2010). Cu-free click cycloaddition reactions in chemical biology. **Chem. Soc. Rev.** **39**, 1272.
108. Beenakker, T.J.M., Wander, D.P.A., Offen, W.A., Artola, M., Raich, L., Ferraz, M.J., Li, K.-Y., Houben, J.H.P.M., van Rijssel, E.R., Hansen, T., et al. (2017). Carba-cyclophellitols are neutral retaining-glucosidase inhibitors. **J. Am. Chem. Soc.** **139**, 6534–6537.
109. Chakraborty, S., Edwards, E.H., Kandemir, B., and Bren, K.L. (2019). Photochemical hydrogen evolution from neutral water with a cobalt metalloptide catalyst. **Inorg. Chem.** **58**, 16402–16410.
110. Takahashi, F., Hattori, K., Matsuoka, M., and Jin, J. (2016). Electrochemiluminescence of tris(2,2'-bipyridyl) ruthenium(II) with ascorbic acid and dehydroascorbic acid in aqueous and non-aqueous solutions. **Anal. Sci. Int. J. Jpn. Soc. Anal. Chem.** **32**, 443–447.
111. Gueret, R., Poulard, L., Oshinowo, M., Chauvin, J., Dahmane, M., Dupeyre, G., Lainé, P.P., Fortage, J., and Collomb, M.-N. (2018). Challenging the [Ru(bpy)₃]²⁺ photosensitizer with a triazatriangulenium robust organic dye for visible-light-driven hydrogen production in water. **ACS Catal.** **8**, 3792–3802.
112. Natali, M., Luisa, A., Iengo, E., and Scandola, F. (2014). Efficient photocatalytic hydrogen generation from water by a cationic cobalt(II) porphyrin. **Chem. Commun.** **50**, 1842.

113. Li, C., Wang, M., Pan, J., Zhang, P., Zhang, R., and Sun, L. (2009). Photochemical hydrogen production catalyzed by polypyridyl ruthenium–cobaloxime heterobinuclear complexes with different bridges. **J. Organomet. Chem.** *694*, 2814–2819.
114. Dempsey, J.L., Brunschwig, B.S., Winkler, J.R., and Gray, H.B. (2009). Hydrogen evolution catalyzed by cobaloximes. **Acc. Chem. Res.** *42*, 1995–2004.

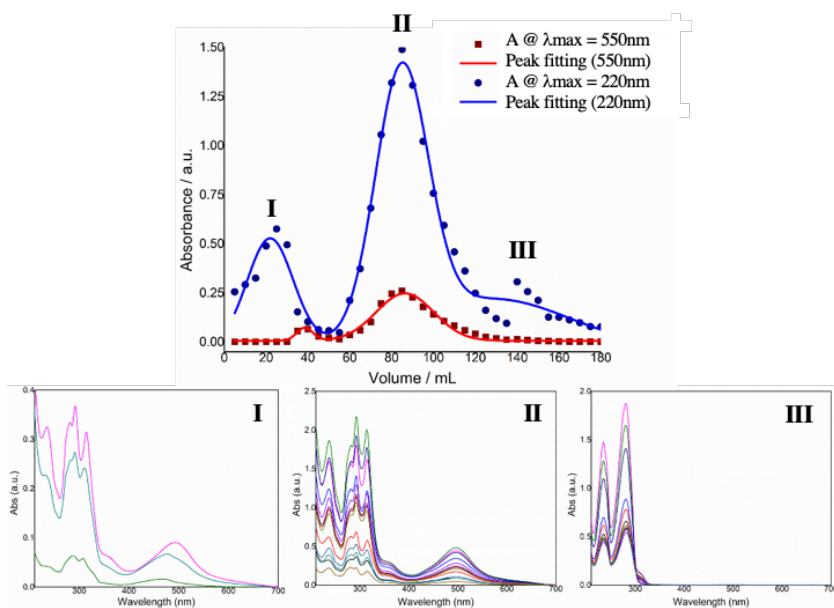
Supporting information

Size-exclusion chromatography:

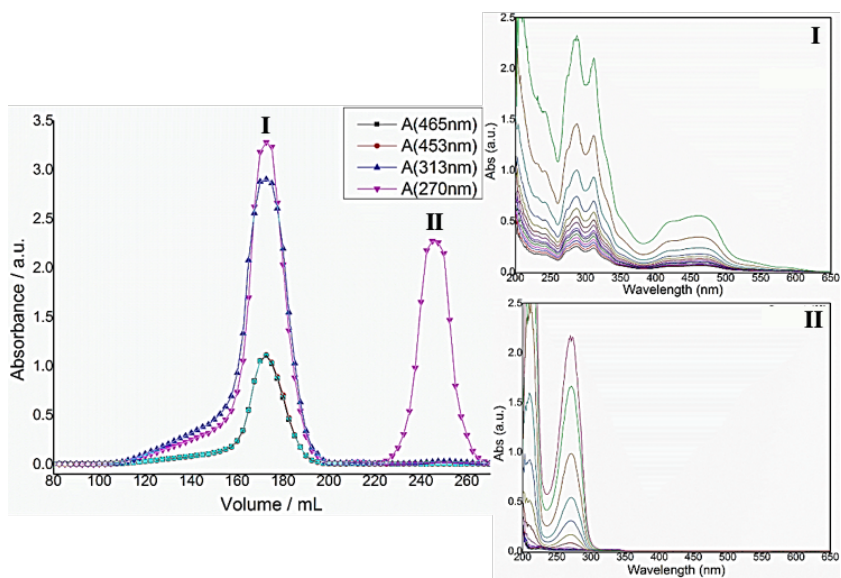
The size exclusion chromatographic purification was conducted using Sephadex-LH20 resin and methanol eluent solvent.



S1. Photo image from the size-exclusion chromatographic system, the packed column with the Sephadex-LH20 resin (**Right**) and the fraction collector (**Left**). The system was provided with a manual control-valve and a pump.



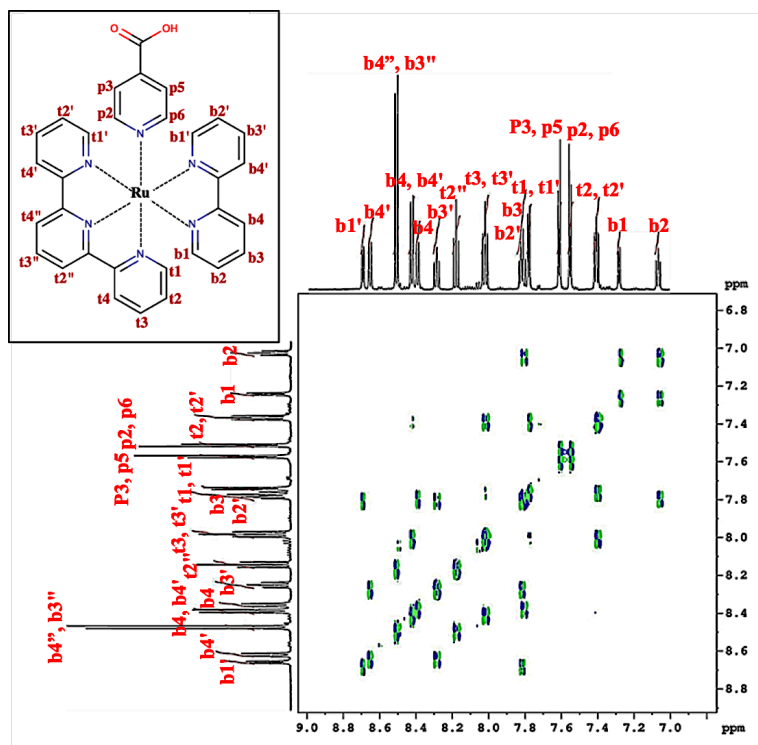
S2. Size-exclusion chromatogram of complex **2** (**Top**) and related UV-Vis spectra (**Bottom**). 1st eluted peak corresponding to Ru^{II}-complex coordinating the aqua-ligand instead of the Cl (**[2-H₂O]**) (**I**). The 2nd eluted peak corresponding to the complex **2** (**II**), and the 3rd eluted peak corresponding to the **bpy** (the excess precursor) (**III**).



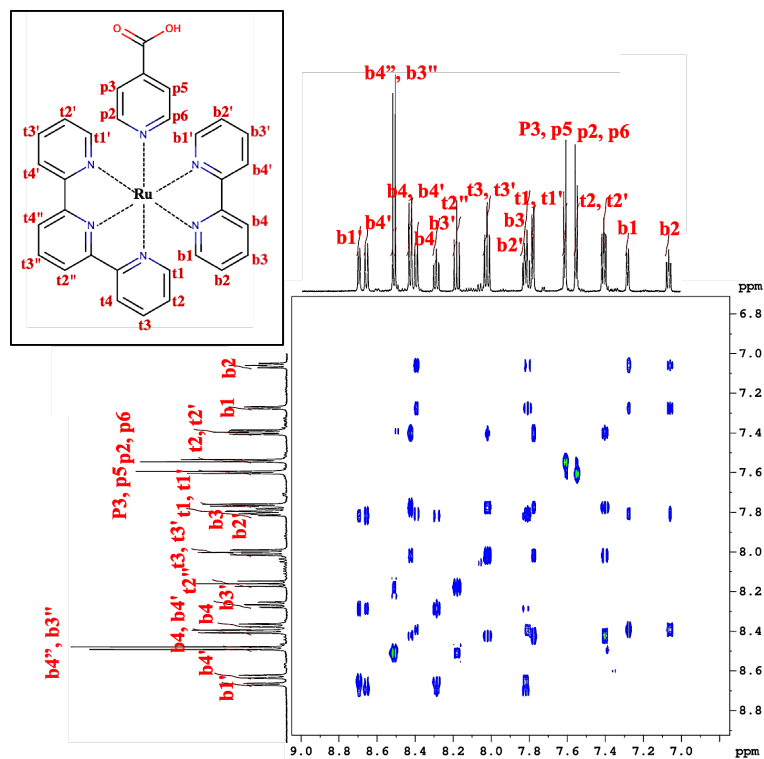
S3. Size-exclusion chromatogram of the complex **3** (**Left**) and the related UV-Vis spectra (**Right**). The 1st eluted peak corresponding to the complex **3** (**I**), and the 2nd eluted peak corresponding to the pyCOOH-ligand (the excess precursor) (**II**).

NMR spectra:

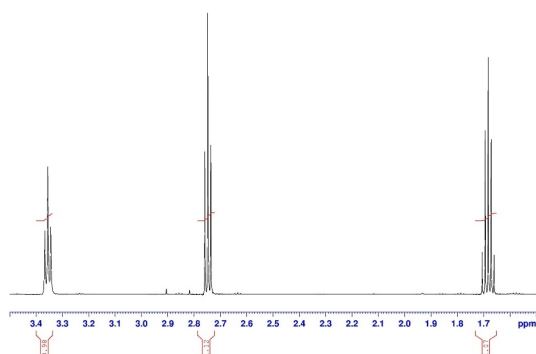
The 2D-NMR experiments (DQF-COSY and TOCSY) conducted for the complex **2** are shown in S4 and S5, respectively.



S4. 2D-DQF-COSY NMR of complex **3** in CD_3CN solvent showing the related assigned full- ^1H -NMR spectrum and the assignment-proton-key structure.

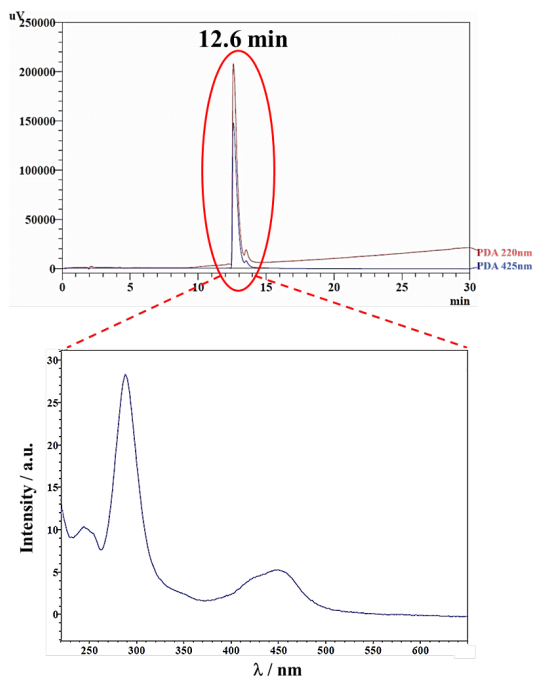


S5. 2D-TOCSY NMR of complex **3** in CD₃CN solvent showing the related assigned full-¹H-NMR spectrum and the assignment-key structure.

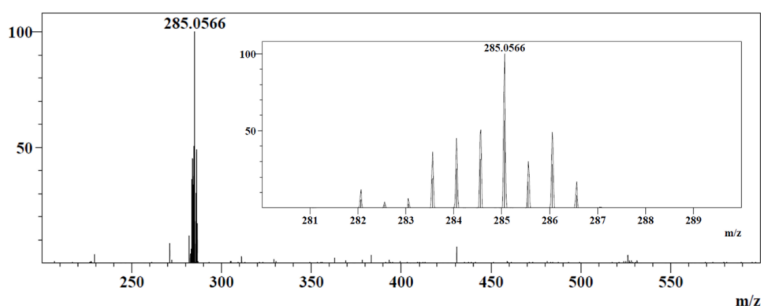


S6. ¹H-NMR of the prepared 3-azido-1-propanamine in CD₂Cl₂ solvent.

Characterization of $[\text{Ru}^{\text{II}}(\text{bpy})_3]$:

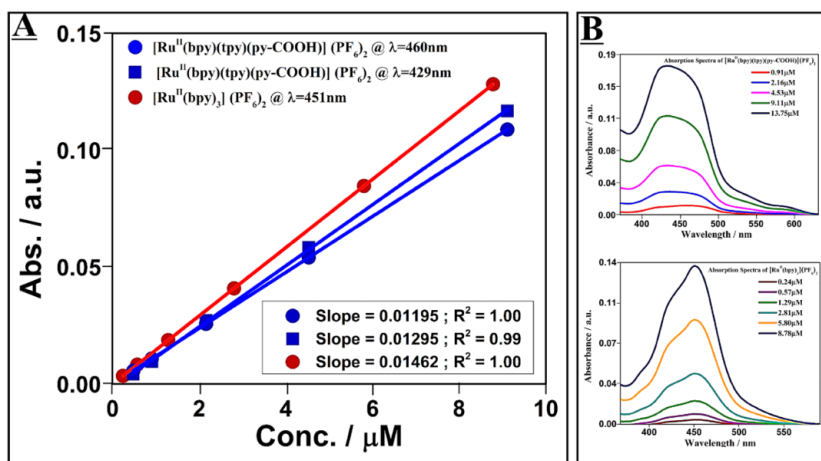


S7. RP-HPLC of the purified $[\text{Ru}^{\text{II}}(\text{bpy})_3]$ complex (**Top**), and on-line UV-Vis spectra obtained from the HPLC-PDA detector (**Bottom**).

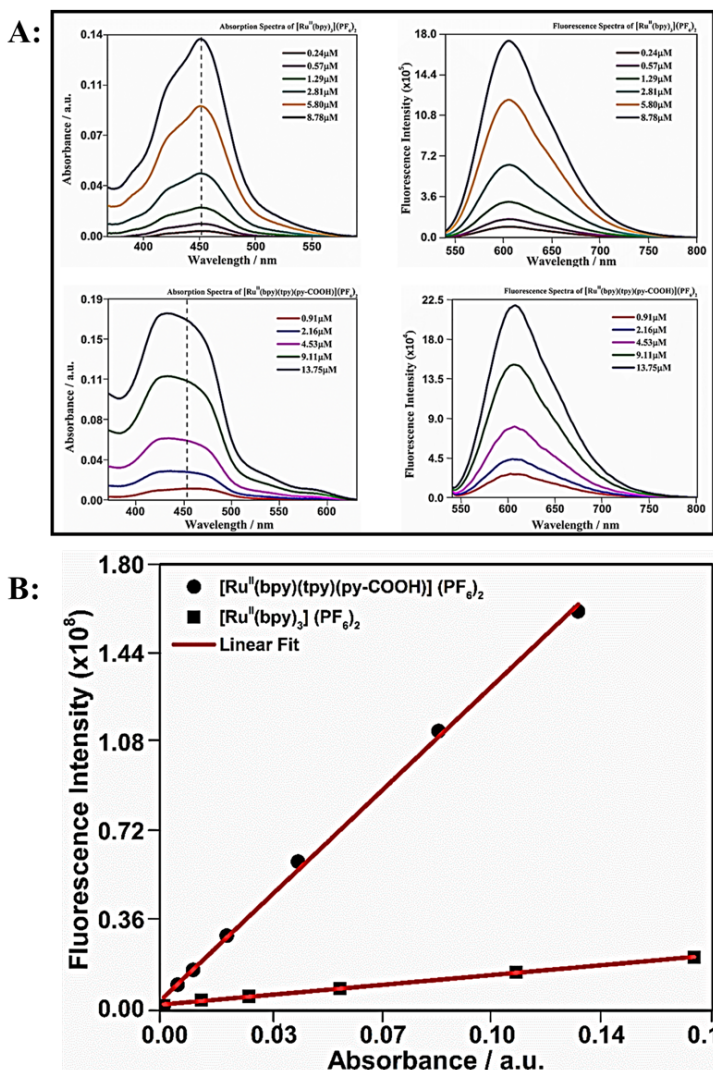


S8. IT-TOF MS spectra of $[\text{Ru}^{\text{II}}(\text{bpy})_3]$ complex, which shows a peak centered at m/z value for $[\text{M}]^{2+} = 285.0566\text{Da}$, indicating to the expected complex mass (calculated mass = 570.1132Da ; average mass = 569.59amu). [**Insert**: shows the isotopic pattern of the observed peak at $m/z = 285.0566$, with half-unity apart between the observed isotopic peaks. The most intense peak is corresponding to the most abundant Ru-102 isotope].

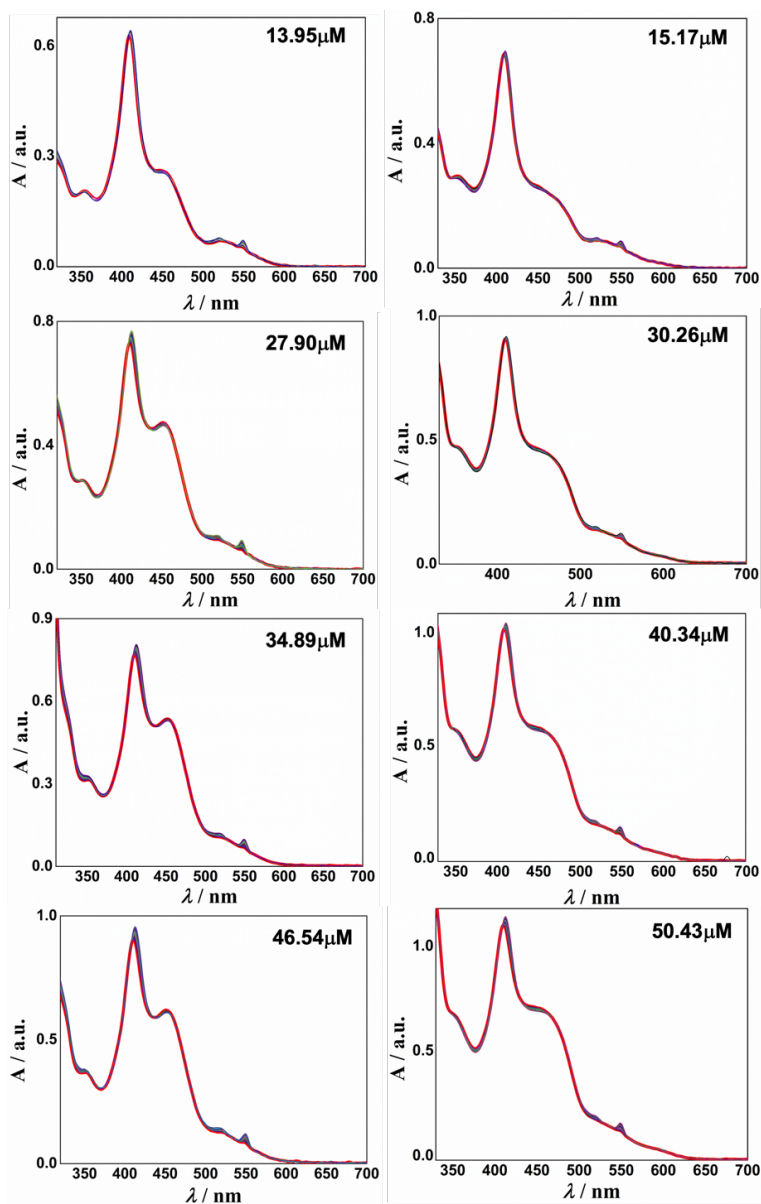
Steady-state-based photophysical and photochemical properties:



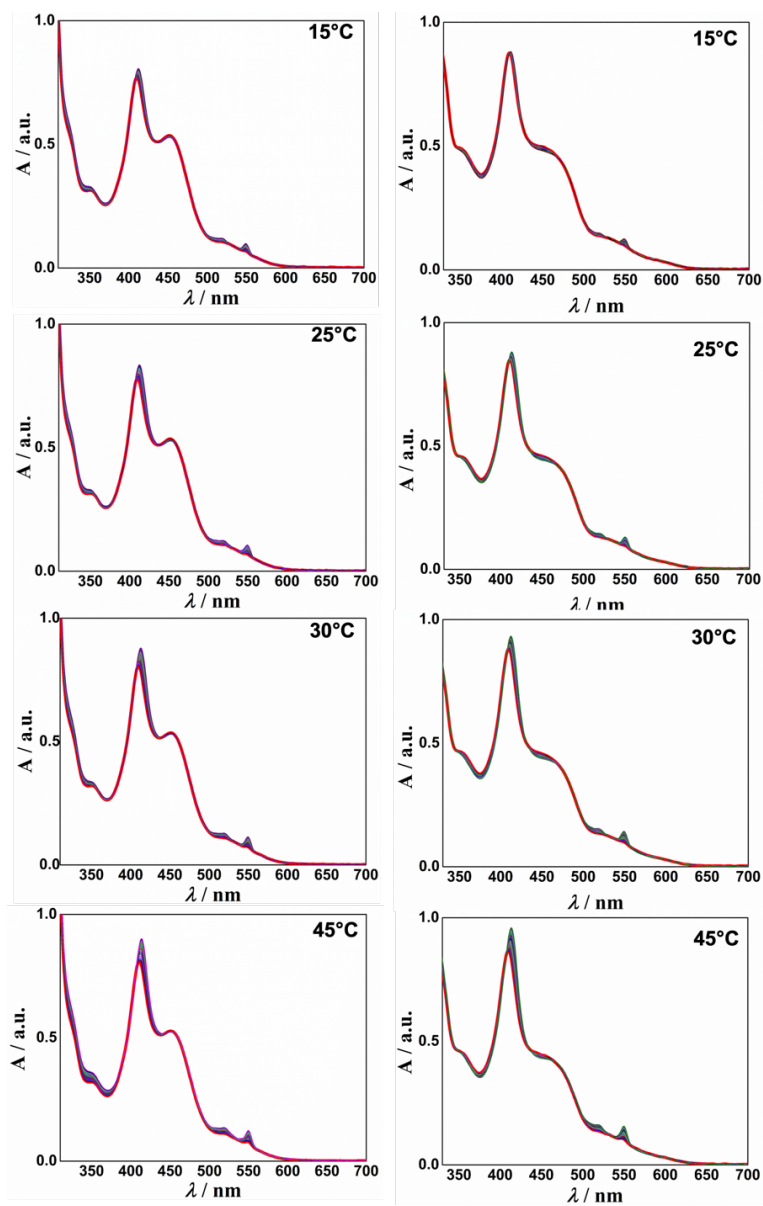
S9. Beer's-Lamberts plot (**Left**) and the ¹MLCT absorption band changes at different concentrations (**Right**) vs. concentration of complex 3 (**Top spectra**) and [Ru^{II}(bpy)₃] (**Bottom spectra**). The linear fit of the plots obtained ($\lambda_{\text{max}} = 460$ nm) for [Ru^{II}(bpy)₃] (**Redline**) and **3** (both maxima at $\lambda_{\text{max}} = 429$ nm (**Blue; squares**) and 451 nm (**Blue; circles**)) showing gradient corresponding to ϵ in $\mu\text{M}^{-1}\cdot\text{cm}^{-1}$.



S10. UV-Vis absorption and fluorescence spectra at different concentrations (**A**) of the Ru^{II}-complexes; [Ru^{II}(bpy)₃] (**A; Top**) and **3** (**A; Bottom**), and the fluorescence quantum yield (Φ) measurement via “fluorescence vs. absorbance” plots (**B**) of the MLCT transition. The gradient of the obtained plots correlated to Φ , which used to estimate the Φ of **3** compared to [Ru^{II}(bpy)₃] (the reference).

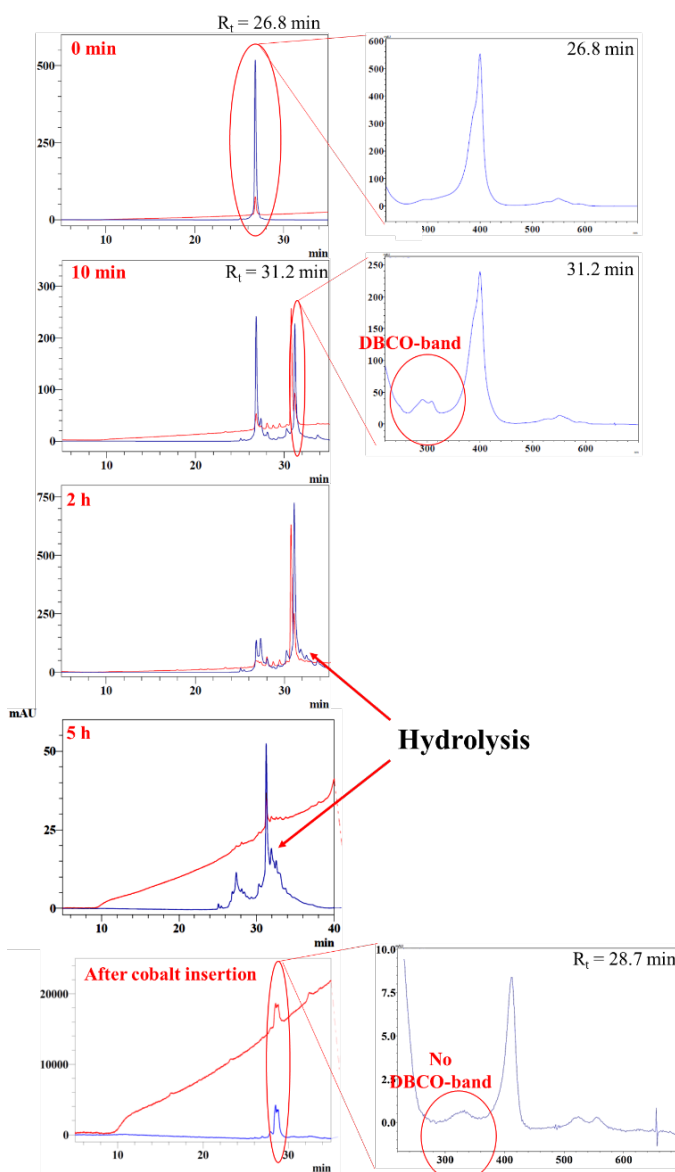


S11. Absorption spectra for photochemical reduction of the Cc, by $[\text{Ru}^{\text{II}}(\text{bpy})_3]$ (**Left**) and **3** (**Right**) at different complex concentrations, reported in each box. Overall conditions are the same as in **Figure (1.42)**.

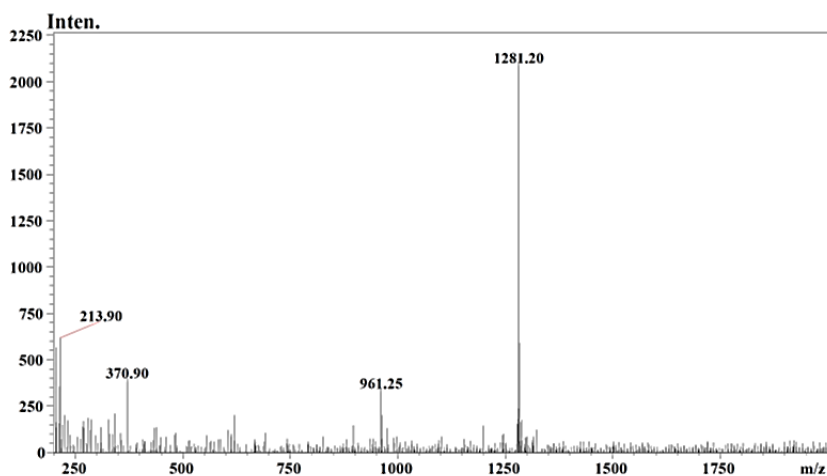


S12. Absorption spectra for photochemical reduction the Cc by Ru^{II}-complexes (30 μM) by [Ru^{II}(bpy)₃] (**Left**) and **3** (**Right**), which performed at different temperatures (15 - 45°C).

RP-HPLC and IT-TOF(MS) haracterization of the hydrolysis of the [DBCO-PEG₄]MC6*a:



S13. RP-HPLC (Left) and related UV-Vis spectra (Right), and online spectra taken within monitoring the functionalization of MC6*a with the DBCO-crosslinker.



S14. ESI-MS spectra of the Hydrolyzed [DBCO-PEG₄]MC6*a , which shows a peaks centered at m/z value for $[M+3H]^{3+} = 1281.20$, $[M+4H]^{4+} = 961.25$ indicating to the expected complex mass (calculated mass = 3840.6Da ; average mass = 3840.7amu). This observed mass is in agreement with the Co^{III}MC6*a (mass = 3492.72Da) plus the PEG4-chain loses the DBCO moiety (plus C₁₅H₂₆NO₈).

الحمد لله رب العالمين

XXXII Cycle
2017 – 2020